The Dissertation Committee for Tanuj Kiranbhai Trivedi certifies that this is the approved version of the following dissertation:

van der Waals Epitaxy and Electronic Transport in Topological Insulators

Committee:

Sanjay K. Banerjee, Supervisor

Dean P. Neikirk, Co-Supervisor

Seth R. Bank

Leonard F. Register

John G. Ekerdt

van der Waals Epitaxy and Electronic Transport in Topological Insulators

by

Tanuj Kiranbhai Trivedi

Dissertation

Presented to the Faculty of the Graduate School
of the University of Texas at Austin
in Partial Fulfillment
of the Requirements
for the Degree of

Doctor of Philosophy

The University of Texas at Austin
August 2017

Dedicated to my loved ones

and

To those late-night and weekend troopers of research who make science non-fiction

Acknowledgments

"*Le doute n'est pas une ètat bien agrèable, mais l'assurance est un ètat ridicule.*"
"Doubt is not a pleasant condition, but certainty is absurd." - **Voltaire**

It would take more than the generally tolerable number of pages to truly acknowledge all those who advised, enabled, helped, supported, loved, and endured me, so that I can pursue my PhD. Nonetheless, I would be seriously remiss if I didn't acknowledge some folks. I would like to extend my eternal gratitude to my PhD advisors Sanjay Banerjee and Dean Neikirk for mentoring, advising and supporting me throughout my graduate career. Working with them, I have truly come to appreciate the value of the bigger picture, and the value of being able to recognize value itself. I treasure the freedom I was afforded to pursue my own course in the daily activities of research. And though I bungled it many a time, my compass was always eventually recalibrated on the correct course through their advise. I want to extend my deepest gratitude to Dr. Praveen Pasupathy, Dr. Anupam Roy, and Dr. Sushant Sonde for not only being patient with my naïve and silly questions and mentoring me selflessly through the years, but also for being great friends outside the lab and providing moral support at the best and worst of times. I would also like to thank Professors Seth Bank, Leonard Frank Register, and John Ekerdt for serving on my committee and mentoring me through my PhD. A special thanks to Prof John Goodenough for being an amazing teacher, and for inspiring me to pursue science for the love of it.

I would like to acknowledge my colleagues, collaborators, mentors, and friends at the Microelectronics Research Center (MRC) who have helped me throughout my graduate career to not only make my PhD a successful venture but to also make timeless memories: Hema C. P. Movva, Ian Williamson, Kyounghwan Kim, Chris Corbet, Jeff Schmulen, Amritesh Rai, Jaehyun Ahn, Emily Walker, Stefano Larentis, Urmimala Roy, Tanmoy Pramanik, Rik Dey, Donghyi Koh, Dax Crum, Dharmendar Reddy, Kumar Appaiah, Amithraj Valsaraj, Atresh Sanne, Kyle McNicholas, Scott Sifferman, Dan Ironside, Nate Sheehan, Dan Fine, Milo Holt, Harry Chou, Sayan Saha, Michael Ramón, Emmanuel Onyegam, Maruthi Yogeesh, Donghwan Kim, Jong Yeon Park, Sheng Zhang, and Ye Chen. I won't forget those late-nights and weekends working at MRC, Wednesday/Thursday/Friday night experiments, drinking the in-

house “Banerjee coffee” for the umpteenth time, chattering away in the hallways loudly without regard to the decorum and the sanctity of the academic institution, and outwardly lamenting the clean room equipment outages all the while inwardly looking forward to the forced break. All those house parties, game nights, movie nights, climbing expeditions, Halloween nights, beer outings (and beer innings), pizza nights are lodged deep within my memory just as those tiny broken pieces of silicon that are lodged stubbornly in the nooks, cracks and crannies of the clean room. Thank you all for being there, and being yourselves.

Thanks to my brothers-in-arms, the FabLab TAs with whom I shared the burden for so many years: Andreas Hsieh, Yujia Zhai, and Tarik Akyol. Without you guys, UT ECE would not be renowned for its Solid-state Electronics program. Few bonds are as strong as those of FabLabbers! I would also like to acknowledge all my FabLab students, who heroically suffered my unendurable antics and hopefully learned a thing or two in the process, as I did from them. A shoutout to Jesse James, Bill Ostler, James Hitzfelder, Johnny Johnson, Ricardo Garcia, and Darren Robbins, who kept the complex universe of MRC running as smoothly as clockwork despite our best efforts to induce chaos. Thank you to Jean Toll and Melanie Gulick for providing indispensable help to me all these years.

To all my friends who stuck by me through thick and thin, and all the other times that were just-the-right-density, I couldn’t possibly thank you enough. But I’ll do it anyway. To my friends from Austin: Saurabh, Vaidyanathan, Richa, Melissa, Siddhartha, Vivek, and Raghunandan, to my friends on this continent and back home: Mohit, Kushan, Ishan, Vatsal, Purav, Shiv, Tania, Khushboo, Shruti, and Snigdha, thank you all for your unwavering friendship and love through all these years.

Finally, I want to express my love and enduring debt of gratitude to my family, who have stood by me all these years while I was being my usual insufferable self, and gave me their unconditional love. A few metric tonnes of thanks to my parents, without whom I would truly be lost. Thank you Geeta, Kiran, Nemi, Trupti, and Chetan. A very special thanks to my wife Heli. You are the engine to my Train Song and the rock to my tempestuous seas.

van der Waals Epitaxy and Electronic Transport in Topological Insulators

by

Tanuj Kiranbhai Trivedi, Ph.D.

The University of Texas at Austin, 2017

Supervisors: Sanjay K. Banerjee and Dean P. Neikirk

Topological insulators (TI) have been demonstrated as a unique electronic phase of matter, possessing topological surface states (TSS) with promising applications in spin-based logic and memory, heterostructures in 2D electronics and exotic physical phenomena such as Majorana quantum computing, axion electrodynamics and topological magnetoelectronics. Since the early stages of discovery, the field of applied research in TIs has evolved. However, demonstration of scalable applications remain challenging due to practical hurdles such as rapid prototyping of new TI compounds, and efficient probing of TSS for device applications. This research work endeavors to take a two-pronged approach: to address the challenges of reliable material growth and to explore TI transport physics. While indirect spectroscopy methods have indisputably shown the presence of TSS, transport in TI devices remains challenging, in part due to parasitic conduction channels. As an alternative to staple binaries, ternary and quaternary compounds $(Bi_{1-y}Sb_y)_2(Te_{1-x}Se_x)_3$ are being explored to reduce unintentional bulk-doping and gain better access to the Dirac point. The sulfur-based ternary Bi_2Te_2S has received little attention, even as its potential as a promising TI is theoretically predicted. We demonstrate first-time van der Waals epitaxial (vdWE) growth of crystalline $Bi_2Te_{2-x}S_{1+x}$ (BTS) nanosheets on SiO_2, hBN and mica. We also perform detailed magnetotransport measurements on BTS devices, establishing BTS as a candidate TI with readily accessible TSS and providing a sound picture of multiple transport channels in TI devices. A versatile process for large-area custom-feature TI growth and fabrication is also demonstrated

using BTS as the candidate TI, achieved through selective-area modification of surface free-energy on mica. TI features grow epitaxially in large single-crystal trigonal domains, exhibiting armchair or zigzag edges highly oriented with the substrate lattice. Unusual nonlinear thickness dependence on lateral dimensions and denuded zones are observed, explained by semi-empirical two-species surface migration modeling with robust estimates of growth parameters. TSS contribute up to 60% of device conductance at room-temperature, indicating excellent electronic quality. The process is constructed from highly adaptable microfabrication technology, and in conjunction with multi-species modeling, it can be customized for TI and other vdW materials device fabrication processes ranging from rapid prototyping to scalable manufacturing.

Table of Contents

List of Tables

List of Figures

Chapter 1

Introduction

1.1 Topological insulators

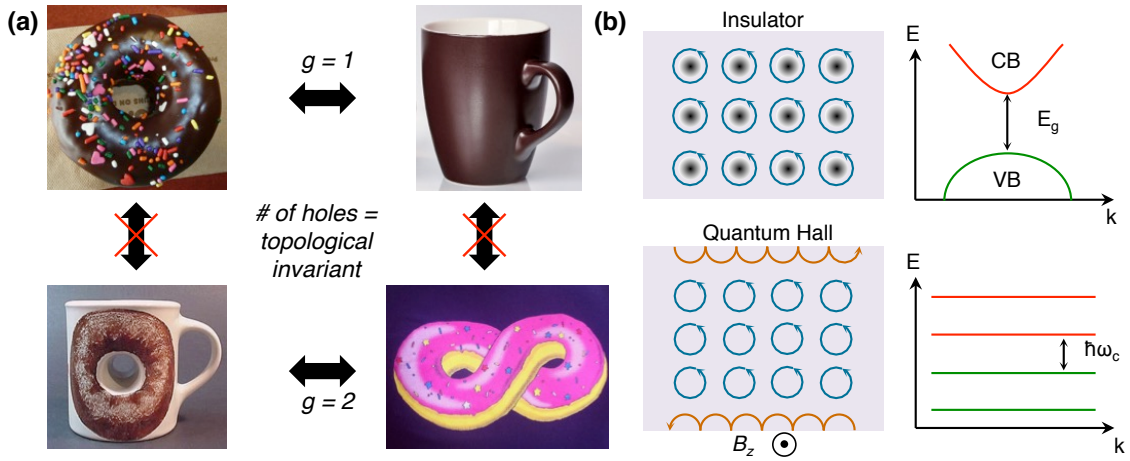

Figure 1.1: (a) Topological classification of geometrical shapes in genera defined by the number of holes present in the Euclidean surface. A transition by smooth deformation between two shapes in different columns is possible, but a transition from one shape to another between the two rows requires an abrupt opening or closing of a hole. (b) In contrast to the insulating phase, 2D quantum Hall phase has a nontrivial topology associated with it through the Chern invariant n, which leads to gapless 1D edge states at the boundaries of the sample, represented here by skipping orbits. Adapted from Hasan & Kane, 2010.[1]

Topological insulators (TI) are an electronic phase of condensed matter and some engineered material systems that have garnered significant attention in the last decade.[1–3] The physical effect and its classification as an electronic phase of matter were first theoretically predicted,[4–6] followed by predictions for candidate TI material systems[7,8] and experimental observation of its physical manifestation in two- and three-dimensional systems.[9–11] TI materials are small-gap band insulators in the bulk of the material, while possessing gapless edge- or surface-states on the boundaries of the material. The idea of applying topological classification from geometry to electronic phases of condensed matter can be traced back to the origins of quantum Hall

effect in high mobility two-dimensional MOSFET structures.[12,13] An intuitive analogy with Euclidean shapes is often utilized to understand the concept of topological classification of matter, as shown in Fig-1.1. Any 3D surface may be classified in different genera by counting the number of holes in the surface, such as a doughnut and a coffee mug both have one hole and can be classified in the same genus. Objects from the same genus can be transformed smoothly without abruptly changing the shape. However, objects in different genera cannot be smoothly deformed, *e.g.*, transforming between the coffee mug and the infinity shaped doughnut requires an abrupt closing or opening of an extra hole. The number of holes remaining constant within a genus can then be considered as some sort of a topological invariant. This analogy can then be extended to solutions obtained from band theory of condensed matter. Similarly, wavefunction solutions to the Shcrödinger Hamiltonian for a material system exist in an abstract Hilbert space as n-dimensional surfaces. As long as a wavefunction can be smoothly deformed to another without opening or closing a bandgap abruptly, they can be classified in the same topological class. An example of a trivial topological class is the classical insulating phase, such that wavefunctions for different insulator materials can be smoothly transformed between each other without closing the bandgap, and all solutions for trivial insulators are topologically equivalent to the vacuum state.[1] However, for nontrivial gapped phases that are protected by some symmetry considerations, a transition to and from a trivial insulator phase is not possible without abruptly closing or opening a bandgap. The quantum Hall effect (QHE) is an example of a topologically nontrivial phase, which nominally has an energy gap between its Landau levels, and yet has a nonzero topological invariant that is fundamentally different from the insulating phase. This is the TKNN or Chern invariant, which shows up in the quantized Hall resistance values in experiments. The Chern invariant is intimately related to the idea of geometric phase or Pancharatnam–Berry phase,[14,15] such that a nondegenerate Bloch wavefunction picks up a phase factor when the momentum coordinate goes through a full rotation. The Chern invariant is the total flux of this phase factor inside the Brillouin zone (BZ)[1] and has a nonzero value for topological materials (TM). Fundamentally novel physical phenomena can be observed at the boundary between a topologically nontrivial and a trivial material, such as between a QH sample and free-space. At the boundary of a TM, the topological invariant of the wavefunction will abruptly have to change,

which inevitably leads to closing of any energy gap and a zero-crossing in energy. This is known as the bulk-boundary correspondence. The 1D edge states in a QH sample can be visualized as "skipping orbits" of the electrons as they bounce off the edge of the sample, while in the "bulk" of the sample, they remain quantized and exhibit a Landau gap equivalent to the cyclotron energy as shown in Fig-1.1(b). An odd number of zero-crossings in the BZ will lead to edge or boundary states that are gapless, and have exotic physical properties such as topological protection. 2D QH samples exhibit these 1D boundary states, and 2D quantum spin Hall (QSH) samples exhibit pairs of such 1D states that are nondegenerate in spin[7] as seen from Fig-1.2. In QSH materials the strong spin-orbit coupling (SOC) plays a role equivalent to that of the externally applied B-field in a QH sample, leading to band inversion and zero crossings that give rise to the spin nondegenerate gapless edge states.

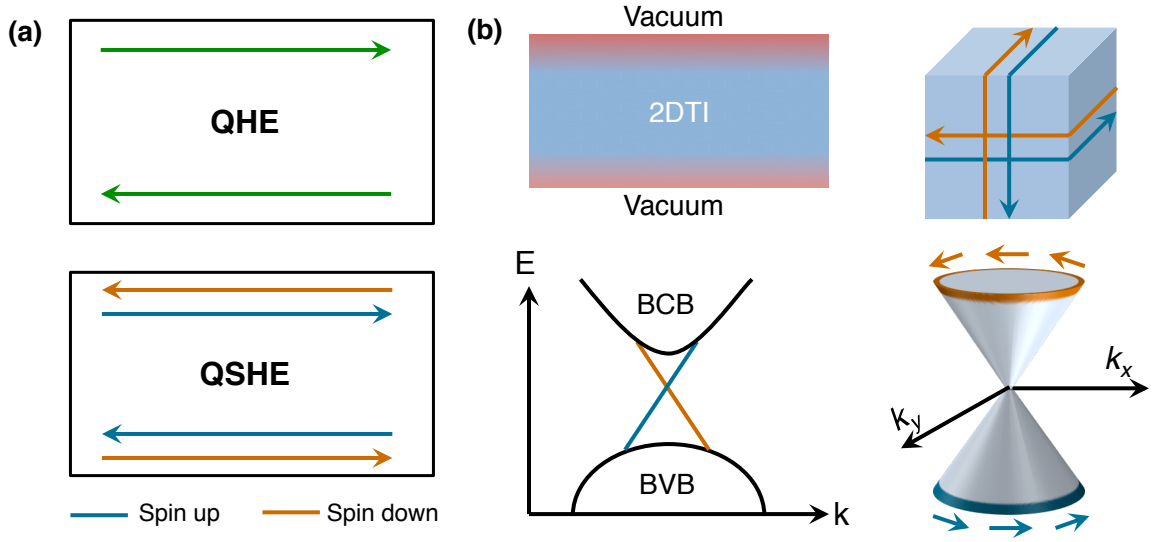

Figure 1.2: (a) Schematic representations of carrier transport in quantum Hall (top) and quantum spin Hall (bottom) samples. Adapted from Qi & Zhang, 2011.[2] (b) Edge states represented by the red zones at the boundaries of the sample and energy dispersion showing 1D Diract cone in a 2DTI (left), surface states and 2D Dirac dispersions with helical spin-momentum locking on the surface of a 3DTI (right). Adapted from Ando, 2013.[3]

For 3D materials with nontrivial topology, these states manifest as 2D surface states. These metallic edge or surface states are reminiscent of the Dirac-like states in 2D graphene as illustrated in Fig-1.2(b). However, there is a key difference

between the two materials. The gapless Dirac states in TI materials show helical spin-momentum locking, offering spin-polarized electronic transport. The gapless states are labeled topological surface states (TSS). Most of recent research has been devoted to TI's that fall under the class of time-reversal invariant systems, where the TSS are protected *via* time-reversal symmetry (TRS). 3DTIs have a topological invariant similar to the Chern invariant associated with them, the so called $\mathbb{Z}_2$ invariant.[4,5] Materials exhibiting strong SOC were predicted to obey the $\mathbb{Z}_2$ invariant topological behavior, without the need of an external magnetic field unlike in the QHE. Since the initial experimental observation of TI behavior in 2D quantum wells of HgTe/CdTe and 3D crystals of Bi_xSb_{1-x}, a plethora of material systems have been (re)-discovered as TI phases, chief amongst them being chalcogenide compounds of Bismuth (Bi) and Antimony (Sb).[1,3] The chalcogenide compounds are layered material systems, with strong in-plane bonding and van der Waals (vdW) bonding out-of-plane, forming crystalline unit cells of five layers or quintuples as shown in Fig-1.3. The binary $Bi_2(Se,Te)_3$ belong to the larger class of crystals under the tetradymite family, and have been explored extensively as the staple materials exhibiting gapless Dirac states on the surfaces of bulk crystals in Angle Resolved Photoemission Spectroscopy (ARPES) experiments. The binary TIs also show the indirect unique electronic signatures in transport experiments on thin films and devices. Proposed applications of TIs and their heterostructure devices range from topological quantum computing,[2,16] spin-based logic and memory[17] and axion electrodynamics.[18] Several prototype applications have been demonstrated in spintronics,[19–21] next-generation electronics,[22,23] on-chip optics and plasmonics,[24] and several exotic promising phenomena under intense investigation such as Majorana quantum computing,[25] axion electrodynamics and topological magnetoelectric effects.[26,27]

1.2 Current state of research

Electronic and spintronic device applications of TI often involve manipulating the electronic surface states, and hence uncovering the details of the underlying transport mechanism is an important aspect of current research. The binary phases $(Bi, Sb)_2(Se, Te)_3$ have been explored extensively as 3D TI materials from the standpoint of transport experiments.[3,28–38] Transport experiments on devices of candidate

3DTI's always include the non-negligible contribution from the bulk conductivity channels and other non-topological 2D electron gases (2DEG) at the surface due to band bending, which complicate the electronic probing of surface states.[3,39] Unlike ARPES experiments, where the bandstructure of the crystal can be directly visualized by measuring the energy and the momentum of the electrons emitted from the surface, the signatures of transport experiments cannot be trivially resolved into parallel contributions from the bulk, trivial 2DEG and TSS in a TI device. Attributing the indirect signatures to multiple conduction channels has been the focus of intense research,[3,33–36,40–42] prompting the need to further explore transport in multiple TI material systems. Over the past few years the focus has shifted to exploring ternary and quaternary compounds, $M_2X_{3-x}Y_x$ (M = {Bi, Sb, $Bi_{1-y}Sb_y$}, X, Y = {Te, Se, S}), and also doping them with magnetic and nonmagnetic impurities such as Fe, Sr, Cu, Cr *etc.* to induce physical phenomena like superconductivity, ferromagnetism etc in conjunction with the topological surface states. Addition of one or more elements to the basic binary chalcogenides lends an extra degree of freedom to manipulate the band structure, and potentially tune the topological properties of the transport.

Equally importantly, obtaining high quality crystalline thin films of TI compounds is a critical challenge that needs to be addressed for practical implementation of TI-based on-chip devices. Since the early discovery and demonstration of the staple TI compounds, the focus of research has evolved on several fronts. However, scaling on-chip device applications remains a challenging task. There are currently a limited number of methods available for repeatable and adaptable material synthesis, largely limited to highly specialized tools such as molecular beam epitaxy (MBE).[35,36,38,43] Most academic researchers utilize bulk crystals and their exfoliation to explore TI materials,[29,40,44] which has obvious limitations in implementation. Thus studies focusing on the scaling aspect and alternative mechanisms of obtaining large-area good quality TI films require immediate attention for engineering research. A simpler, rapid-protoyping alternative used for TI growth is physical vapor epitaxy, also known as sub-atmospheric hot-wall van der Waals epitaxy (vdWE).[45–49] MBE and vdWE are currently the two most favored techniques in the field. While MBE offers high quality crystalline films with a fine control over film thickness, there are limiting factors such as complexity and cost of ultra-high vacuum (UHV) systems, substrate choice, difficulty of ternary/quaternary compound growth and incompatibility with

high vapor pressure compounds (*e.g.*, sulfides).[50] On the other hand, vdWE offers a low-cost, facile alternative, accommodating more source, substrate, and compound thin film combinations,[51,52] but the control over film thickness and area remains challenging. A balance must be achieved to explore alternatives addressing the challenges of scalability and reliability of TI synthesis for practical applications.

1.3 Scope of this work

The aim of the research work summarized in this dissertation is to take a two-pronged approach to tackling practical implementation challenges for TI devices: reliable, high-quality TI synthesis and understanding the underlying transport physics in TI devices for future optimization.

The Sulfur-based ternary compound, naturally occurring tetradymite with an ideal formula Bi_2Te_2S, has received relatively little attention as a TI, even as it is theoretically predicted to be a promising 3DTI.[54] Tetradymite has been synthesized in the laboratory as bulk crystals in previous experiments showing non-stoichiometry in deviation from the ideal structure, since as early as the 1960's whence it was known to exhibit highly anisotropic electrical conduction.[55–58] The substitution of a more electronegative S for Te in the Bi_2Te_3 crystal structure (see Fig-1.3) is expected to increase the bulk band gap, reduce antisite defects and exposes the otherwise buried Dirac point. This has been confirmed to be the case in an ARPES experiment on bulk crystals of non-stoichiometric tetradymite.[58] The tetradymite ternary thus provides a promising platform to study transport signatures of the surface states.

We report on the van der Waals epitaxial growth of crystalline Bismuth Telluro-Sulfide ($Bi_2Te_{2-x}S_{1+x}$, BTS) nanosheets on SiO_2 and muscovite mica, and observation of surface states through transport experiments.[49] Weak-antilocalization (WAL), electron-electron interaction (EEI) driven insulating ground state and universal conductance fluctuations (UCF) are observed in magnetotransport experiments on BTS devices. Low-temperature insulating ground state in the conductivity of the BTS devices reveals the presence of EEI, which have been observed for thin film devices of 3DTIs. The characteristic weak antilocalization (WAL) signature of the topological surface states is seen in the magnetoresistance (MR), which acts in combination with EEI effects at low-temperatures and low-fields. Evidence of separation of trans-

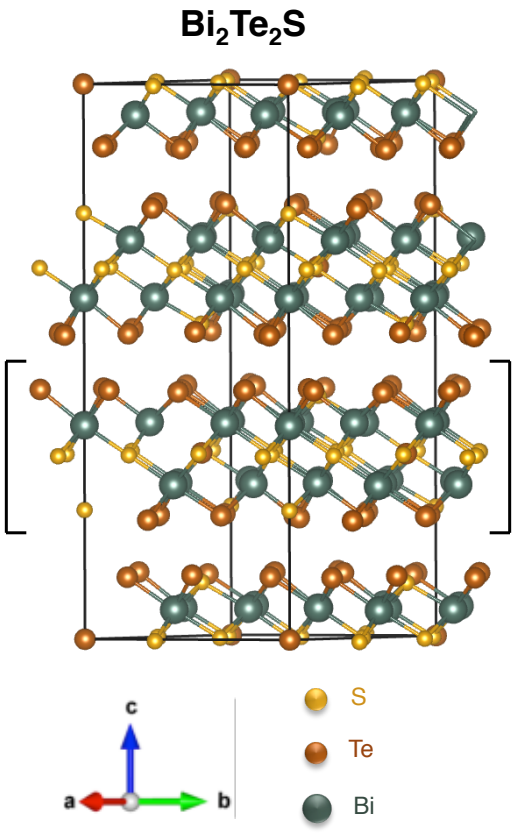

Figure 1.3: Crystal structure of the ternary tetradymite Bi_2Te_2S (ideal composition) with the quintuple layer of Te–Bi–S–Bi–Te indicated with square brackets. In reality, there is an intermixing of S and Te in the outer chalcogen layer, leading to a more S-rich compound. Crystal structure image produced with VESTA 3.[53]

port channels in Hall data is seen, with a parallel conductivity contribution from bulk states. An extended-WAL model is proposed to fit full-range MR data. A two-channel Hall conductance model is used in conjunction with the extended-WAL fit to describe the results. Universal conductance fluctuations (UCF) are also observed in the magnetoresistance of thin BTS devices, the temperature-dependent behavior of which is analyzed with standard UCF theory for two-dimensional metals, yielding phase coherence lengths of the same order as those obtained from WAL. Empirical parameters from modeling the thickness- and temperature-dependent WAL and UCF data indicate two-dimensional mesoscopic transport, revealing the presence of accessible surface states in the BTS material system.

As the natural next step towards technological relevance, a versatile process for large-area, crystalline TI growth in customizable features on mica is also presented, called custom-feature van der Waals epitaxy (CF-vdWE). The TI features grow epitaxially in large single-crystal trigonal domains of several microns in size and in any arbitrary shape of linear dimensions up to the order of 100 μm. Unusual nonlinear thickness dependence on lateral dimensions is observed along with denuded zones at boundaries, which are explained with a semi-empirical two-species surface migration model providing insights into the underlying growth mechanism, and the role of the selective-area surface modification. The subsequent mask layers for device fabrication can be effortlessly integrated post-growth using standard photolithography. DC transport on directly-grown TI Hall bars of different dimensions show metallic conduction down to 77 K, and the device sheet conductance remains remarkably flat with increasing TI Hall bar thickness at room temperature across several samples, indicating that the transport is dominated by the metallic topological surface states (TSS) with a low bulk contribution. The process only utilizes high-yield and adaptable standard microfabrication technology with the versatile vdWE method, and is easily extendable to a larger set of TI compound growths. The CF-vdWE process, in conjunction with multi-species modeling, can be customized for rapid-prototyping research for engineered substrates and vdW compound growths or can be adapted to scalable manufacturing.

Chapter-2 discusses the van der Waals epitaxial growth of Bi_2Te_3 and ternary $Bi_2Te_{2-x}S_{1+x}$ (BTS) on SiO_2, mica and hBN substrates, and in-depth materials characterization of ternary BTS nanosheets.

Chapter-3 discusses magnetotransport experiments on devices of as-grown BTS nanosheets on SiO_2. Thickness, temperature and electrostatic gating dependence of magnetoresistance, temperature dependent conductivity and electron-electron interactions, extended-HLN modeling of weak antilocalization and separation of transport channels, and universal conductance fluctuations are discussed in detail.

Chapter-4 discusses the versatile, large-area custom-feature van der Waals epitaxy growth method developed for TI growth on prepatterned mica substrates, materials characterization and analysis of the growth results.

Chapter-5 discusses and derives a semi-empirical two-species surface migration model to explain the CF-vdWE growth results. Transport measurements on as-grown

TI shapes are also presented.

Chapter-6 summarizes the major results and contributions discussed in this dissertation, and suggests potential future directions utilizing this work as a platform.

Appendix-A describes in detail the standard operating procedure and maintenance of the vdWE growth system utilized in this work.

Appendix-B describes in detail the micro and nanofabrication process recipes developed in this work.

Appendix-C describes in detail the standard operating procedure for low-noise lock-in magnetotransport measurements of TI devices using the Quantum Design PPMS system.

Chapter 2

van der Waals Epitaxy and Materials Characterization

2.1 Introduction

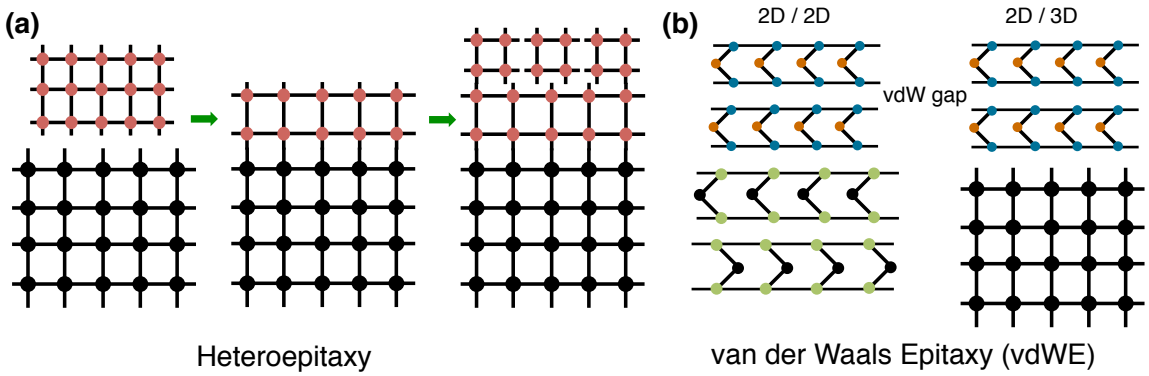

Figure 2.1: Conceptual schematics of (a) heteroepitaxy, and (b) van der Waals epitaxy. Adapted from Ueno, 2012.[59]

Over the last decade, researchers have rediscovered several of the so-called van der Waals (vdW) materials, such as graphene, hexagonal Boron Nitride (hBN), Bi/Sb-based chalcogenides and transition metal dichalcogenides ((Mo,W)(S,Se,Te)$_2$), in light of emergent physical phenomena such as massless Dirac fermions, topological states, excitonic physics, valleytronics, and spin-momentum locking to name a few. A common theme amongst these vdW materials is that their crystal structure is layered, with strong in-plane bonding and weak van der Waals bonding between layers out-of-plane. This leads to ease of obtaining material for the purposes of rapid prototyping by mechanical exfoliation, and also the creation of stacks of different vdW materials for heterostructure device applications. A similar benefit exists in thin film growth of these materials, as lattice-matching with the substrate is not crucial due to the out-of-plane van der Waals bonding.

Results discussed in this chapter were published in J. Appl. Phys. Contributions: Primary author. Designed and built the growth system, carried out the growth experiments, performed materials characterization analysis. Citation: T. Trivedi, S. Sonde, H. C. P. Movva, and S. K. Banerjee, "Weak antilocalization and universal conductance fluctuations in bismuth telluro-sulfide topological insulators," *J. Appl. Phys.*, vol. 119, no. 5, p. 055706, Feb. 2016, Available: `http://dx.doi.org/10.1063/1.4941265`.

Epitaxial thin film growth can be broadly classified in two categories: homoepitaxy (substrate and thin film are the same material) and heteroepitaxy (substrate and thin film are different materials). In most traditional epitaxy growth mechanisms, the thin film is chemically bonded to the substrate, and the lattice mismatch between the two determines the crystalline quality of the film, defect type and density and stress. In the 1970's, another class of epitaxial growth mechanism was discovered: the so called incommensurate epitaxy, where there was only a weak interaction between the adsorbate and the substrate, instead of forming strong chemical bonds as in traditional epitaxy.[60] Koma and colleagues extended the concept to epitaxial growth of thin films on substrates with more than 20% lattice mismatch, dubbing it van der Waals epitaxy (vdWE), as vdW forces are chiefly responsible for the weak bonding between the thin film and substrate during this type of growth.[61,62] The ability to grow any layered or vdW material on top of any other 2D layered or a 3D bulk material makes vdWE a versatile and convenient method to synthesize several different materials with relative ease.[52] See Fig-2.1 for schematic representations of the different growth mechanisms as discussed in this section. Fig-2.2 shows the custom built hot-wall growth setup for the TI compound growth utilized in this work.

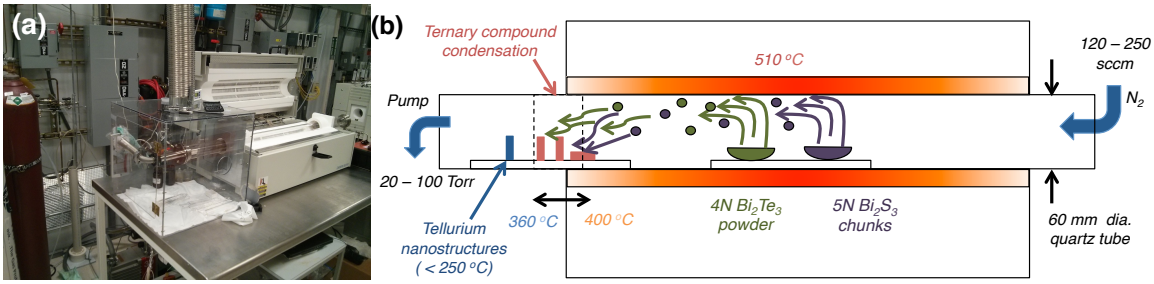

Figure 2.2: (a) Photograph, and (b) schematic of the custom-built subatmospheric hot-wall van der Waals epitaxy growth system.

2.2 vdWE growth of TI compounds

Over the past few years, Bi and Sb chalcogenide compounds have been grown using hot-wall vdWE on 3D substrates,[45,63–65] and layered substrates such as mica,[47] hexagonal Boron Nitride[46] and graphene.[66] Hot-wall growth systems utilize physical vapor transport-like mechanism to achieve the vdWE growth of layered materials

on unmatched substrates, which requires low-vacuum atmospheric conditions in the chamber with a constant carrier gas flow. The relative ease of setting up the furnace-based growth system, and its low-vacuum requirement make it a cost-effective alternative to complex UHV MBE or CVD systems. The operational principle is also simple, yet elegant, to allow for rapid prototyping of growth of different materials on different substrate for academic research. The hot-wall vdWE technique is also more preferable for growing thin-films of TI compounds containing Sulfur, as the high vapor-pressure of Sulfur makes it an undesirable source material for most molecular beam epitaxy (MBE) systems. We have built a vdWE system in-house using a programmable three-zone Lindberg/Blue M furnace with a 60 mm diameter quartz tube, connected to a roughing pump and a gas flow manifold supplying different carrier gases such as N_2, H_2 and Ar with MFC's (see Fig-2.2).

2.2.1 Growth method

We have grown Bi-based TI compounds Bi_2Te_3, $Bi_2Te_{2-x}S_{1+x}$ on different substrates in the hot-wall vdWE system with a combination of compound solid-state precursors.[49,67] Thermal SiO_2/Si, muscovite mica and exfoliated hBN are used as growth substrates. Low-resistivity ($\sim 5\ m\Omega$cm) silicon wafers are thermally oxidized to grow high quality $285 - 300$ nm thick SiO_2. An alignment marker grid for e-beam lithography is then etched into the SiO_2 film with standard photolithography and dry etch, instead of depositing metallic markers as is standard practice. Metal alignment markers are found to act as nucleation centers leading to undesirably thick, dense and malformed growth with possible metal contamination, hence etched-in alignment markers are preferred. SiO_2/Si wafers so prepared are then cleaved into samples of 5-20 mm size and placed either vertically or horizontally in a slotted quartz carrier. The quartz carrier is placed at the neck of the furnace in the cold-zone, downstream of the precursor materials ($\sim$16" away from central zone). Muscovite mica samples of similar sizes are freshly cleaved immediately prior to growth and loaded inside in a similar fashion. For several growth experiments, the cleaved mica samples are pre-patterned or roughened with an RIE O_2 plasma using patterned photoresist as an etch mask. After the plasma roughening, the PR is cleaned in hot Remover PG overnight and the patterned samples are then loaded into the furnace.

Powdered Bi_2Te_3 (4N Sigma-Aldrich) is placed in a quartz boat in the center

zone, along with chunks of Bi_2S_3 (5N Sigma-Aldrich) for the ternary BTS growth, either in the same boat or in another boat in the zone closer to the sample carrier. The quartz tube is then pumped down to base pressure several times and subsequently purged with N_2 gas for a few hours to remove any trace oxygen and moisture, and to achieve a stable pressure and flow of the carrier gas. All three zones of the furnace are then heated up to 510°C within 20 minutes without overshooting and are held at that temperature for $20-40$ minutes before being cooled down naturally to room temperature. Good growth is observed when tube pressure is in the range of $20-100$ Torr with N_2 flow in the range of $150-200$ sccm and when the samples are in the temperature range of $360-380$°C.

2.2.2 Growth results

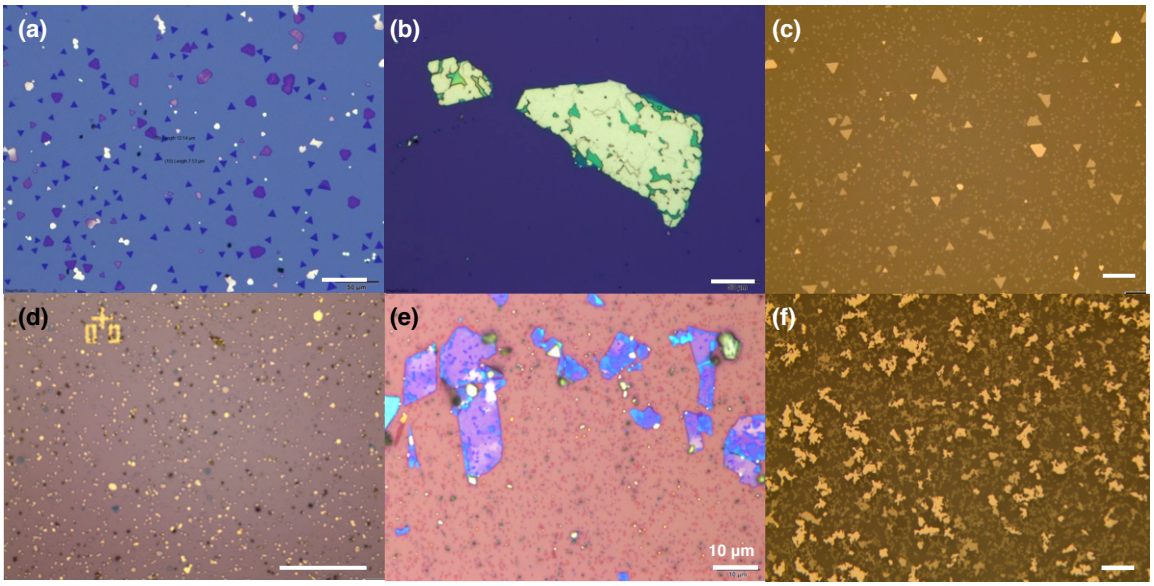

Figure 2.3: Optical images of Bi_2Te_3 on (a) SiO_2, (b) exfoliated hBN, and (c) muscovite mica, and $Bi_2Te_{2-x}S_{1+x}$ on (d) SiO_2, (e) exfoliated hBN, and (f) muscovite mica. Scale bars are 50μm unless specified.

The vdWE-grown TI nanosheets show clear crystal shape-symmetry, growing largely in hexagonal and truncated-triangular shapes of lateral dimensions of a few microns, for both Bi_2Te_3 and $Bi_2Te_{2-x}S_{1+x}$. Fig-2.3 shows optical images of representative vdWE growths on different substrates. Growth results and mechanism on

muscovite mica will be discussed in further detail in Chapters 4 and 5. The underlying crystal symmetry of the tetradymite crystal structure is trigonal-hexagonal (space group $R\bar{3}m$), which leads to the formation of layered triangular nanosheets during growth. Similar terraced growth has also been observed for other 2D material systems with trigonal symmetry, on different substrates.[38,68,69] After the initial nucleation of the islands, the ultimate shape is dependent on the variance in the growth rate along the different types of edges in the hexagonal-trigonal shape, which has been established by Monte Carlo simulation of the kinetic growth mechanism,[68,70] leading to either hexagonal or more often truncated-triangular nanosheets. The vdWE-grown nanosheets are found to nucleate randomly on the SiO_2 surface, but show evidence of highly layered growth, visible in the atomic force microscopy (AFM) height profiles of candidate BTS nanosheets in Fig-2.4. Two such examples are shown in Fig-2.4(a): a height plot (mid-right) and an amplitude error (bottom-left) and height plots (bottom-right). Fig-2.4(b) mid and bottom figures show the step height profiles, measured between subsequent terraces, accurately match the quintuple unit cell thickness of ≈ 1 nm. Tellurium-rich nanostructures are obtained for sample temperatures lower than ~ 250°C, as has been observed before in a similar growth experiment.[45] This is indicative of the decomposition of the evaporated solid-state precursor compounds (Bi_2Te_3 and Bi_2S_3) into constituent adatoms, as the samples from the colder regions of the chamber show the presence of Te-only nanostructures.

2.3 Materials characterization of BTS nanosheets

Representative samples from different growth experiments are analyzed with Raman spectroscopy and X-ray diffraction (XRD) to confirm crystallinity of the nanosheets. Compositional analysis is performed on candidate nanosheets with Carl Zeiss/EDAX energy dispersive x-ray spectroscope and X-ray photoelectron spectroscopy (XPS) to confirm the presence of all three elements within a range of stoichiometries. The results are shown in Fig-2.5.

2.3.1 XRD analysis

X-ray diffraction (XRD) spectra of as-grown BTS-on-SiO_2 and BTS-on-mica samples show sharp peak at those from the (0 0 6), (0 0 9), (0 0 12), (0 0 15) and (0 0

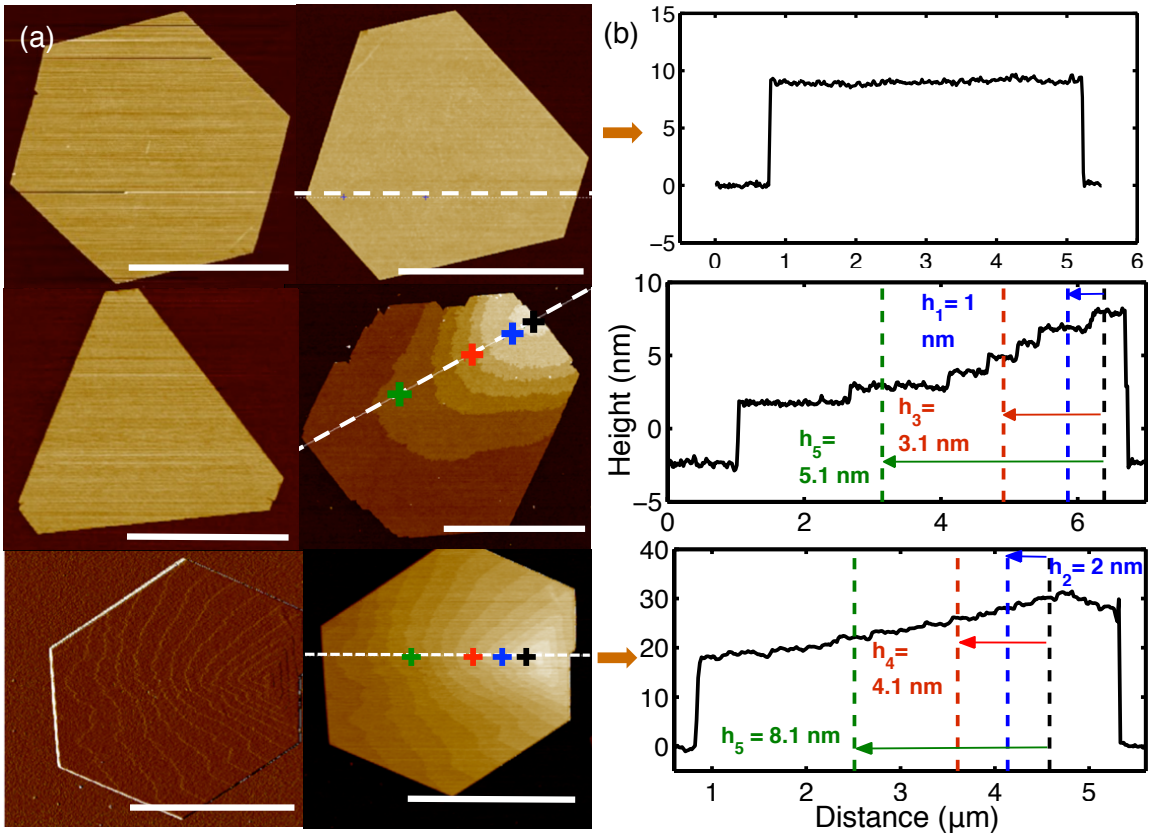

Figure 2.4: (a) AFM images of representative as-grown BTS nanosheets (scale bars 3μm) on SiO_2. (b) Cross-sectional height profiles at the dashed lines showing examples of a flat surface (top) and layered growth terraces (mid and bottom).[49]

18) facets of the tetradymite crystal only. This indicates evidence of particularly c-axis oriented growth, *i.e.*, the peaks only at the positions of the (0 0 n) facet reflections of the bulk tetradymite crystal,[56,58,71] as seen from Fig-2.5(a). The AFM results of Fig-2.4 and the XRD data confirm that, once nucleated, the BTS nanosheets subsequently grow epitaxially, forming the layered van der Waals crystal structure of the tetradymite. A preliminary comparison of the BTS-on-SiO_2 diffraction data to those expected from the crystal structure of the so-called γ-phase tetradymite proposed by Pauling[57,71] yields lattice parameters $a \approx 4.17$ Å and $c \approx 29.55$ Å, which are close to those previously reported.[58]

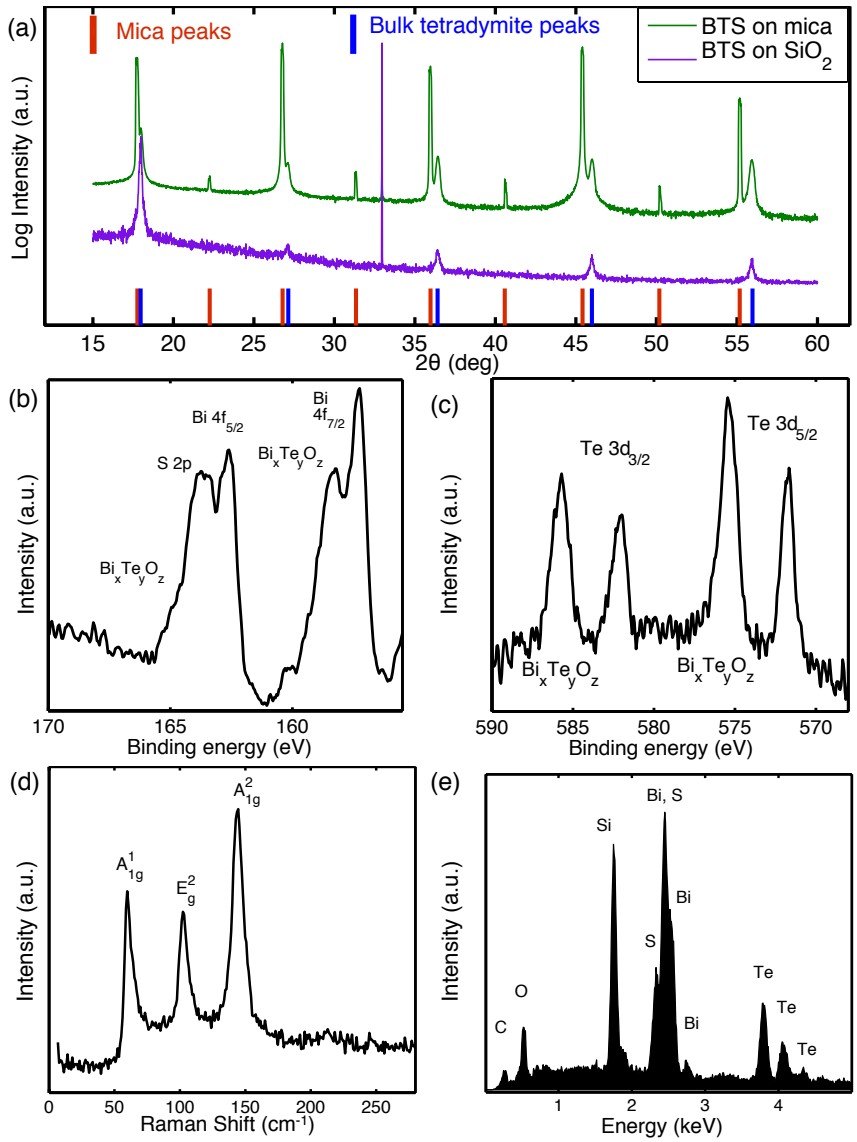

Figure 2.5: (a) X-ray diffraction pattern from as-grown BTS on mica and SiO_2 substrates, compared with bulk crystal (0 0 n) peak locations. (b), (c) Core-level X-ray photoelectron spectra showing the Bi 4f, S 2p (b) and Te 3d (c) bonding states in a candidate BTS sample, also showing the presence of a surface oxide. (d) Raman shift spectrum measured from as-grown candidate BTS nanosheet. (e) Energy dispersive X-ray analysis on as-grown BTS nanosheet showing the presence of Bi, S and Te elements.[49]

2.3.2 Raman spectroscopy

Raman spectra show sharp peaks (see Fig-2.5(d)), which are coincident with tetradymite spectrum.[71,72] Major Raman shifts are observed at $A^1_{1g} \sim 61 - 63$ cm^{-1}, $E^2_g \sim 103$ cm^{-1} and $A^2_{1g} \sim 144$ cm^{-1}, which when compared to Bi_2Te_3, exhibit a blue shift. The S-atoms occupy the middle chalcogen layer and intermix with Te-atoms in the outer chalcogen layers in the BTS crystal.[57,58] Replacing the Te atoms in the Bi_2Te_3 unit cell with the smaller S atoms leads to a smaller Bi−S bond length, more compressive strain and non-stoichiometry in the ideal tetradymite lattice, leading to the so called γ-phase in the temperature range of the growth ($360 - 380°$).[56–58] The compressive strain leads to the blue shift observed in the Raman spectrum.[72]

2.3.3 Compositional analysis

Glatz thoroughly examined the Bi_2Te_3 − Bi_2S_3 system with bulk crystals,[56] and Pauling[57] subsequently analyzed Glatz and Soonpaa's[55] work by theoretical arguments. Glatz observed two compound phases of tetradymite, β– and γ–tetradymite, in the range of 25−30% and 34−50% mole fraction Bi_2S_3 in Bi_2Te_3, respectively. Pauling calculated the stoichiometry of β-tetradymite as $Bi_{14}Te_{15}S_6$ and γ-tetradymite as $Bi_{14}Te_{13}S_8$. Pauling also observed that the ideal stoichiometry of Bi_2Te_2S would require a mole-fraction of 33.3% Bi_2S_3, which was not observed in Glatz or Soonpaa's experiments. Ji *et al.*'s recent experiment investigating tetradymite as a TI material with ARPES, also obtained the Sulfur-rich γ–phase,[58] *i.e.* $Bi_2Te_{1.6}S_{1.4}$, as was also observed for the BTS nanosheets grown in this study. The literature seems to suggest the stability of the γ–BTS compound over that of the other possible phases, and over the perfect stoichiometry of $2:2:1$.

Glatz reported limited solubility of Bi_2S_3 in Bi_2Te_3, referred to as the α–phase, in the phase diagram of the Bi_2Te_3 – Bi_2S_3 system. This phase extends up to only 4% mole fraction of Bi_2S_3 and was not observed below the solidus. This limited range of solid-solubility supports the observations in the vdWE growth of BTS nanosheets. The sample temperature range during our growth experiments is $360-380°$ C. Due to its higher vapor pressure, there is likely to be a large amount of Sulfur flux ever-present on the sample during growth. These growth conditions mainly promote the growth of the Sulfur rich phases of the ternary compound, while the solid solution/mixture

of Bi_2S_3 and Bi_2Te_3 is unlikely as reported by Glatz.

Core-level X-ray photoelectron spectroscopy (XPS) analysis on candidate BTS samples show the presence of the expected Bi 4f, S 2p and Te 3d bonding states, shown in Fig-2.5(b) and (c).[38,73,74] The chemical shifts at higher bonding energies away from the Bi 4f 5/2, 7/2 states point to the presence of a surface oxide, as do the ones observed for the Te 3d 3/2, 5/2 states.[73] The surface oxide justifies the need for plasma treating the surface of the BTS nanosheets before contact metal deposition during device fabrication. Energy dispersive X-ray spectroscopy on candidate BTS nanosheets on SiO_2 and mica show the presence of Bi, Te and S in all samples (see Fig-2.5(e)) and stoichiometries are established in the range of $Bi_2Te_{2-x}S_{1+x}$ with $x \in [0.2, 0.5]$, in near agreement with the γ-phase.

Chapter 3

Magnetotransport in vdWE Grown BTS Devices

3.1 Introduction

This chapter describes the experimental magnetotransport results obtained from electrical devices fabricated on as-grown nanosheets of BTS on SiO_2. Over the last few years, many transport experiments on different TI materials have been reported, ranging from bulk crystals, epitaxial thin films, exfoliated flakes and vdWE-grown nanosheets. The transport signatures of the topological surface states (TSS) are indirect, unlike those from ARPES experiments. While there is overall agreement in literature over the primary indirect transport signatures expected from TI's, there is still plenty of debate over the assignment of these signatures to the different transport channels present in the typical experimental setup. This work represents the first report of magnetotransport in the ternary BTS, and the results confirm the material as a candidate 3DTI with accessible surface states.

3.2 Experimental methods

3.2.1 Device fabrication

Samples of vdWE-grown BTS on SiO_2/Si are inspected using an optical microscope and AFM to identify flat and thin ($\sim 7 - 100$ nm) candidate nanosheets, with lateral dimensions in the range of a few microns. Metal contacts are patterned directly on the as-grown nanosheets in a four-point or Hallbar geometry with standard e-beam lithography and liftoff process, utilizing the alignment marker grid on the SiO_2 substrate, etched-in prior to growth. Immediately prior to metallization, the contact areas on the BTS nanosheet are etched with a brief Ar plasma ($\sim$10-12 seconds, 75 W) in an RIE chamber using the e-beam resist as the etch mask, to remove surface oxides (as observed in XPS analysis from Section-2.3.3) and any other

Results discussed in this chapter were published in J. Appl. Phys. Contributions: Primary author. Fabricated the devices, carried out the magnetotransport measurements, analyzed and modeled the transport data. Citation: T. Trivedi, S. Sonde, H. C. P. Movva, and S. K. Banerjee, "Weak antilocalization and universal conductance fluctuations in bismuth telluro-sulfide topological insulators," *J. Appl. Phys.*, vol. 119, no. 5, p. 055706, Feb. 2016, Available: http://dx.doi.org/10.1063/1.4941265.

contaminants. A 3/30 or 5/120 nm of Ti/Pd or Ti/Au metal stack is deposited with e-beam evaporation for the contact leads. The samples are then attached onto a standard 16-pin DIP package with silver-paste and wirebonded using a Au ball-bonder or an Al wedge-bonder. Sample temperature during the fabrication process is carefully maintained below 150°C to prevent material degradation.

3.2.2 Transport measurements

The wirebonded samples are loaded inside Quantum Design EverCool2 PPMS system, equipped with a 9T magnet. All magnetotransport measurements are performed using Stanford Research Systems 830 digital lock-in amplifiers. A steady current in the range of $0.1 - 1\mu A$ is supplied to the two outer terminals of the Hallbar or four-point device structure. The current source is formed by the sinusoidal voltage output of the SRS-830 and a standard series resistor. The series resistor is in the range of $\sim$1 MΩ, whereas the typical DUT resistances are of the order of $\sim$1 kΩ or less. Hence, the current fluctuation due to the DUT series-loading is three orders of magnitude lower and can be safely ignored. Four-point longitudinal (r_{xx}) and transverse (r_{xy}) resistances are measured as a function of the magnetic field B, with two phase-locked lock-in amplifiers at low frequency ($11 - 13$ Hz). The symmetric $R_{XX,\ XY}(B)$ functions are calculated as: $R_{XX}(B) = \frac{1}{2} \cdot [r_{xx}(B) + r_{xx}(-B)]$ and $R_{XY}(B) = \frac{1}{2} \cdot [r_{xy}(B) - r_{xy}(-B)]$. Temperature dependent measurements are performed down to a chamber temperature of 2 K, and magnetic field sweeps are up to $\pm$9 T.

3.3 Temperature-dependent conductivity measurements

Some examples of devices fabricated on as-grown BTS nanosheets on SiO_2 substrates in a four-point or Hallbar geometry, are shown in Fig-3.1(a), with a typical device measurement setup as shown in Fig-3.1(b). Four-point resistance was measured as a function of the sample temperature, showing an almost linearly decreasing resistance for all devices (see Fig-3.1(c)). This is indicative of a doped bulk, likely due to chalcogen deficiencies (donors) and antisite defects (acceptors), characteristic of Bi-based chalcogenide materials.[75] The BTS devices were found to be dominantly n-type from Hall data. Due to a vapor pressure higher than Tellurium, Sulfur evapo-

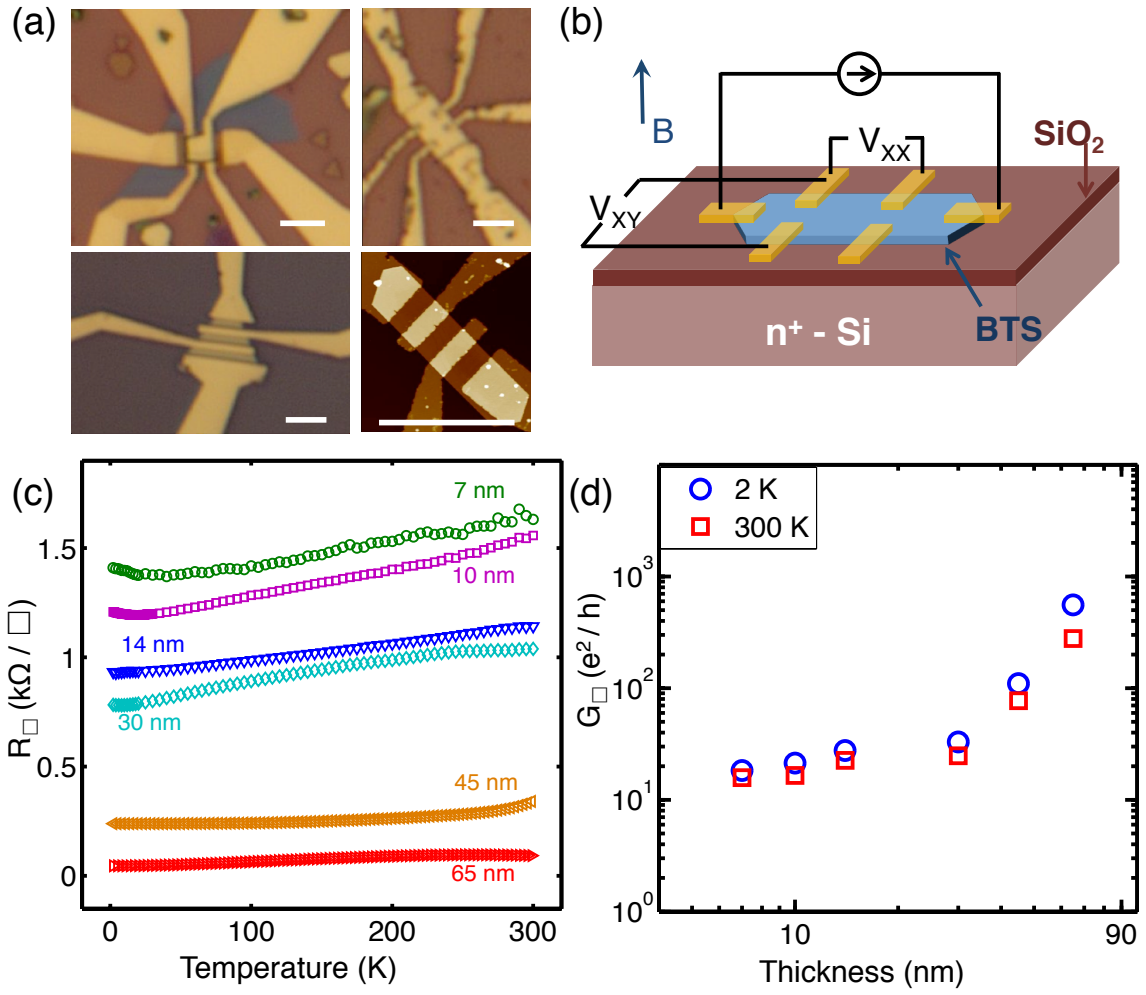

Figure 3.1: (a) Optical and AFM images of several devices (all scalebars are 3 μm). (b) Schematic diagram of a typical BTS device structure with the constant current source geometry. (c) Device sheet resistance measured as a function of temperature for different BTS thicknesses. (d) Device sheet conductance as function of BTS thickness d, in units of e^2/h.[49]

rates more during growth and device processing leaving behind donor vacancies, while the Bi-S bonding in BTS reduces acceptor-like antisite defect formation, leading to an overall n-type behavior.[58] This observation was also made for the bulk crystal case in previous experiments.[55,58] Care must thus be taken to reduce the overall fabrication and processing temperature, as was done in this study. Interestingly, Soonpaa's experiment on non-stoichiometric BTS bulk crystals also showed highly anisotropic

conductance, *i.e.*, the ratio of in-plane ($\sigma_{\parallel}$, perpendicular to the c-axis of the crystal) to out-of-plane ($\sigma_{\perp}$, parallel to the c-axis of the crystal) conductivity was large.[55] Sheet conductance data for several BTS devices are also plotted vs the BTS nanosheet thickness d in Fig-3.1(d). $G_{\square}$ is approximately flat for thinner devices, which indicates the large contribution of the surface channel to the sample conductance.[30,35] As d increases, a corresponding increase in $G_{\square}$ is seen, not unlike a doped semiconductor. This increase in conductivity indicates the growing contribution of the bulk channel for thicker nanosheets, which has been explained as increased impurity band states.[30]

3.4 Electron-electron interaction effects

There is a decrease in the rate of reduction of resistance at lower temperatures (< 50 K), oftentimes showing an increase in the resistance (see Fig-3.2(a)), or a decrease in conductivity. This decrease in the conductivity is linearly proportional to logarithmic temperature and is indicative of an insulating ground state, expected for a 2D system with electron-electron interaction (EEI), in which the Coulomb interaction between electrons is enhanced and becomes long range.[31,32,76–78] The correction to the conductivity due to the dynamically screened interaction can be expressed as:[76,79]

$$\delta\sigma_{2D} = \frac{e^2}{2\pi h}\left[2 - \frac{3}{2}\tilde{F_\sigma}\right] ln\left(\frac{T}{T_0}\right) \tag{3.1}$$

Where the fitting parameter $\tilde{F_\sigma}$ is a Hartree term related to the strength of Coulomb screening and T_0 is a reference characteristic temperature, taken as 2 K for this experiment.[76,79] Example fits for the different BTS devices are shown in Fig-3.2(b) and (c). Incidentally, the conductivity for the $d = 14$ nm device was observed to flatten out at low temperatures, unlike other devices that show a decrease, and hence could not be fitted to the EEI model. The likely reason for this observation is that out of the competing contributions from WAL and EEI, the WAL contribution is larger than EEI for the 14 nm device, and hence the decrease in conductivity due to EEI is smaller than that observed for other devices. The competing contributions are discussed in more detail in Section-3.6. The exact definition of the fit parameter $\tilde{F_\sigma}$ depends on the dimensionality of the sample, which for two-dimensional films is: $\tilde{F_\sigma}^{2D} = \frac{8}{F} \cdot (1 + \frac{F}{2}) \cdot ln(1 + \frac{F}{2}) - 4$, where F is the dimensionless factor of the screened interaction averaged on the Fermi surface, and for values of $0 < F < 1$, $\tilde{F_\sigma} \sim F$

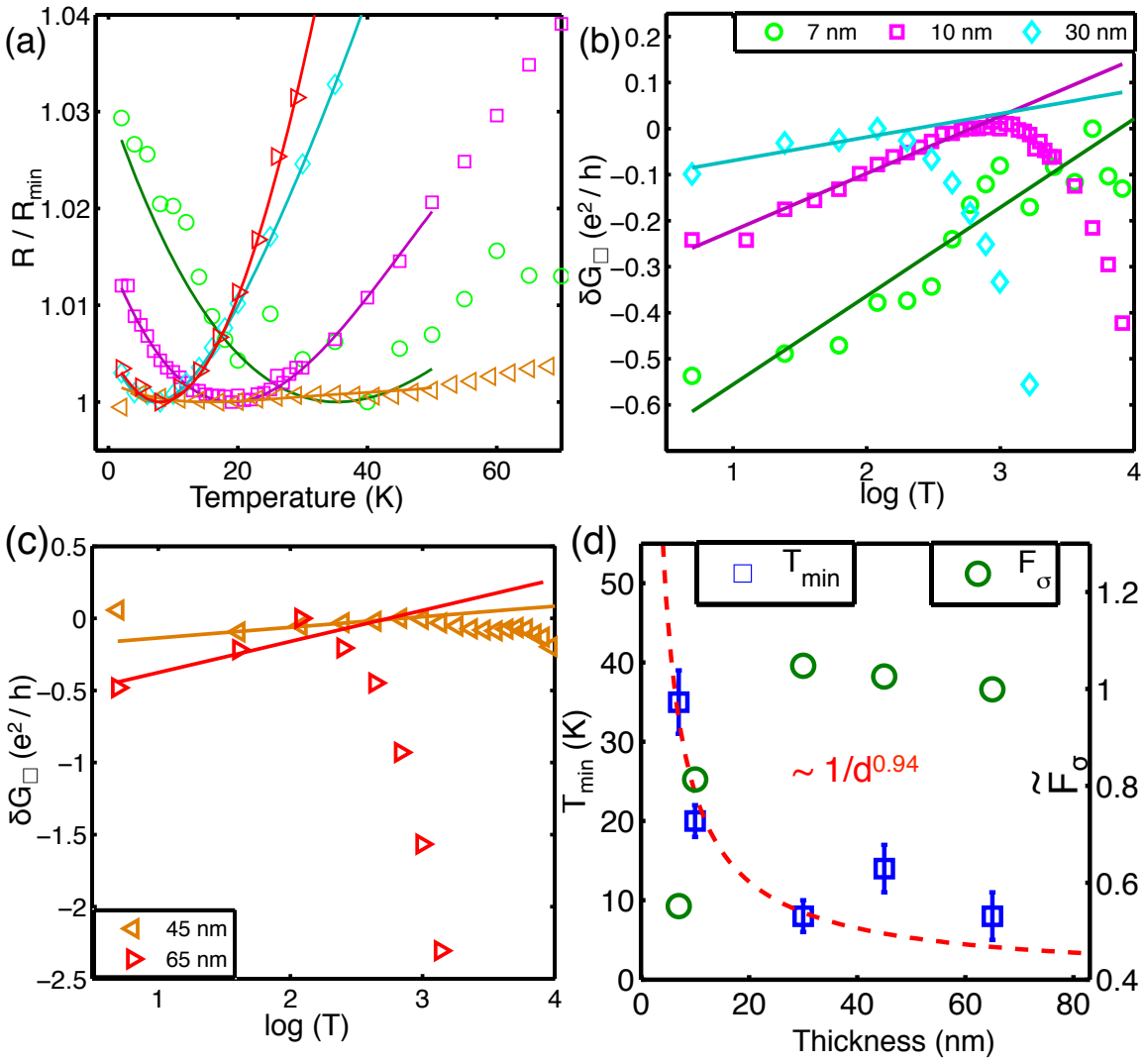

Figure 3.2: (a) Several normalized $R_\square$ vs temperature data shown at low-T, to illustrate the insulating ground state. Solid lines are a guide to the eye. (b), (c) Linear fits to conductivity variation with logarithmic temperature, due to EEI effects. (d) Temperature of resistance minima (T_{min}) and Coulomb screening factor $\tilde{F}_\sigma$ as a function of thickness d. The dashed red line is a $\sim d^{-0.94}$ fit to the T_{min} data.[49]

within 10%.[76] The nature and values of the screening parameter $\tilde{F}_\sigma$ are a matter of some debate due to the immense difficulty involved in its exact calculation and variance in experimental observation.[33,76,77,80,81] It can be shown that the functional

form of the screening factor F is:[78]

$$F = \frac{2}{\pi}\frac{\tan^{-1}\sqrt{\frac{1}{X^2}-1}}{\sqrt{\frac{1}{X^2}-1}},\ X = 2k_F\zeta \tag{3.2}$$

Here k_F is the Fermi wavevector and ζ is the Thomas-Fermi screening length. Qualitatively, for the massless Dirac case the parameter X is nonzero and leads to $F \to 0$ as X increases, signifying weaker screening. For the case of massive carrires, $X \to 0 \implies F \to 1$, signifying stronger screening. The TSS is an example of the massless Dirac case. On the other hand, when the Fermi level is at the bottom of the conduction band (BCB), bulk carriers also contribute to the transport representing the massive case. Details of the derivation of the functional form in Eq-3.2 and its limiting cases can be found in the Supplementary Information of Lu and Shen's work.[78] Thus, the values of F from 0 to 1 signify weaker screening (larger correction) to stronger screening (smaller correction) for most metals in presence of disorder.[78,80] The values of $\tilde{F_\sigma}$ from the EEI fits are shown in 3.2(d) as a function of nanosheet thickness, going from a value of ~ 0.56 for thinner to ~ 1 for thicker devices. These values indicate stronger screening in thicker devices, likely due to larger contribution from bulk carriers to the transport as explained above, thus leading to a smaller correction to $\sigma(T)$.[78] Similar values in this range have been reported for devices of TI materials and thin films of strong spin-orbit coupling materials, such as elemental Bi.[31–33,77,78,82,83]

The temperatures T_{min}, when $R = R_{min}$, are plotted vs thickness (d) of the BTS nanosheet in Fig-3.2(d) showing a $\sim d^{-0.94}$ fit. The decreasing T_{min} vs d data are qualitatively similar to the observation made for the sheet conductance vs d, as the bulk channels become more dominant for thicker devices and the onset of the 2D interaction-driven ground state is evident at lower temperatures. This $\sim 1/d$ behavior of T_{min} can be derived from a conduction model considering both surface and bulk channels contributing to the total transport. Assuming that the total conductivity can be represented as a sum of effectively two types of contribution, *i.e.*, surface and bulk channels:[29,44]

$$\sigma = \sigma_b + \frac{G^{ss}_{\square}}{d} \tag{3.3}$$

Where σ, σ_b and $G_{\square}^{ss}$ are the total conductivity, bulk conductivity and surface state (SS) conductance, respectively. Assuming that the bulk conductivity component is largely independent of the thickness of the film, and that the SS conductance follows the 2D EEI relation of Eq-3.1 (up to some correction factor converting between conductance and conductivity), a temperature-dependent conductivity correction can be written as:[49]

$$\begin{aligned} \frac{\partial \sigma}{\partial T} &\approx \frac{\partial \sigma_b}{\partial T} + \frac{C}{d \cdot T} \\ \text{At the resistance minima, } T = T_{min},\ \frac{\partial \sigma}{\partial T} &= 0 \\ \therefore 0 &\approx \left.\frac{\partial \sigma_b}{\partial T}\right|_{T_{min}} + \frac{C}{d \cdot T_{min}} \\ \therefore T_{min} &\approx \left(\frac{-C}{\left.\frac{\partial \sigma_b}{\partial T}\right|_{T_{min}}}\right) \cdot \frac{1}{d} \end{aligned} \tag{3.4}$$

C in Eq-3.4 is a combined constant factor of all the temperature independent variables obtained after differentiating the expression in Eq-3.3 and Eq-3.1. As can be seen from Eq-3.4, the temperature of the resistance minima (or conductivity maxima) scale roughly as $1/d$, as is observed in Fig-3.2(d).

3.5 Thickness-dependent magnetotransport

The symmetric longitudinal magnetoresistance (MR) R_{XX} in perpendicular magnetic field is shown in Fig-3.3(a) for several BTS devices of different thicknesses. The MR shows a sharp cusp in low-field range, which is representative of weak antilocalization (WAL). It is a result of the negative interference in electron paths due to π Berry's phase in TIs.[5] The WAL effect is especially an indicator of topologically protected surface states as TIs belong to the symplectic class and unlike topologically trivial 2D systems, don't show a crossover to weak localization from WAL.[28] Incidentally, fluctuations in the MR are also evident for thinner devices, which are discussed in further detail in Section-3.8. The WAL correction to the conductivity has been

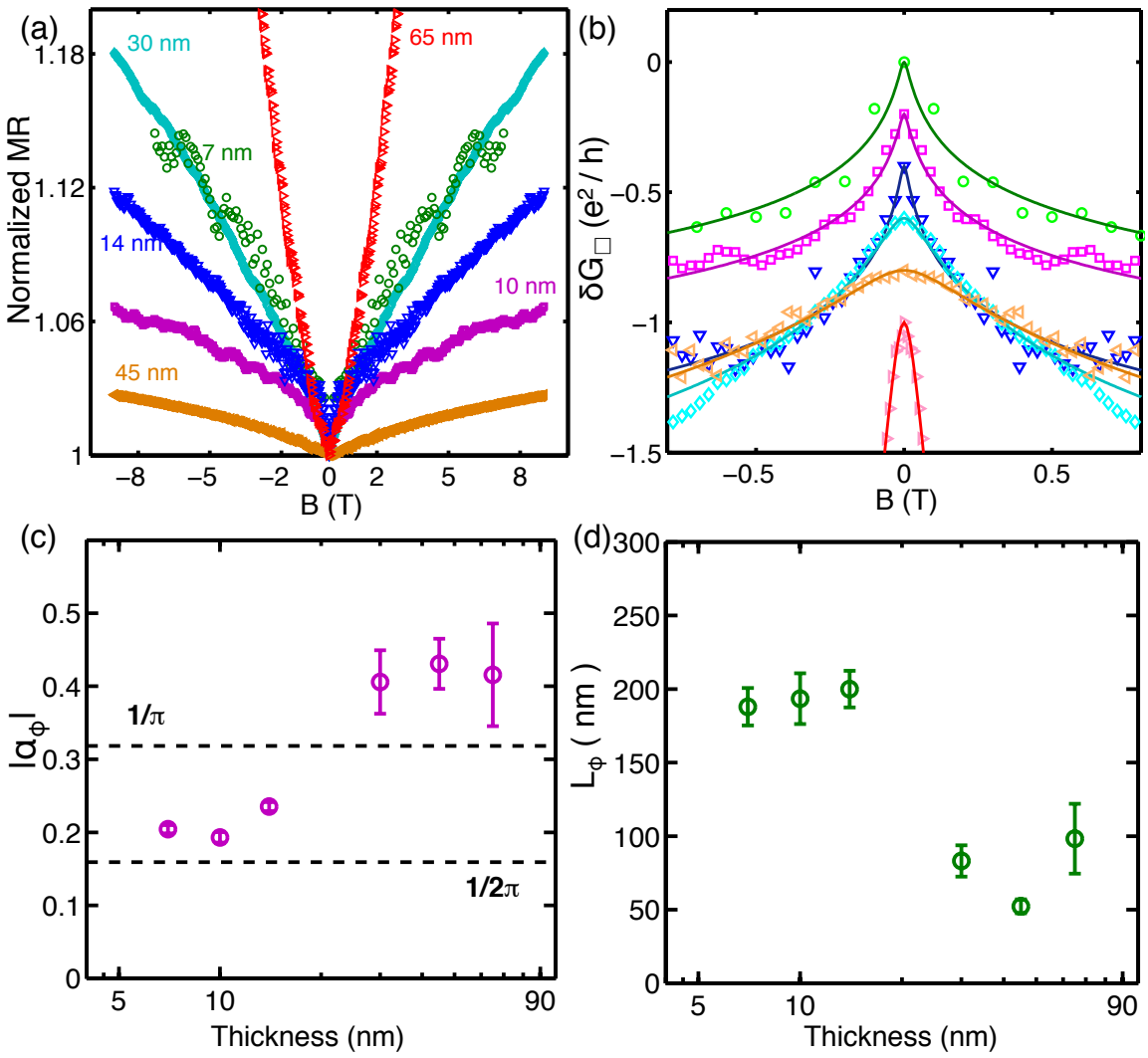

Figure 3.3: (a) Normalized symmetric longitudinal magnetoresistance R_{XX} for several devices at 2 K. (b) Reduced HLN fit to $\delta G_{\square}$ at the low-field WAL feature (solid lines are fits). Curves are shifted for clarity. (c) Reduced HLN prefactor α_ϕ vs BTS thickness d. (d) Reduced HLN-fitted phase coherence lengths L_ϕ vs BTS thickness d.[49]

computed by Hikami, Larkin and Nagaoka (HLN), and for the symplectic case it is:[84]

$$\begin{aligned}\delta G(B) &= G(B) - G(0) \\ &\approx \alpha_\phi \frac{e^2}{2\pi\hbar}\left[ln\left(\frac{B_\phi}{B}\right) - \psi\left(\frac{1}{2}+\frac{B_\phi}{B}\right)\right]\end{aligned} \tag{3.5}$$

Prefactor α_ϕ in Eq-3.5 is indicative of the nature and number of conduction channels and $B_\phi \left(= \hbar/4eL_\phi^2\right)$ is the dephasing field, associated with the characteristic phase decoherence length L_ϕ. Eq-3.5 is a simplified or reduced version of the full HLN conductivity correction, assuming strong spin orbit coupling in the transport direction, no magnetic scattering and large elastic scattering time.[84] α_ϕ is exactly equal to $1/2\pi$ for the symplectic case of the 2D topological surface channel. Several of the device MR data are fitted to Eq-3.5 in low-field limit to extract α_ϕ and L_ϕ, as shown in Fig-3.3(b). As can be seen from Fig-3.3(c) for thinner devices $\alpha_\phi \in [1/2\pi, 1/\pi]$ and for thicker ones it is larger than $1/\pi$. The exact meaning of the values and trends of the prefactor α_ϕ has been a matter of some debate, and because of its empirical fitting nature it is more an indirect indicator of the underlying complex picture of multi-channel transport.[28,33,34,40,41,85] Qualitatively however, one can distinguish regimes of transport: α_ϕ can almost continuously vary from an ideal picture of parallel symplectic channels, *i.e.*, surface states ($\nu/2\pi,\ \nu \in \mathbb{N}$), to a more complicated picture of surface states coupled *via* conductive bulk (non-integer multiples of $1/2\pi$). Value of $\alpha_\phi \in [1/2\pi, 1/\pi]$ has been attributed to phase-preserving coherent scattering between the two surface states and bulk states, which are only partially decoupled such that the contribution effectively adds up to less than two full channels.[33,34,41,42,86] Similarly, $\alpha_\phi > 1/\pi$ may indicate a larger degree of separation of surfaces but with an addition of other channels: larger bulk contribution in thicker devices and trivial 2D subbands, occurring mainly due to surface band bending.[40,42,87] This observation corroborates the $G_\square$ vs d data from Fig-3.1(d). The argument is further supported by the phase coherence length data, as shown in Fig-3.3(d) where L_ϕ is larger for thinner devices. This may be explained as a lower (higher) bulk channel contribution and hence a lower (higher) surface-to-bulk scattering in thinner (thicker) devices leading to a longer (shorter) phase-coherence time and length.[34]

3.6 Temperature-dependent magnetotransport

Temperature-dependent magnetoresistance measurement results for a candidate thin BTS device (d = 10 nm) are shown in Fig-3.4. The MR shows a sharp WAL cusp (Fig-3.4(a)), which gets smaller as the sample temperature increases. The solid lines in Fig-3.4(a) inset show the reduced HLN fits to the magnetoconductance

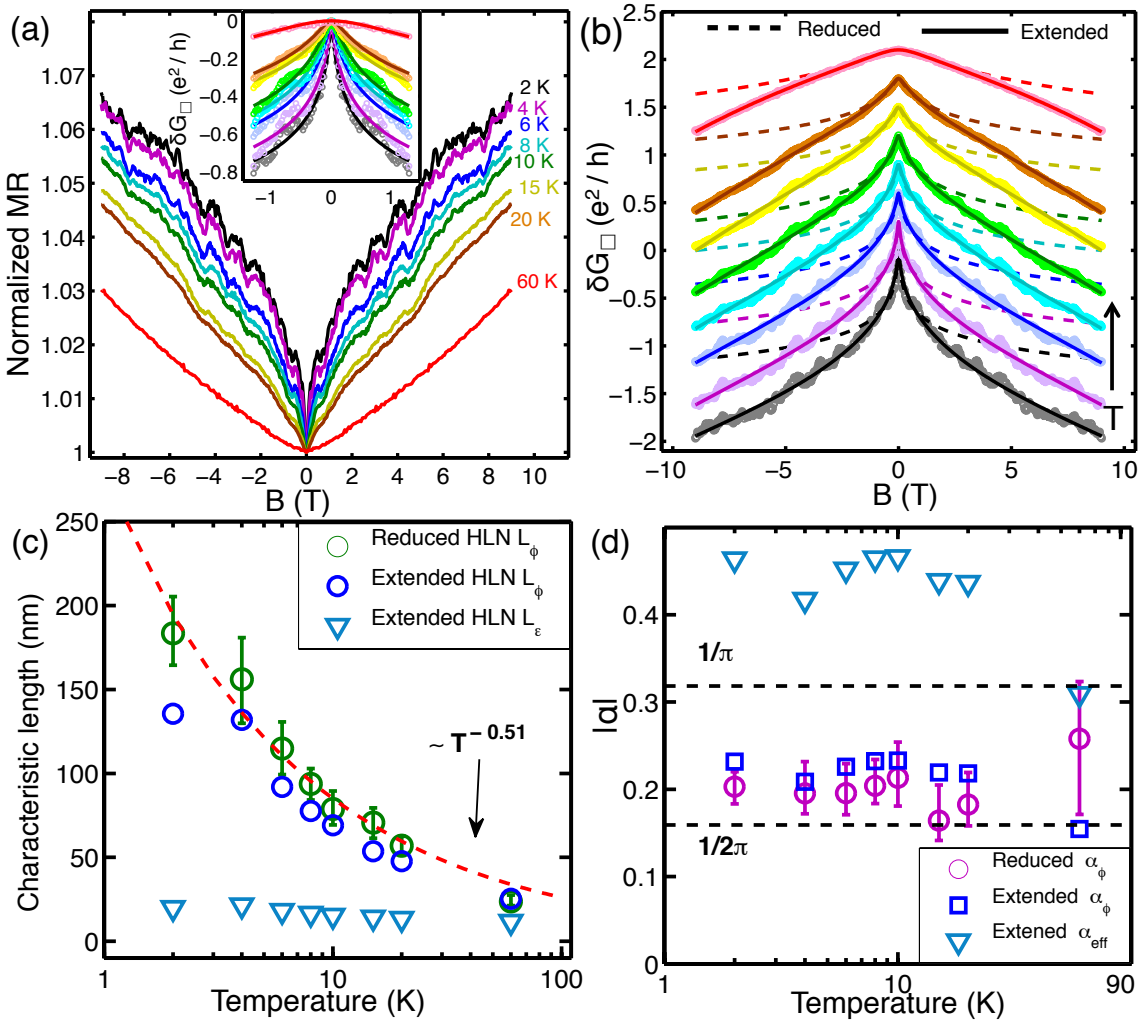

Figure 3.4: (a) Normalized symmetric longitudinal MR (R_{XX}) at different temperatures, in perpendicular magnetic field. Inset shows reduced HLN fit to $\delta G_{\square}$ at low-fields. (b) Comparison of reduced and extended HLN fit to the full range $\delta G_{\square}$ data (curves shifted for clarity). (c) Characteristic lengths from the reduced and extended HLN fits. Dashed line is a $\sim T^{-0.51}$ fit. (d) The prefactor α_{ϕ}'s from the reduced and extended HLN fits.[49]

at low magnetic fields. The limitation of the reduced fit is apparent if it is expanded to include full-range MR data (dashed lines in Fig-3.4(b)), as the high-field magnetoconductivity is not dominated by the quantum-only correction of Eq-3.5 unlike in the low-field case.

3.6.1 Extended-HLN conductivity correction

We have considered an extended version of the HLN equation as an alternative, with added terms:

$$\delta G(B) \approx \frac{\alpha_{eff}}{2}\frac{e^2}{2\pi\hbar}\left[ln\left(\frac{B_\phi}{B}\right) - \psi\left(\frac{1}{2}+\frac{B_\phi}{B}\right)\right] + \alpha_{eff}\frac{e^2}{2\pi\hbar}\left[ln\left(\frac{B_\varepsilon}{B}\right) - \psi\left(\frac{1}{2}+\frac{B_\varepsilon}{B}\right)\right] - \beta B^2 \quad (3.6)$$

Eq-3.6 has two extra correction terms compared to Eq-3.5. The second term is similar to the first in form, but it represents the contribution from elastic scattering.[84,88,89] The prefactor α_{eff} is an indicator of multiple channels effectively contributing to the correction. The final term is the conventional quadratic cyclotron term, which provides a negative correction to the overall conductivity.[90,91] The extended HLN fit of Eq-3.6 proves more reliable for full-range fitting (solid lines in Fig-3.4(b)). The characteristic lengths associated with the two dephasing fields in Eq-3.6, L_ϕ, L_ε and the reduced HLN L_ϕ, are shown as a function of temperature in Fig-3.4(c) matching closely. The dashed line represents a $T^{-0.51}$ dependence, which is an attribute of a 2D system and corresponds to Nyquist electron-electron decoherence.[40,89,92] The elastic scattering length $L_\varepsilon < L_\phi$ and changes relatively little over the temperature range. α_ϕ v T from both the fits are shown in Fig-3.4(d) matching relatively well. The equivalent prefactor of the surface channel in the extended HLN fit is obtained from the effective prefactor as $\alpha_\phi = \alpha_{eff}/2$. As before, α_ϕ is slightly larger than $1/2\pi$ at lower temperatures for both fits, indicating the presence of mainly a symplectic 2D channel, partially decoupled with the bulk states, contributing to the WAL. It is also instructive to consider the value of $\pi\alpha_{eff}$, which is ~ 1.5. A value larger than unity indicates the presence of more than one channel contributing,[40] especially with the elastic scattering term in Eq-3.6. The data at 60K is almost parabolic with a very small WAL feature, such that the first and second terms in Eq-3.6 act equivalently for the purposes of the fit and gives larger error in the reduced HLN case.

The fitting parameter β can be expressed as $\mu_{MR}^2 G_\square(0)$, where μ_{MR} is the mobility estimated from the parabolic MR term and for isotropic scattering μ_{MR} should be approximately similar to μ_{Hall}.[93] The μ_{MR} from the fit is very close to the Hall

mobility (Fig-3.6(b)), *i.e.*, ~ 150 cm^2/V·s. The temperature-dependent 2D behavior of L_ϕ and the values of α_ϕ can be understood as arising from topological surface channel contributing to the WAL cusp, while the conductive bulk also contributes to the high-field MR behavior. In prior study on Bi_2Te_3 films, additional conductivity correction terms in the HLN equation from spin-orbit scattering, were also considered.[88,89] However, for our data the spin-orbit dephasing fields $B_{SOx,z} \ggg B_\phi, B_\varepsilon$, hence could be safely ignored from the fit.

3.6.2 Quantum correction to conductivity due to WAL

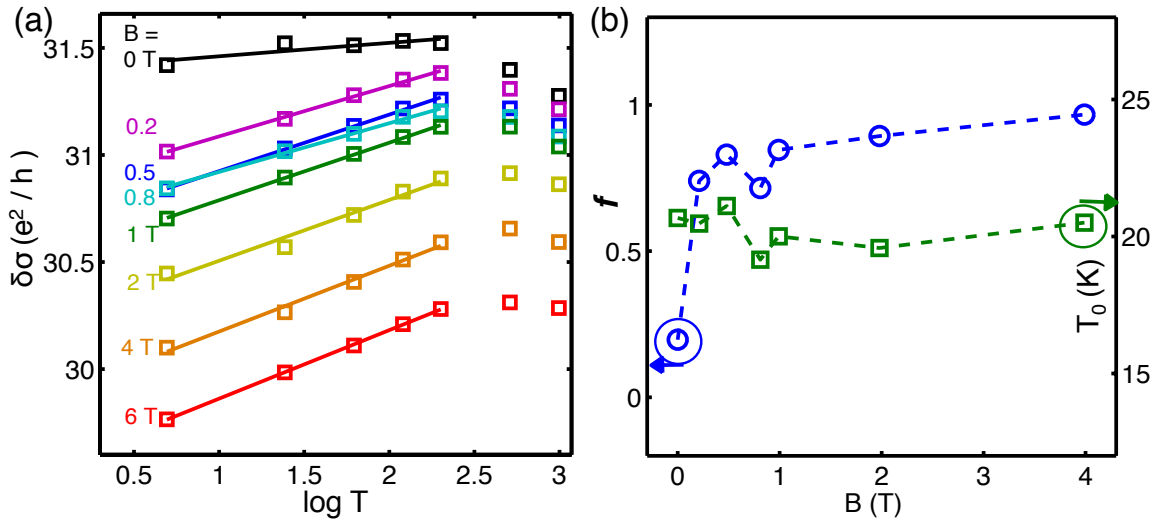

Figure 3.5: (a) Linear dependence of the longitudinal conductivity on logarithmic temperature in different magnetic fields. (b) Coefficients f and T_0 from the quantum correction the conductivity, fitted to Eq-3.8.[49]

The contribution from the WAL effect dominates the conductivity at low-temperatures and at zero-field. The expected quantum correction to the temperature-dependent conductivity in disordered systems due to localization is (in units of e^2/h):

$$\delta\sigma = -\frac{\alpha_{qc}}{\pi}\, ln\left(\frac{\tau_\phi}{\tau}\right) = \frac{\alpha_{qc} p}{\pi}\, ln\left(\frac{T}{T_L}\right) \tag{3.7}$$

Where the phase coherence time $\tau_\phi \sim T^{-p}$ ($p = 1$ for 2D), α_{qc} is a prefactor similar in nature to α_ϕ from the HLN fit and T_L is the temperature at which the

correction disappears.[78,79,81] The conductivity should continue to increase with decreasing temperature for a purely WAL-like contribution. However, as discussed in Section-3.3 and 3.4, the devices show a decrease in the conductivity with decreasing temperature, which is linearly proportional to logarithmic temperature and is attributed to EEI. The EEI correction is also logarithmic in nature similar to Eq-3.7, as seen from Eq-3.1. The low-temperature conductivity in different perpendicular magnetic fields can be then fitted to a generic equation of the form (in units of e^2/h):

$$\delta\sigma = \frac{f}{\pi}\ ln\left(\frac{T}{T_0}\right) \tag{3.8}$$

Where f is the slope of the line (equivalent to $\alpha_{qc}p$, $(1-\frac{3}{4}\tilde{F}_\sigma)$ from Eq-3.7 and Eq-3.1) and T_0 is the characteristic temperature. Fig-3.5(a) shows the temperature dependent conductivity fits to Eq-3.8, and Fig-3.5(b) shows the values of f, T_0 as a function of magnetic field. f saturates to ~ 1 at fields higher than 2 T, whereas T_0 is within 20 ± 1 K and approximately independent of field. Thus the WAL and EEI effects arise in a similar temperature range. The value of α_{qc} can be extracted from $\alpha_{qc}p = \delta f \approx 0.7$ with $p = 1$ for 2D states, which is slightly different than the HLN-fitted $\pi\alpha_\phi \approx 0.66$ but still indicates effectively a single surface state with a bulk contribution.[32,78] This variation in α has been observed in previous experiments.[31,38,78,79,81] The saturating value of f at higher fields points to a dominant contribution from EEI, as the magnetic field dependence of EEI is weaker, while the low-field variation in f may be attributed to the WAL effect, such as both effects act in combination for the BTS devices.[37,38,78,79,81]

3.7 Two-channel Hall conductivity model

Fig-3.6 shows the results obtained from a two-channel model[29,35,42,44] fit to the Hall conductivity G_{xy} data, to investigate the parallel contribution from the surface and bulk effective channels. In terms of the conductivity tensor components, a generic multi-carrier model can be represented as:

$$G_{XX} = e\sum_i \frac{n_i\mu_i}{1+\mu_i^2B^2},\ G_{XY} = eB\sum_i \frac{n_i\mu_i^2}{1+\mu_i^2B^2} \tag{3.9}$$

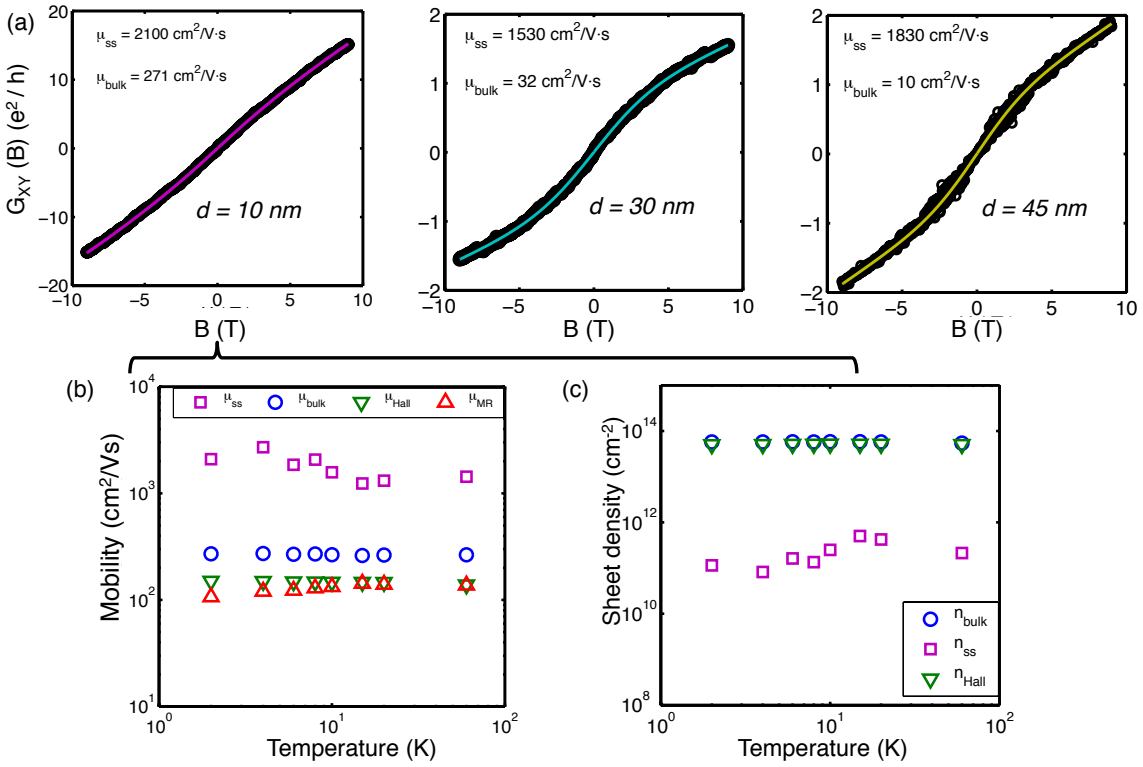

Figure 3.6: (a) Two-channel model fit applied to the Hall conductivity data at 2 K for different devices. (b) Mobilities from the two-channel model compared with the Hall and MR mobilities for different temperatures for $d = 10$ nm. (c) Sheet carrier densities from two-channel model compared with Hall concentration at different temperatures for $d = 10$ nm.[49]

Where n_i, μ_i are the carrier concentration and mobility of the i^{th} channel, respectively. $G_{XX,\ XY}$ are the conductance tensor components. With some basic algebra and limiting assumptions the number of unknown variables in the fit can be reduced and the following equation can be used for a two-channel model:[35]

$$
\begin{aligned}
G_{XY} &= eB\left(\frac{k_1\mu_1 - k_2}{\left(\frac{\mu_1}{\mu_2} - 1\right)\cdot(1+\mu_2^2B^2)} + \frac{k_1\mu_2 - k_2}{\left(\frac{\mu_2}{\mu_1} - 1\right)\cdot(1+\mu_1^2B^2)}\right) \\
k_1 &= G_{XX}(0)/e,\ \ k_2 = \lim_{B\to 0} G_{XY}(B)/eB \\
n_1 &= \frac{k_1\mu_2 - k_2}{\mu_1\mu_2 - \mu_1^2},\ \ n_2 = \frac{k_1\mu_1 - k_2}{\mu_1\mu_2 - \mu_2^2}
\end{aligned}
\tag{3.10}
$$

Fig-3.6(a) shows the two-channel fit to the Hall conductivity data for BTS devices of different thicknesses. For the $d = 10$ nm device, the two mobilities and carrier densities extracted from the model fit are shown in Fig-3.6(b) and (c), respectively, as a function of the temperature compared with the values computed directly from the Hall coefficient. The bulk carrier concentrations from both Hall and two-channel models are close to previously reported carrier densities for bulk crystals showing n-type doping.[55,58] The two-channel model reveals the presence of a higher mobility and lower carrier density surface channel, *i.e.*, μ_{ss}, n_{ss}, whereas the lower mobility and higher carrier density channel, μ_{bulk}, n_{bulk}, is indicative of an effective contribution from the bulk channel. The two-channel model fits the data well up to higher temperatures, where the surface state channel is still found to contribute to the overall conduction, with the bulk conduction states always present.

3.8 Universal conductance fluctuations

Fluctuations in the magnetoresistance are evident for thinner devices, for example in the 10 nm device in Fig-3.4(a) and can be visualized better by subtracting the smooth background from the extended HLN fits (Fig-3.7(a)), seen to be persisting up to higher temperatures. Universal conductance fluctuations (UCF) are a manifestation of an electron's path interfering with itself, as it goes around a defect site. If the phase of the electron is preserved over a mesoscopic scale $\mathcal{L}_\phi$, then the interference leads to measurable variance or fluctuations in the conductance. When the sample dimensions are larger than $\mathcal{L}_\phi$ there is some self-averaging due to changing impurity potential configuration,[94,95] which can reduce the overall amplitude of the fluctuations. To calculate the amplitude, a correlation function of the fluctuations is calculated as:[95] $\mathcal{F}(\Delta B) = \langle \delta g(B) \cdot \delta g(B + \Delta B) \rangle$, where $\delta g = g(B) - \langle g(B) \rangle$ (see Figure-3.8 for examples of the correlation function). The UCF magnitude is obtained at $\sqrt{\mathcal{F}(0)}$ and is of the order of $\sim 0.05\ e^2/h$, decaying as $T^{-0.44}$ from our experimental data (Fig-3.7(c)). This temperature dependence is similar to theoretically expected $1/\sqrt{T}$ dependence in a 2D system.[40,85,86,94,95] The correlation-field B_c (related to the scale of the UCF) can be calculated from the correlation function as $\mathcal{F}(B_c) = \frac{1}{2}\mathcal{F}(0)$ and the related phase coherence length as $L_{\phi,\ UCF} = \sqrt{\Phi_0/B_c}$, where Φ_0 is the flux quantum.[95] As seen in Fig-3.7(c) $L_{\phi,\ UCF}$ matches closely with $L_{\phi,\ HLN}$ and decays

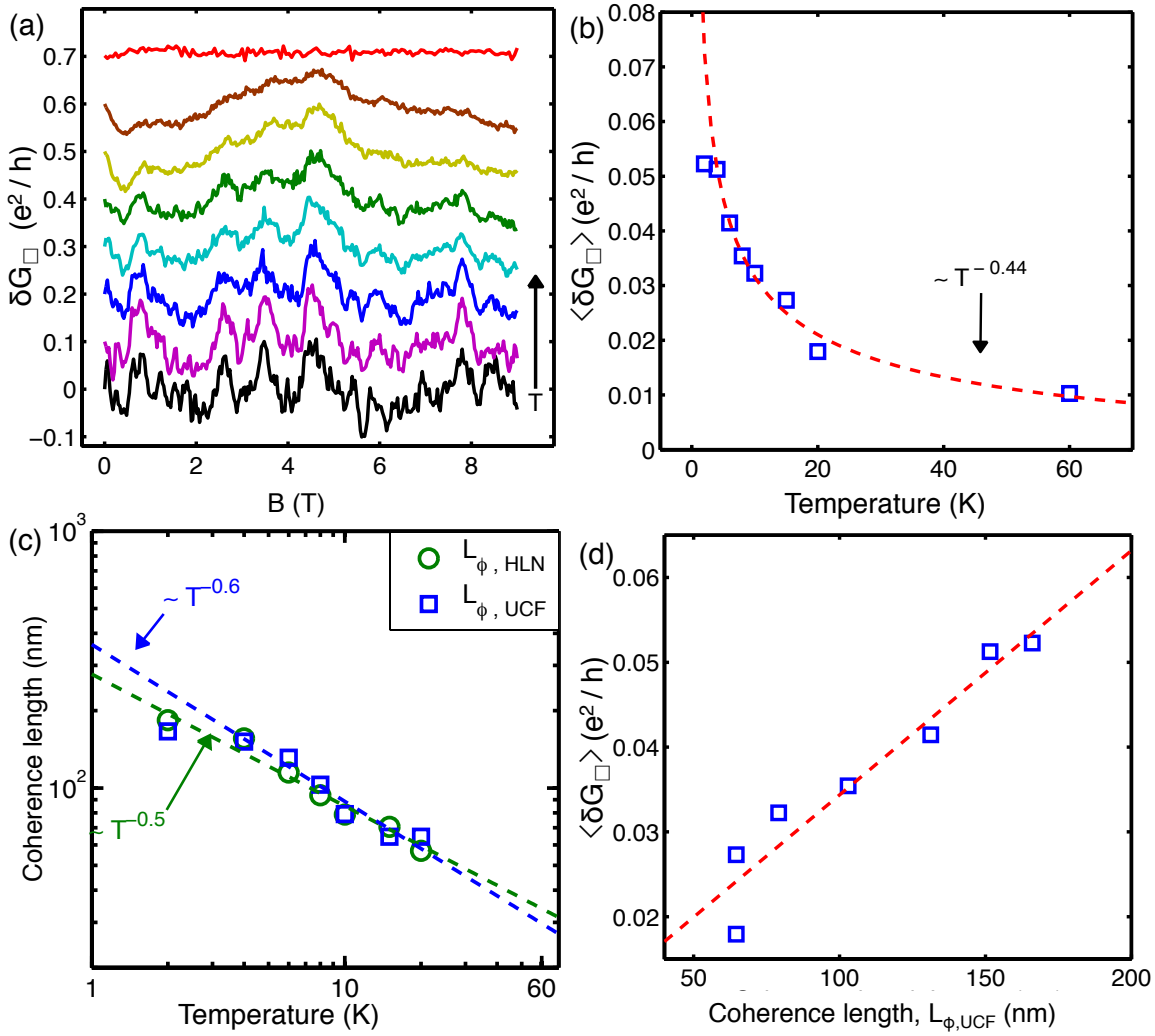

Figure 3.7: (a) Sheet magnetoconductance in $d = 10$ nm device at different temperatures with smooth background subtracted. Curves are shifted for clarity. (b) Magnitude of the fluctuations as a function of temperature, showing a $\sim T^{-0.44}$ behavior expected from 2D UCF theory. (c) Phase coherence length L_ϕ, as extracted from the UCF calculations, compared with the L_ϕ from HLN fitting. (d) RMS values of the fluctuations show linear dependence on the phase coherence lengths.[49]

as $\sim T^{-0.6}$, which confirms that the fluctuations are primarily from the 2D surface channel.[95] Also expected from 2D UCF theory is the linear relation of rms value of the fluctuations with the corresponding phase coherence length[95,96] (see Fig-3.7(d)).

To see the consequence of finite size effects on the UCF magnitudes, devices

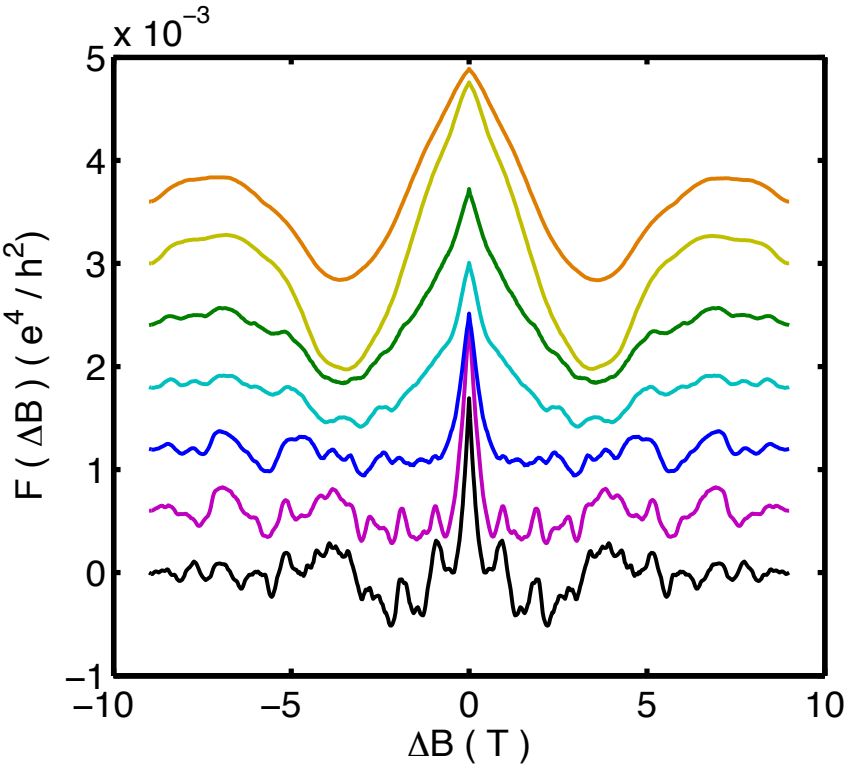

Figure 3.8: Temperature-dependent UCF correlation function $\mathcal{F}$ as a function of the magnetic field shift ΔB (up to 20K).

of different dimensions ($L,\ W$) can be compared for their rms values. For a true comparison the rms value of the UCF within a phase-coherent box $\mathcal{L}_\phi \times \mathcal{L}_\phi$ should be considered, which calculated as $\langle \delta G_\phi \rangle = \sqrt{N}\frac{L}{W}\langle \delta G_\square \rangle$, where $N = LW/L_\phi^2$ is the number of phase coherent boxes in a $L \times W$ sample.[97] Rossi *et al.* have proposed an approach to compare UCF amplitudes in Dirac materials, independent of impurity density, disorder strength and correlation length:[98]

$$\langle \delta G_\phi^2 \rangle = \left(\frac{e^2}{\pi^2 h}\right)^2 \sum_{n_x=1, n_y=-\infty}^{\infty} \frac{12 g_s g_v}{\left(n_x^2 + 4\left(\frac{L}{W}\right)^2 n_y^2\right)^2} \tag{3.11}$$

In Eq-3.11 the spin and valley degeneracies for TI surface channel is $g_s g_v = 1$.[98] Fig-3.9 shows the phase coherent UCF magnitudes of several devices as a function of the dimensional ratio L/W. The red dotted line shows the behavior of a topological surface channel from Eq-3.11; the black dotted line is the expected value of the UCF

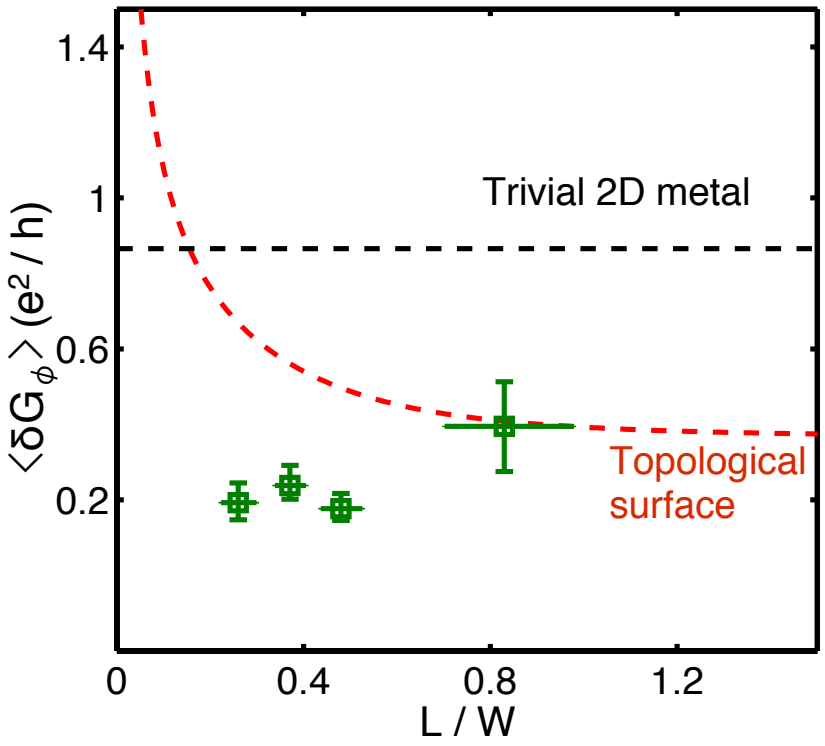

Figure 3.9: UCF magnitude in a phase-coherent box ($\langle \delta G_\phi \rangle$) in several devices as a function of their dimensional ratio L/W. Dashed red line is Eq-3.11.[49]

magnitude ($\approx$ 0.86 e^2/h) for a topologically trivial 2D-electron gas (2DEG).[99,100] The UCF magnitudes are somewhat less than the magnitude expected from topological states according to Eq-3.11, but they are much less than trivial 2D metal values, indicating that the conductivity fluctuations largely arise due to the topological surface states.[100,101]

3.9 Electrostatically gated magnetotransport

The magnetotransport results discussed in detail up to now point towards the existence of readily-accessible surface states in BTS devices, albeit with parallel contribution from bulk channels. Temperature dependent conductivity, EEI effects, temperature dependent WAL analyzed with an extended-HLN model and 2D universal conductance fluctuations are observed in BTS devices. Each of these physical

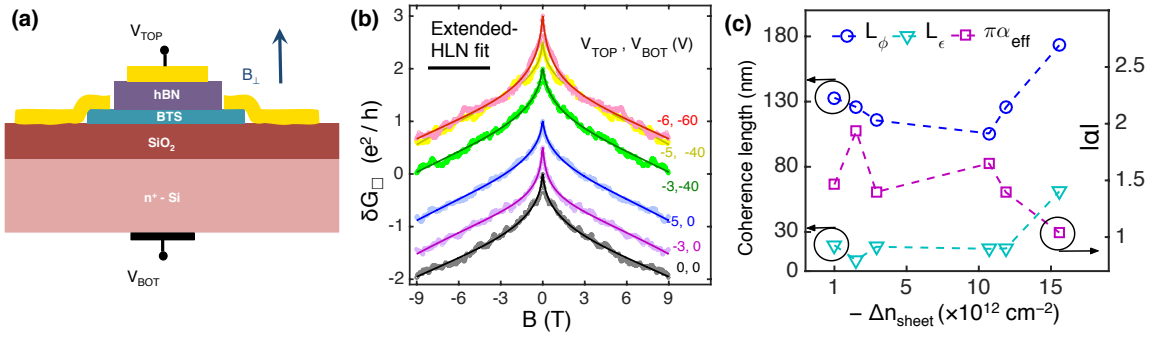

Figure 3.10: (a) Schematic of the dual-gated BTS device. (b) Longitudinal MR for different electrostatic biases and their extended HLN fits. The gate-bias combinations are shown next to their corresponding curves in the same color. (c) Coherence lengths and effective prefactor as a function of the electron density in the device.

effects are dependent on the carrier density in the device, the type of carriers and the contribution of the bulk. These factors can be modified controllably by applying electrostatic gate bias to the BTS devices, as has been successfully demonstrated in literature on devices of other 3DTI materials.

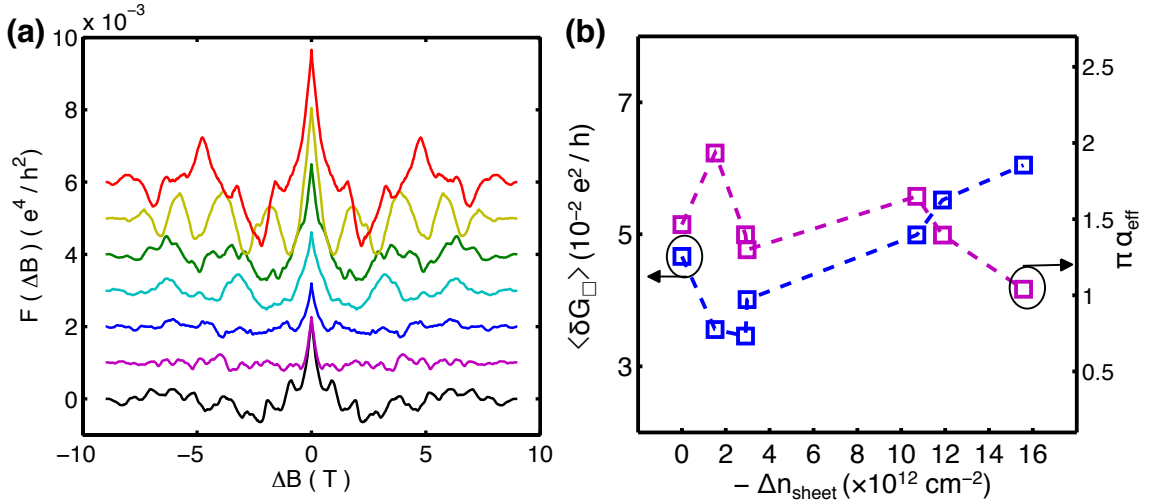

Figure 3.11: (a) The UCF correlation function for different gate biases. The color scheme is consistent with Fig-3.10. (b) Magnitude of the UCF as a function of the density in the device. Effective prefactor values are also shown for reference.

We have performed preliminary transport measurements on a dual-gated BTS

device. The device structure was fabricated by transferring a thin flake (∼15 – 20 nm) of exfoliated-hBN on a Hall bar BTS device using a PDMS stamp method, and patterning a Ti/Pd metal gate on it.[102] The SiO_2 film (growth substrate) and the doped bulk n^+-Si are used as the backgate. The sample was then measured in a similar fashion as that described in Section-3.2.2. The gate-voltages are supplied by HP 4140b SMU's. Typical top-gate and bottom-gate voltages are in the range of -10 to 10 V and -80 to 80 V, respectively. Good devices showed gate-leakage currents in the pA range. The schematic of the fabricated dual-gated BTS device is shown in Fig-3.10(a). The four-point magnetoresistance was measured as a function of different gate-voltages. As seen from Fig-3.10(b) application of a more total negative gate bias on both the gates leads to a sharper WAL signature and more prominent fluctuations (lighter circles represent measured data). The extended-HLN fit of Eq-3.6 also fits the gate-dependent magnetoconductance data fairly well, as shown by the darker lines. Fig-3.10(c) shows the characteristic lengths L_ϕ, L_ε and $\pi\alpha_{eff}$ from the extended fit as a function of the negative relative sheet carrier density in the device calculated from Hall data, *i.e.*, $-\Delta n_{sheet} = n_{sheet}(0) - n_{sheet}(V_g)$, such that the carrier density in the device is decreasing towards right. Two regions can be considered in the plot: the top-gate only region ($-\Delta n_{sheet} < 4 \times 10^{12} cm^{-2}$) and top+bottom gate region ($-\Delta n_{sheet} > 8 \times 10^{12} cm^{-2}$). The first region shows the value of $\pi\alpha_{eff} > 1$ and the phase coherence length L_ϕ decreasing at first, with the fourth data point as a bit of an outlier. As carriers are further depleted through biasing of the back-gate, a more coherent picture arises in the second region: $\pi\alpha_{eff} \to 1$, and L_ϕ steadily increases. This behavior can be understood as a separation of the multiple conduction channels in the device, including top and bottom surfaces, bulk and scattering channels, with eventually one surface channel in the WAL correction ($\alpha_\phi \sim 1/2\pi$) and the other surface channel's contribution lumped in with the bulk and scattering channels.

Electrostatic gating also leads to measurable change in the UCF observed in the longitudinal MR of the dual-gated device, as shown in Fig-3.11. Fig-3.11(b) shows the effect of the gate-bias on the UCF amplitude, compared with the trend in the prefactor $\pi\alpha_{eff}$ from the extended HLN fits. As a more negative gate-bias is applied, the contribution of the primary surface channel dominates over that of the bulk (*i.e.*, $\alpha_{eff} \to 1$ or $\alpha_\phi \sim 1/2\pi$) and the measurable rms value of the UCF amplitudes increases. This may be explained as an increase in the mesoscopic scale $\mathcal{L}_\phi$, over

which the fluctuations are phase-coherent, and a decrease in scattering contribution from the bulk.

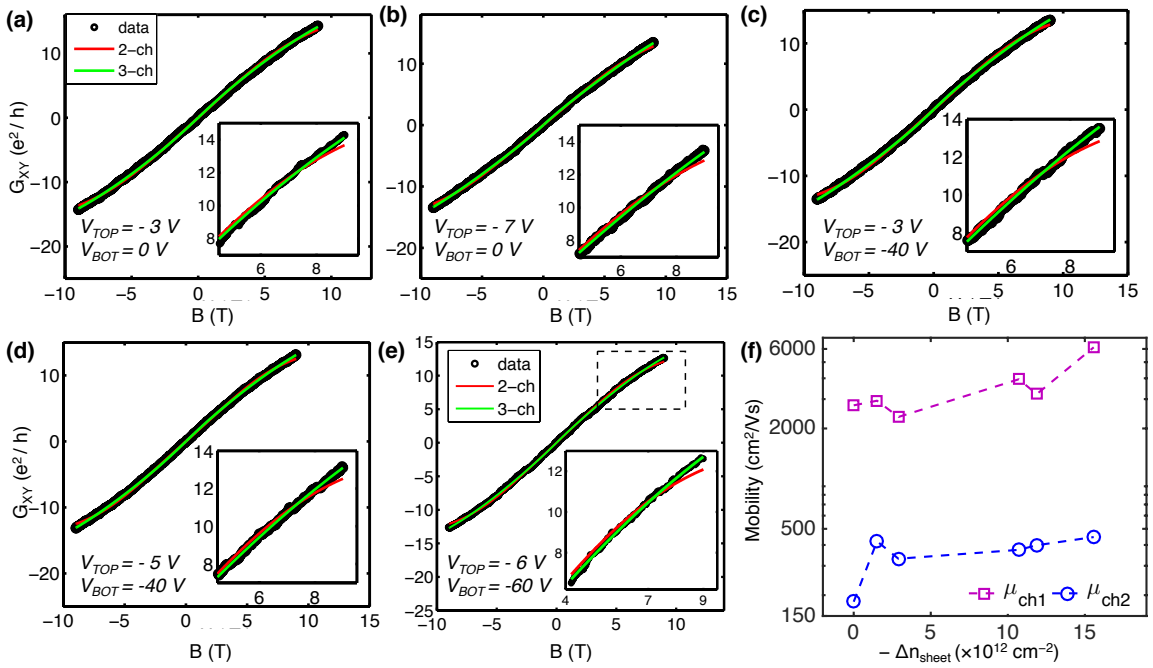

Figure 3.12: (a) – (e) Device Hall conductance (back circles) for several different electrostatic gating combinations, as displayed in the figure insets. The solid red curves are fits to the two-channel conductivity model of Eq-3.10, and the solid green curves are fits to the three-channel conductivity model of Eq-3.15. (f) Mobility values extracted from the three-channel model as a function of the device density. The third channel mobility largely remains flat at a low value in the range of $20 - 50$ cm^2/V·s.

The separation of channels interpretation in the dual-gated device is further supported by fitting the G_{xy} data at different gate biases as shown in Fig-3.12. The two-channel model provides an unsatisfactory fit, unlike in the zero-bias temperature-dependent case. We have considered a model with three conduction channels as an alternative explanation, which fits the gate-dependent G_{xy} better than the two-channel model as seen from Fig-3.12(a) – (e). The three-channel model is derived as follows.

3.9.1 Three-channel Hall conductivity model

Starting from the generic multi-carrier model from Eq-3.9 for three channels:

$$G_{XX} = e\sum_{i=1}^{3} \frac{n_i \mu_i}{1+\mu_i^2 B^2},\ G_{XY} = eB\sum_{i=1}^{3} \frac{n_i \mu_i^2}{1+\mu_i^2 B^2} \tag{3.12}$$

Along with the limiting assumptions from,[35] *i.e.*, the k_1, k_2 variable assignments in Eq-3.10, a third assumption can be made: $\sum_i n_i = n_{Hall}$, where n_{Hall} is the Hall carrier concentration calculated directly from the as-measured Hall-coefficient. Assigning $k_0 = n_{Hall}$, the three reduction variables are:

$$\begin{aligned} k_0 &= n_{Hall} = n_1 + n_2 + n_3, \\ \text{For } B = 0,\ k_1 &= n_1\mu_1 + n_2\mu_2 + n_3\mu_3 = G_{XX}(0)/e, \\ \text{As } B \to 0,\ k_2 &= n_1\mu_1^2 + n_2\mu_2^2 + n_3\mu_3^2 = \lim_{B\to 0} G_{XY}(B)/eB \end{aligned} \tag{3.13}$$

Eq-3.13 can be used to eliminate n_i's (in favor of μ_i's), and obtain them as a function of K_i and μ_i:

$$\begin{aligned} n_1 &= \frac{k_2 - k_1(\mu_2+\mu_3) - k_0\mu_2\mu_3}{(\mu_1-\mu_3)(\mu_1-\mu_2)} \\ n_2 &= \frac{k_2 - k_2(\mu_3+\mu_1) - k_0\mu_3\mu_1}{(\mu_1-\mu_2)(\mu_3-\mu_2)} \\ n_3 &= k_1 - \frac{k_2 - k_1(\mu_1+\mu_2) + k_0\mu_3(\mu_3-\mu_2-\mu_1)}{(\mu_1-\mu_3)(\mu_2-\mu_3)} \end{aligned} \tag{3.14}$$

Substituting the expressions from Eq-3.14 into Eq-3.12:

$$\begin{aligned} G_{XY} = eB \cdot \Bigg[&\frac{k_2 - k_1(\mu_2+\mu_3) - k_0\mu_2\mu_3}{(\mu_1-\mu_3)(\mu_1-\mu_2)(1/\mu_1^2 + B^2)} + \frac{k_2 - k_1(\mu_3+\mu_1) - k_0\mu_3\mu_1}{(\mu_1-\mu_2)(\mu_3-\mu_2)(1/\mu_2^2 + B^2)} + \\ &\frac{1}{(1/\mu_3^2 + B^2)}\left(k_0 - \frac{k_2 - k_1(\mu_1+\mu_2) + k_0\mu_3(\mu_3-\mu_2-\mu_1)}{(\mu_1-\mu_3)(\mu_2-\mu_3)}\right)\Bigg] \end{aligned} \tag{3.15}$$

The three-channel fit of Eq-3.15 is applied to the electrostatic gate-dependent

G_{XY} data in device D2. Fig-3.12 shows the fitted data, as compared with the two-channel model of Eq-3.10. Three-channel model provides a better fit. When the back-gate bias is applied (Fig-3.12(c) – (e)) the limitation of the two-channel fit is more apparent compared to when only the top-gate bias is applied (Fig-3.12(a,b)).

The three mobilities obtained from the model are shown in Fig-3.12(f) as a function of $-\Delta n_{sheet}$. The high-mobility channel (μ_{ch1}) can be understood as the aforementioned dominant surface state, the moderate mobility channel (μ_{ch2}) as the secondary surface channel and the low mobility channel (μ_{ch3}) as the bulk scattering component. The three mobilities show a two-region behavior similar to L_ϕ, α_ϕ, where the high and moderate mobility channels show a steady increase and the low-mobility channel stays relatively unchanged. For devices of layered van der Waals materials on a dielectric substrate, bottom layers closer to the substrate typically have lower mobilities compared to the top layers, largely due to charge impurity-dominated scattering from the substrate and other surface roughness related scattering.[103] Similarly, the high (moderate) mobility channel μ_{ch1} (μ_{ch2}) may be interpreted as the contribution from the top (bottom) surface in this case. The L_ϕ from the extended HLN model can be considered as arising from the contribution of the top surface channel, as the number of channels contributing to the WAL conductivity correction approaches one, *i.e.*, $\pi\alpha_{eff} \to 1$ or $\alpha_\phi \sim 1/2\pi$.

As a next step, transport in hBN encapsulated BTS devices can be considered for future work. Such a device can be constructed by stamp transferring hBN layers on fabricated devices on BTS nanosheets, which are in-turn grown on exfoliated hBN as shown in Fig-2.3. The benefit of such a device structure can be twofold: firstly, due to the crystalline nature of hBN used as the growth substrate, the BTS nanosheets grown on top would be expected to have less defects related to the substrate roughness when compared to BTS-on-SiO_2. Secondly, hBN encapsulation for devices of 2D materials such as graphene and MoS_2, has been shown to increase the mobility by reducing substrate related scattering and the low-κ dielectric environment.[103] A similar effect is expected in hBN-encapsulated BTS devices, which would lead to cleaner transport signatures that can be analyzed with our extended-HLN and multi-channel conductivity models. Once a prototype encapsulated device is demonstrated, a more detailed research project can be to extend it to large-area devices of vdWE grown BTS on CVD-grown large area hBN films.

Chapter 4

Custom-Feature van der Waals Epitaxy: Growth Process and Characterization

This chapter describes the versatile, large-area custom-feature van der Waals epitaxy growth method developed for TI growth on prepatterned mica substrates and materials characterization.

4.1 Introduction

Since the early discovery and demonstration of the staple TI compounds the focus of research has evolved on several fronts. Demonstrations of scalable device applications remain challenging to this day, however, with a dearth of repeatable and adaptable thin film synthesis techniques being amongst the primary reasons.[3,104] There are three well-established mechanisms to obtain high quality crystalline thin film topological materials: bulk crystals and their exfoliation,[29,40,44,105] molecular beam epitaxy (MBE),[35,36,38,43,106] and sub-atmospheric hot-wall van der Waals epitaxy (vdWE).[45–49] The latter two are the only realistic contenders for scalable implementation. While MBE offers high quality crystalline films with a fine control over film thickness, there are limiting factors such as complexity and cost of ultra-high vacuum systems, substrate choice, difficulty of ternary/quaternary compound growth and incompatibility with high vapor pressure compounds (*e.g.*, sulfides).[50] On the other hand, as described previously, vdWE offers a low-cost, facile alternative, accommodating more source, substrate, and compound thin film combinations,[51,52] but the control over film thickness and area remains challenging. An optimal balance must be achieved to explore alternatives addressing the challenges of scalability and reliability of TI synthesis for practical applications.

Selective-area growth (SAG) for compound III-V semiconductors has received a great deal of attention since the late 70's owing to adaptability and ease of im-

Results discussed in this chapter were published in ACS Nano. Contributions: Primary author. Designed and built the growth system, developed the custom-feature patterning process, carried out the growth experiments, performed materials characterization analysis. Citation: T. Trivedi, A. Roy, H. C. P. Movva, E. S. Walker, S. R. Bank, D. P. Neikirk, and S. K. Banerjee, "Versatile Large-Area Custom-Feature van der Waals Epitaxy of Topological Insulators," *ACS Nano*, vol. 11, no. 7, pp. 7457–7467, Jul. 2017, Available: `http://dx.doi.org/10.1021/acsnano.7b03894`.

plementation.[107–110] SAG methods rely on patterning the substrate prior to growth, conventionally with an inert hard mask such as thin films of SiO_2 or SiN_x, such that only certain regions of the substrate are accessible where the deposition and/or growth will occur. The hard masks are usually patterned with shadow masks or standard lithography. Test growth structures often involve array of holes in the hard mask film, of different shapes, sizes and with varying pitches. For metal-organic chemical vapor deposition (MOCVD) SAG methods, geometrical dependence of growth results is observed.[108,110,111] SAG processes for TIs have only recently started attracting focus and the field is in its nascent stage, with proposed methods such as shadow-masked pattern and polymer imprint based local chemical modification with solvents or self-assembled molecules.[112–116] The proposed methods are able to demonstrate the basic SAG of TI, however, the control over features sizes/shapes and overall process integrability is suboptimal: shadow masks have feature size restrictions and polymer stamp based imprint lithography involves specialized tools and added fabrication steps that introduce sources of process variability. Most reported methods also do not delve into the details of the growth mechanism and the kinetics of the TI SAG. There is undoubtedly a need for fully integrable processes utilizing standard microfabrication technology to obtain large-area TI films, especially ternary and quaternary compounds, for electronic, spintronic and optoelectronic device applications. Such processes must be versatile enough to span the spectrum from academic and prototype research to scalable manufacturing. Simultaneously, unraveling the details of the growth mechanism is a necessary and significant advancement towards optimization and customization of TI SAG processes, and their extension to a larger set of compound and substrate combinations for future research and development.

As the natural next step towards technological relevance, a versatile process for large-area, crystalline TI growth in customizable features on mica is presented, called custom-feature van der Waals epitaxy (CF-vdWE).[117] The TI features grow epitaxially in large single-crystal trigonal domains of several microns in size and in any arbitrary shape of linear dimensions up to the order of 100μm. A nonlinear thickness dependence on lateral dimensions is observed along with denuded zones at boundaries, which are explained with a semi-empirical surface migration model providing insights into the underlying growth mechanism, and the role of the selective-area surface modification. The subsequent mask layers for device fabrication can be

effortlessly integrated post-growth using standard photolithography. DC transport on directly-grown TI Hall bars of different dimensions show metallic conduction down to 77 K, and the device sheet conductance remains remarkably flat with increasing TI Hall bar thickness at room temperature across several samples, indicating that the transport is dominated by the metallic topological surface states (TSS) with a low bulk contribution.

4.2 CF-vdWE process

The 7-step fabrication and growth process for the custom-feature TI growth on pre-patterned mica substrates is schematically represented in Fig-4.1. Customization of the process for other substrates and growth compounds is possible by introducing or removing appropriate fabrication steps depending on the engineered surface requirements for the substrate/compound combination.

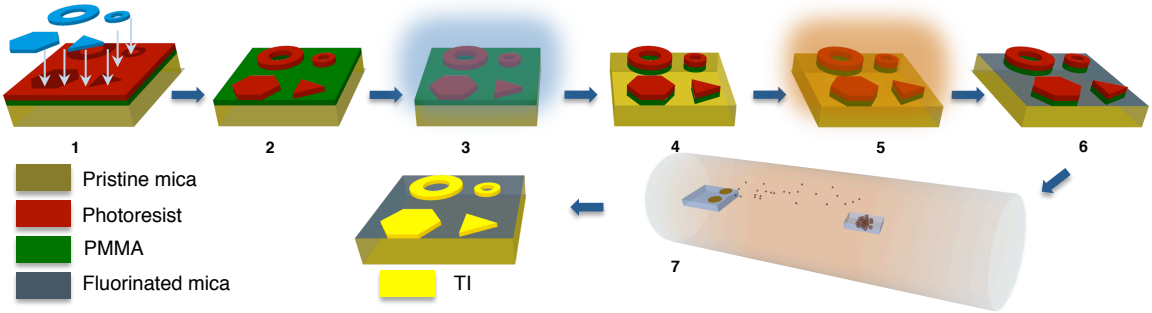

Figure 4.1: Custom-feature van der Waals epitaxy (CF-vdWE) process flow schematic.[117]

4.2.1 Lithographic modification of mica substrates pre-growth

- **Step 1**:
  - Muscovite mica disks of 10-25 mm diameter (Ted Pella Inc.) were cleaved along the (0 0 1) plane immediately prior to the process using a clean scalpel.

- A layer of PMMA A4 (MicroChem) was spin-coated at 4k rpm on the freshly cleaved substrates and baked at 180 °C, followed by a layer of AZ 5209E photoresist (PR) spin-coated at 4k rpm, baked at 90 °C.
- A mask aligner with an i-line UV source at 7.5 mW/cm^2 intensity was used to expose a custom-designed pattern from a photomask onto the mica substrate with the dual-resist layers in vacuum contact mode.

- **Step 2**: The PR layer was developed using a standard 2.3% tetramethylammonium hydroxide (TMAH) developer (Dow MF-26A). As the cleaved muscovite mica surface contains Al and Si oxides,[118] it reacts with TMAH if exposed directly and is slowly etched, leading to low-yield in a single layer resist process. The PMMA layer, which is inert to TMAH, protects the mica surface during development and prevents unexposed PR from peeling off. The bilayer resist process dramatically improves lithography yield.

- **Steps 3 − 6**: The substrates were loaded into an RIE plasma chamber (Plasmatherm 790) for a dual-step plasma process. Test mica substrates without any lithographic patterns were also loaded into the RIE chamber, to be used later for contact-angle measurements.

  - *Steps 3, 4*: 100 W oxygen plasma process to transfer the patterns from the PR to the PMMA film underneath
  - *Steps 5, 6*: Without breaking vacuum, 100 W CF_4 plasma process to fluorinate the exposed mica surface. The substrates were then cleaned in hot NMP (Remover PG, MicroChem) overnight to remove resist and other organic contaminants.

4.2.2 van der Waals epitaxial growth and materials characterization

The cleaned fluorinated mica substrates were loaded into the vdWE growth furnace, described in detail in Chapter 2. The precursor materials in the central zone were ramped up to 510 °C, such that the sublimated vapor flux is carried over to a cold zone of the furnace by an inert carrier gas (N_2), where the pre-patterned clean mica substrates were horizontally arranged. The substrate temperature was typically

in the range of 390 – 410 °C, the chamber pressure was maintained at 20 – 50 Torr and the N2 gas flow rate was typically 100 – 150 sccm. The central zone temperature was held constant typically for 5 – 20 minutes, before cooling down naturally to room temperature (Step 7). The composition post-growth was confirmed by XPS analysis (SCALAB Mark II Omicron) on the mica substrates. Sample-wide crystallinity of the CF-vdWE grown features was determined with XRD (Philips X'Pert) and locally with scanning Raman spectroscopy (Renishaw inVia). An in-house goniometer with a digital camera was used for measuring the contact angle of water on test mica substrates before and after the CF4 plasma process to establish the surface free energy difference. Tapping mode AFM (Veeco Nanoscope V) was used to extensively image the grown features locally, and to extract thickness distributions, domain sizes and orientations, and exclusion zone boundaries. Statistics, image analysis and fitting were performed with MATLAB. Open source SPM software Gwyddion was utilized for processing acquired AFM data.[119]

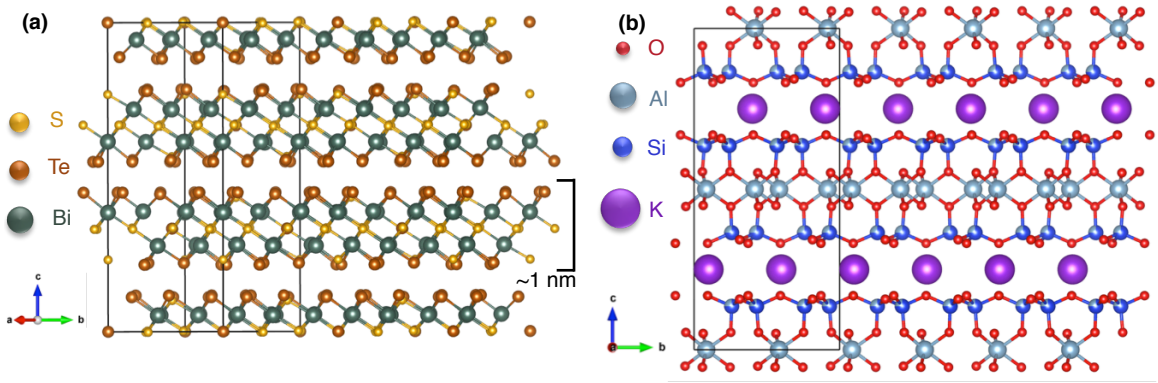

Figure 4.2: Crystal structure and unit cell of (a) BTS, and (b) muscovite mica. Orientation is indicated with the axes for both crystals. Crystal structures were visualized with VESTA 3.[53]

4.3 Growth results

Muscovite mica is a layered inorganic compound that cleaves readily out of plane, breaking bonds at the potassium layer,[118] revealing an atomically flat and smooth single-crystal (0 0 1) plane (see Fig-4.2) and providing an excellent surface

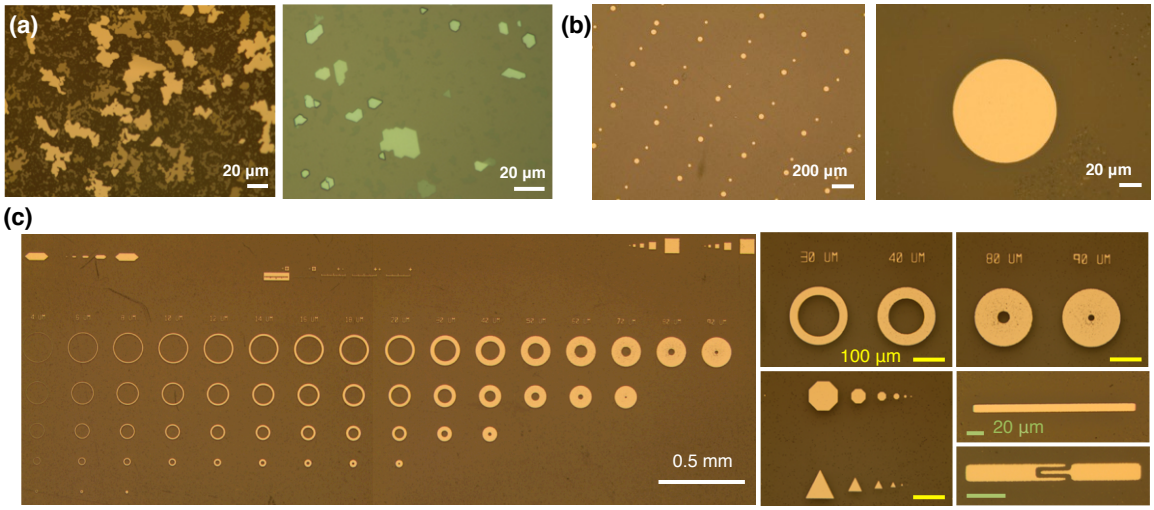

Figure 4.3: (a) Optical images of BTS nanosheet growth on un-patterned pristine mica. (b) Optical image of CF-vdWE grown Bi_2Te_3 circles. (c) Optical image of various CF-vdWE grown BTS shapes.

for TI compound growth.[48,120] While there is a large lattice mismatch (24%) between mica (a = 5.2 Ą) and BTS (a = 4.2 Ą), due to the weak substrate dependence of vdWE,[52] layer-by-layer epitaxial growth of BTS on mica can still be obtained similar to the case of SiO_2, albeit with larger and more oriented domains (see Fig-4.3(a) for BTS growth on un-patterned pristine mica). The process is constructed from readily integrable steps: standard photolithography, reactive plasma etching, standard solvent cleans, and hot-wall vdWE growth of Bismuth Telluro-Sulfide ($Bi_2Te_{2-x}S_{1+x}$, $0.2 \leq x \leq 0.5$) or BTS. The CF-vdWE process can nevertheless be easily extended to other TI compounds in the Bi/Sb family, simply by altering the precursor material combinations in the vdWE step (see Fig-4.3(b) for examples of CF-vdWE grown Bi_2Te_3). The CF-vdWE process results in large-area contiguous BTS films highly confined within the feature boundaries, as seen in Fig-4.3(c). The TI material grows in virtually any shape as predefined by the lithographically masked plasma process. The typical growth mask used in this experiment involves a matrix of rings or annuli of different widths (increasing from left to right) and different outer diameters (decreasing from top to bottom), as shown in Fig-4.3(c). A variable annulus pattern matrix is chosen in order to study the dependence of the process on lateral dimensions and the pitch of an array of features, eliminating the need to pattern several different

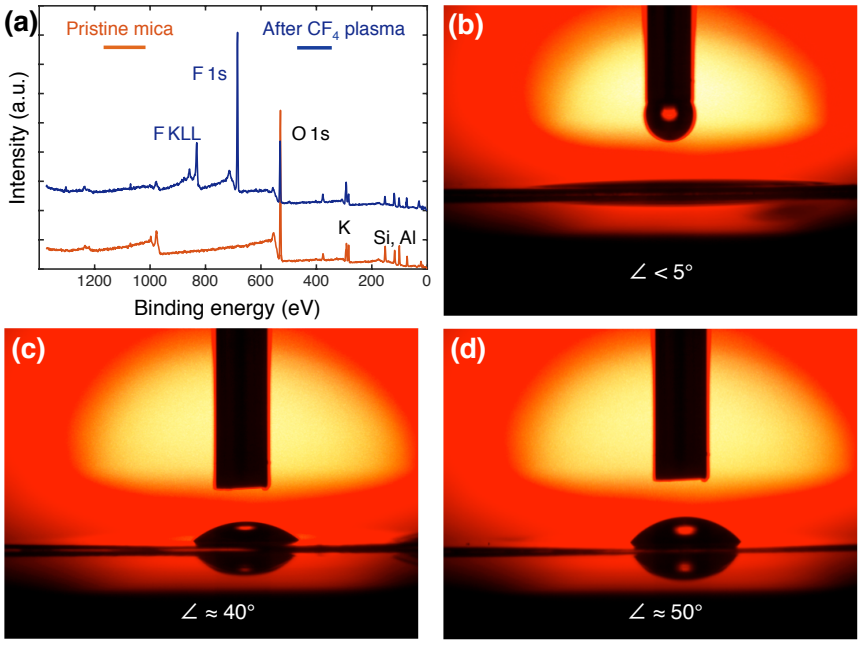

Figure 4.4: (a) XPS spectra on muscovite mica before and after the CF_4 plasma process. Large F-peaks are observable, indicating surface fluorination. Contact angle images of water droplets on (b) pristine mica, (c) mica after 50 W RIE CF_4, and (d) 100 W RIE CF_4 process.

shapes with varying sizes and pitches.

4.3.1 Mica surface free energy modification *via* fluorination

Remarkably, there is virtually no growth outside the feature boundaries in the CF_4 exposed mica regions even for growth times as long as 20 minutes, except for negligible deposition near localized physical defect sites. If the plasma process were to merely induce physical damage on the surface, the overall adhesion would be expected to improve with more growth or deposition around dislocations and defects.[122] The absence of any significant growth in areas as large as a few millimeters points to an alternative mechanism, which overcompensates for any improved adhesion. Such a mechanism must be chemical in nature, resulting in a reduction of the sticking probabilities of one or more constituent adatoms, preventing nucleation and/or compound formation. Indeed, the CF4 plasma process results in a fluorination of the exposed mica surface as observed in comparative X-ray photoemission

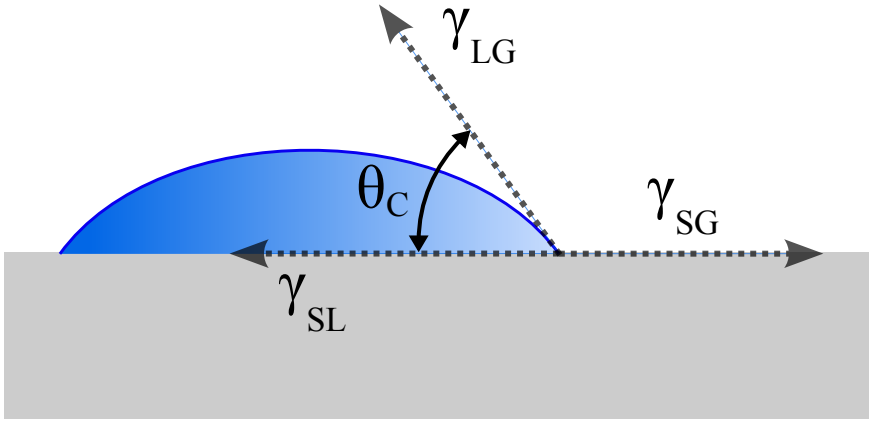

Figure 4.5: Contact angle of a water droplet on a hydrophobic surface, showing the surface energy components of the Young equation.[121]

spectroscopy (XPS) analysis shown in Fig-4.4(a). Large F-peaks are observed in the XPS spectrum from a mica substrate following the plasma process, which are absent in the spectrum of pristine mica. The peaks do not disappear after standard cleaning or after the high-temperature furnace growth step, indicating that the surface remains fluorinated likely due to a deposition of a fluorocarbon sheath.[118,123] Pristine mica is fairly hydrophilic,[118] causing almost complete wetting of a water droplet on the surface, while the same substrate treated with a blanket CF_4 plasma exposure results in an increased contact angle of water (see Fig-4.4(b)-(d) for contact angle images). This is due to a reduction in the surface free energy of the fluorinated mica surface,[124] which in turn results in significant reduction in adhesion of water or the TI compound on fluorinated mica. The surface free energy of a water droplet on a hydrophobic surface can be described by the Young equation:

$$\gamma_{\mathrm{SG}} = \gamma_{\mathrm{SL}} + \gamma_{\mathrm{LG}} \cdot \cos\,\theta_c \tag{4.1}$$

$\gamma_{\mathrm{SG,\,SL,\,LG}}$ are the solid-vapor, solid-liquid and liquid-vapor interfacial energies, respectively, while θ_c is the contact angle of the water droplet on the surface, schematically illustrated in Fig-4.5. As a surface becomes more hydrophobic the surface free energy further reduces, leading to an increase in the measured contact angle θ_c according to Eq-4.1. Reduction in surface free energy due to plasma-related flu-

orination has been observed in several experiments.[118,123,125] Thus, highly selective growth of the TI compound is achieved, as the artificial boundary condition due to selective surface fluorination leads to an engineered surface for large-area crystalline growth well confined within the pristine mica regions.

4.3.2 Materials characterization

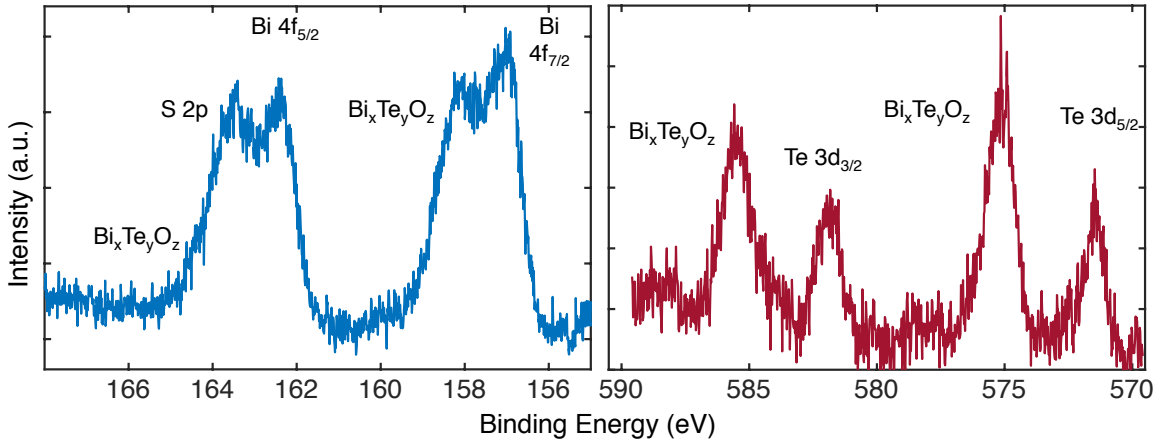

Figure 4.6: XPS of a representative CF-vdWE grown BTS TI sample showing the (e) Bi, S peaks and (f) Te peaks. Surface oxidation related peak splitting is visible.

Compositional analysis on candidate CF-vdWE grown BTS TI smaples is confirmed with XPS as shown in Fig-4.6, showing similar results as vdWE grown BTS nanosheets on SiO_2 (Fig-2.5(b),(c)). As with the case of BTS nanosheets, the CF-vdWE TI features also exhibit evidence of surface oxides that is evident from the peak splitting in the XPS data. The composition of the CF-vdWE grown BTS films across different growth runs remains within the narrow range of stoichiometry $Bi_2Te_{2-x}S_{1+x}$, $0.3 \leq x \leq 0.4$, which is referred to as the γ-phase of the BTS. The tetradymite compound has been previously largely explored only from bulk crystal growths. The data in literature on synthetic crystals of tetradymite is limited, main works being those of Glatz (1967),[56] Soonpaa (1962)[55] and more recently, Ji et al. (2012).[58] Refer to Section-2.3.3 for a more detailed discussion on BTS compound stochiometry and the stability of the γ-phase. X-ray diffraction (XRD) patterns of CF-vdWE grown BTS thin film features show very sharp peaks, appearing only at the (0 0 n) facet reflections

of the bulk tetradymite crystal structure, as shown in Fig-4.7, pointing to a highly c-axis oriented and layer-by-layer growth.[49] Further confirmation of crystallinity and uniformity of the TI is obtained from localized Raman spectroscopy as shown in Fig-4.8. Fig-4.8(a) shows the representative Raman spectrum of a CF-vdWE grown BTS TI annulus, matching with the Raman spectra of vdWE grown BTS nanosheets on SiO_2 (Fig-2.5(d)). A scanning Raman measurement is also performed on the TI annulus (Fig-4.8(b)), and the spectra are fitted with Lorentzians to obtain the full-width half-max (FWHM) spatial distribution of the A^1_{1g}, E^2_g, and A^2_{1g} peaks, as shown in Fig-4.8(c). The XY-mapped FWHM shows good uniformity across the scanned region, confirming good crystalline quality locally in addition to excellent crystalline quality observed globally in the XRD pattern.

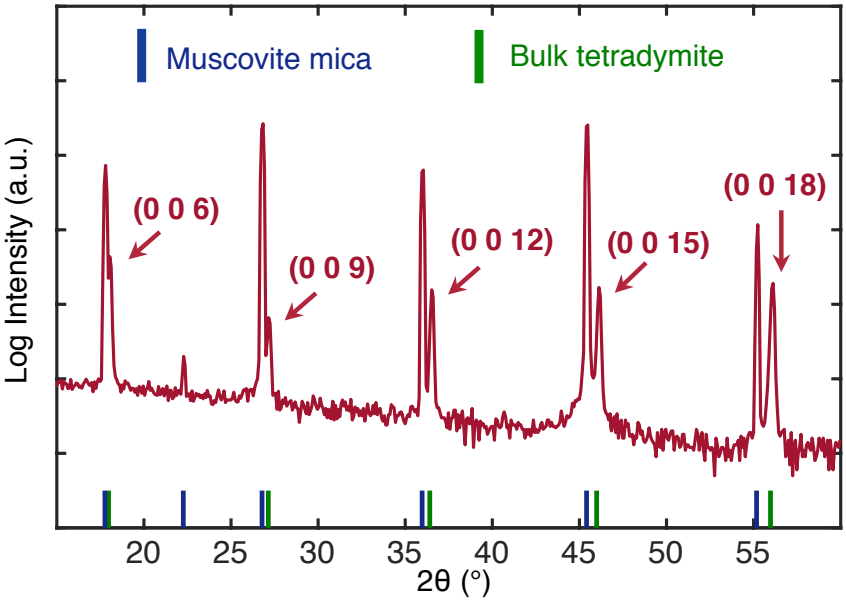

Figure 4.7: XRD pattern of a candidate CF-vdWE grown BTS TI on prepatterned mica.

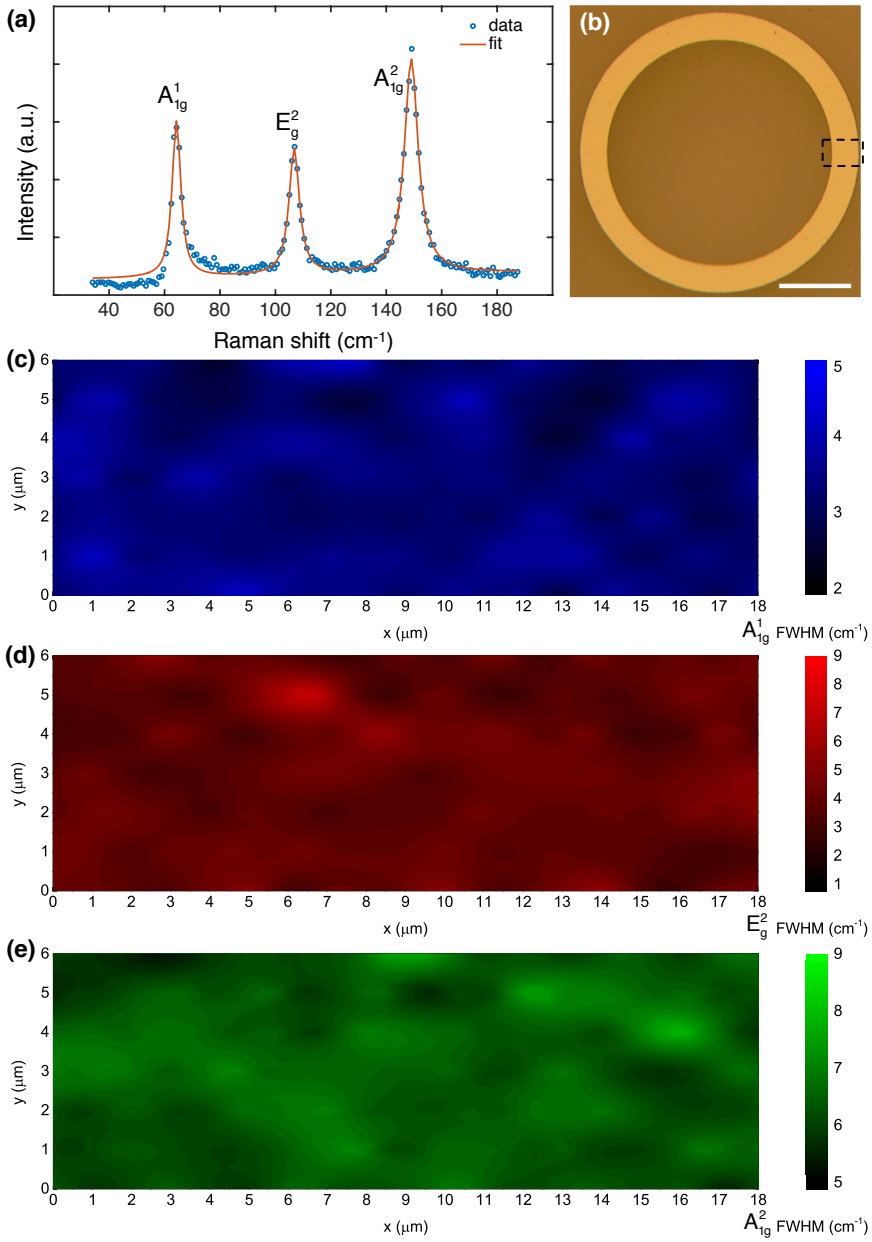

Figure 4.8: (a) Representative Raman spectrum of a BTS TI annulus. (b) Optical image of a TI annulus, showing the region where 2D mapped Raman spectra were measured with a dashed black box (scale bar is 50 μm). (c) Smoothed XY maps of fitted FWHM for A^1_{1g}, E^2_g, and A^2_{1g} peaks, showing good uniformity.

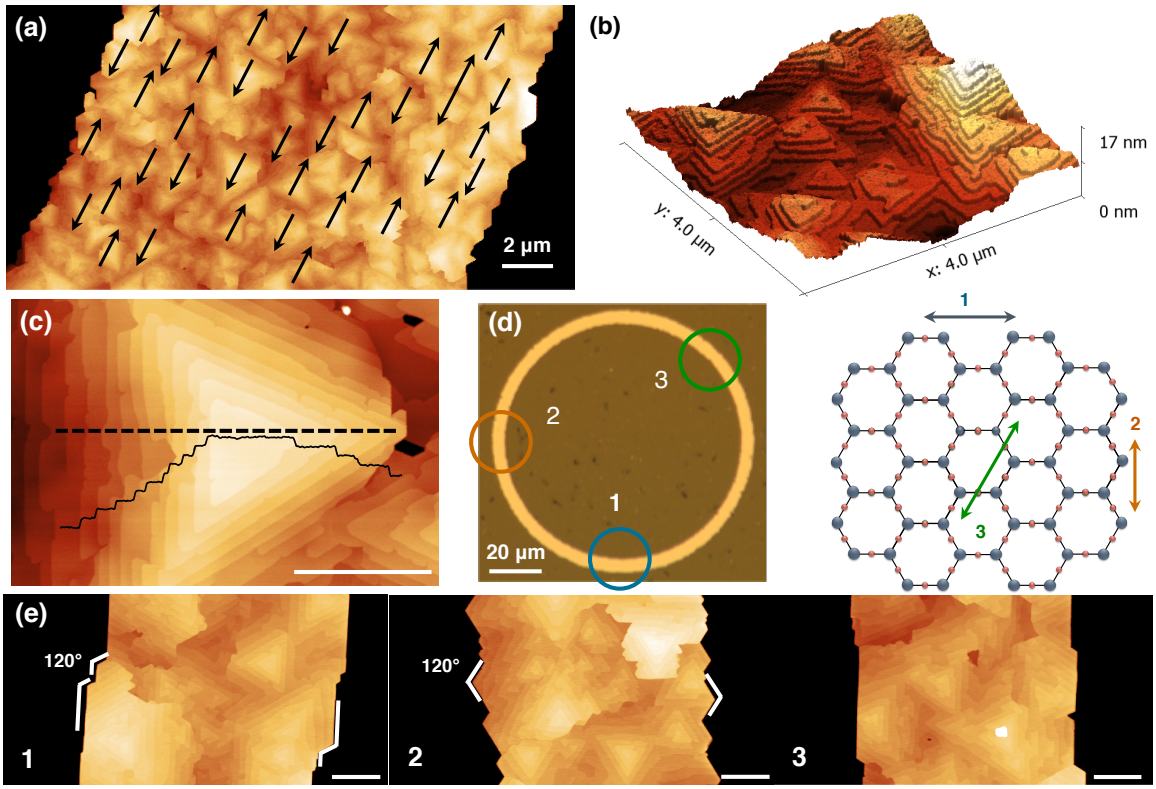

Figure 4.9: (a) AFM image of a CF-vdWE grown TI annulus of 18 μm width and 200 μm outer diameter. Large, layered trigonal domains are oriented in only two directions offset at 180°. All scalebars are 1 μm unless specified. (b) 3D AFM height profile showing highly terraced and oriented growth. (c) A typical trigonal domain and its height profile along the dashed line with ≈1nm steps. (d) Optical image of a TI annulus (left). Circles indicate different locations along the perimeter, corresponding to orientations of the mica lattice underneath (right). (e) Location dependence of armchair-like, zigzag-like and almost straight edges of TI annuli.[117]

4.4 AFM imaging and analysis of CF-vdWE TI

AFM imaging reveals several outstanding features as shown in Fig-4.9. A typical AFM height profile of a section of a BTS annulus is shown in Fig-4.9(a). The structure is composed of highly terraced single-crystal trigonal domains, extending up to several microns in lateral dimensions, which merge together to form the contiguous BTS annulus. A striking characteristic evident from AFM images is that the trigonal domains grow in one of only two orientations mirrored at 180°, sug-

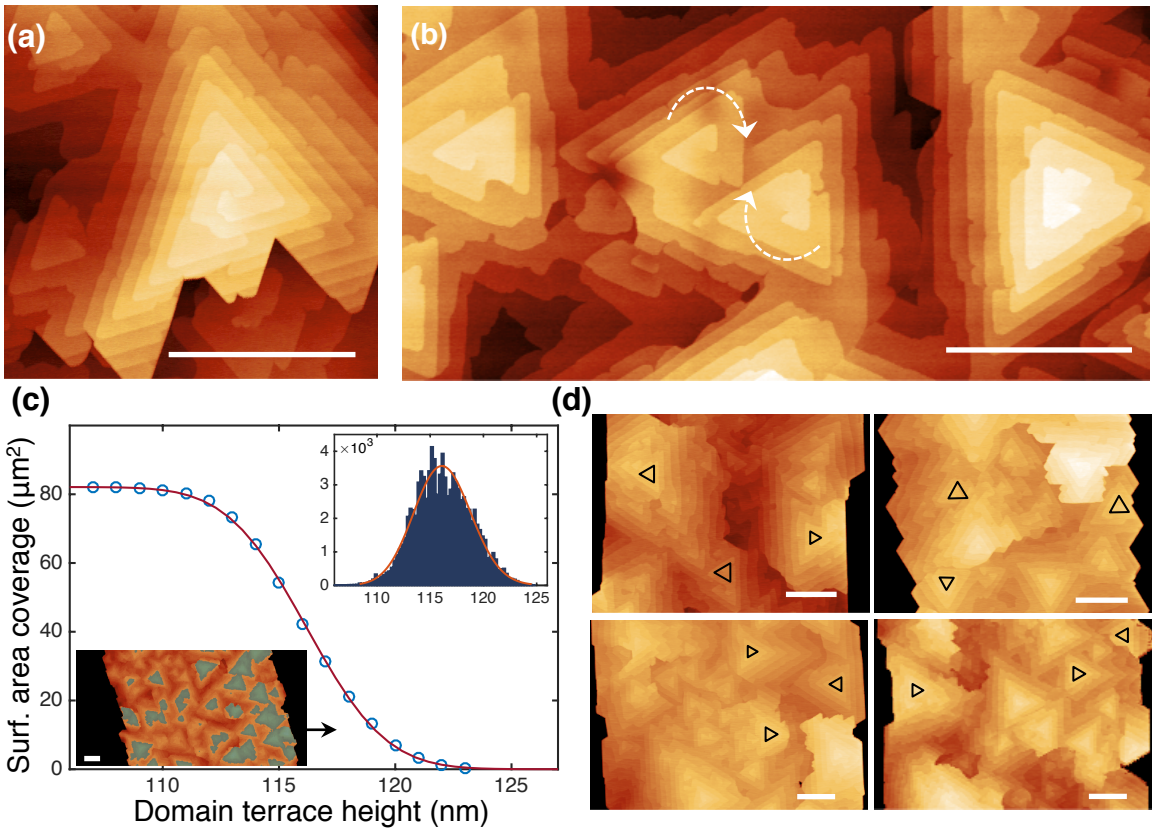

Figure 4.10: (a), (b) Examples of spiral growth of trigonal terraces on a CF-vdWE grown TI. (c) TI annulus surface area coverage as a function of the absolute terrace height of the constituent trigonal domains (open circles), and its lognormal CDF dependence (solid line). Top inset shows the AFM thickness distribution fitted to a lognormal PDF. Bottom inset shows the area coverage at a domain height of 118 nm. (d) AFM images of TI annuli with top-most domains indicated by black triangles. All scalebars are 1μm.[117]

gesting an influence of the hexagonal in-plane symmetry of the underlying (0 0 1) mica surface. The large equilateral trigonal domains observed in the AFM images (*e.g.*, Fig-4.9(b)) reflect the trigonal-hexagonal in-plane symmetry of the tetradymite crystal, analogous to growths involving thin films and/or substrates with hexagonal symmetry.[69,126] Fig-4.9(c) illustrates a typical layered trigonal domain. The step height between each subsequent layer is almost 1 nm, which is the thickness of one quintuple layer of the tetradymite crystal structure (Fig-4.2(a)); thus establishing that the BTS domains grow layer-by-layer in an epitaxial fashion.[38,49] While the

edges of the TI annulus superficially appear serrated compared to the smooth lithographic boundaries in the resist, closer examination reveals highly oriented crystalline edges. AFM height profiles of the same BTS annulus at different locations along its perimeter (Fig-4.9(d)) reveal almost straight, armchair-like or zigzag-like crystalline edges exhibiting exactly 120° angles as shown in Fig-4.9(e). This indicates a strong influence of relative localized orientation of the annulus perimeter with the hexagonal lattice of mica, schematically illustrated in the right column of Fig-4.9(d). Due to the artificial boundary condition, the orientation effect appears to be amplified as compared to TI growth on unpatterned pristine mica, opening up an opportunity to selectively grow thin film features in preferred orientations and with custom crystalline edges on patterned hexagonal lattices such as mica, sapphire, hexagonal BN and pyrolitic graphite.

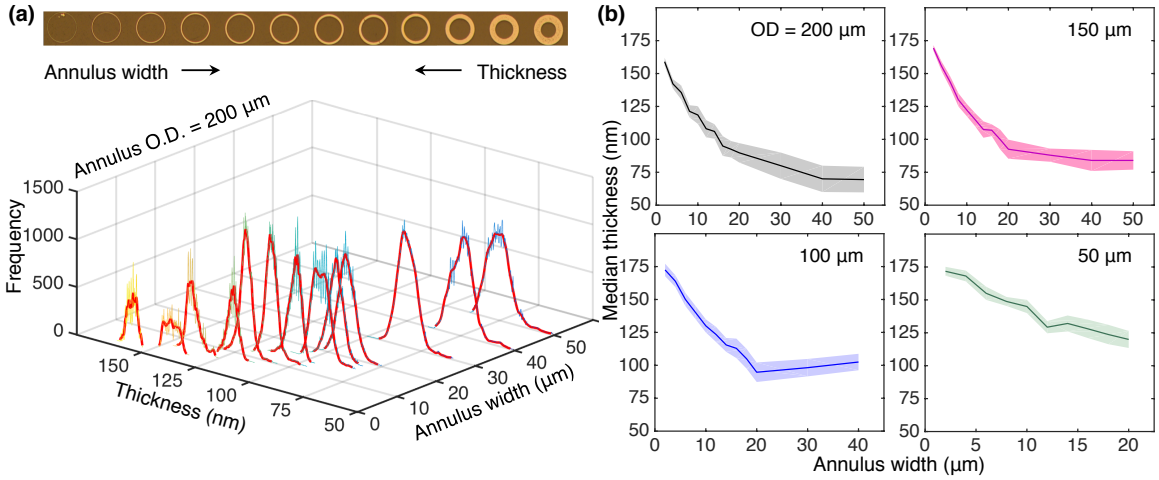

Figure 4.11: (a) AFM thickness distributions for CF-vdWE grown TI annuli of different widths, for an outer diameter (OD) of 200 μm. Solid lines are kernel-smoothed fits to the histograms. (b) Median thickness as a function of the annulus width for different ODs. Shaded regions represent one median absolute deviation.[117]

Interesting features such as cooperative spiral growth on certain trigonal domains are also occasionally observable, as shown in Fig-4.10(a) and (b). Spiral growth of trigonal terraces has been observed previously in vdWE of layered 2D materials,[51] and 3D epitaxial thin films on crystalline substrates.[69] Spiral structures typically arise as a result of screw dislocation centers propagating from the site of nucleation, providing a step source on the surface that leads to winding around the dislocation

center and formation of a spiral.[69] As seen from Fig-4.10(b), the spirals can be clockwise or counter-clockwise and can occasionally also occur as cooperative spirals. Area coverage on the surface of the CF-vdWE grown TI as a function of the absolute height of the constituent trigonal domains is shown in Fig-4.10(c). The bottom inset shows an example of partial coverage at an absolute domain height of 118 nm, highlighted in blue. The coverage data can be accurately fitted with a lognormal complementary cumulative distribution function. Furthermore, the raw histogram data for the AFM measured thickness for the same annulus can also be fitted with a lognormal probability distribution function of the same parameters (top inset in Fig-4.10(c)). This provides further confirmation that the trigonal domains are flat and layered at steps of 1 nm. Fig-4.10(d) shows AFM height profiles of several TI annuli, indicating the topmost trigonal domains with black triangles, the significance of which will be discussed later in Section-5.4.

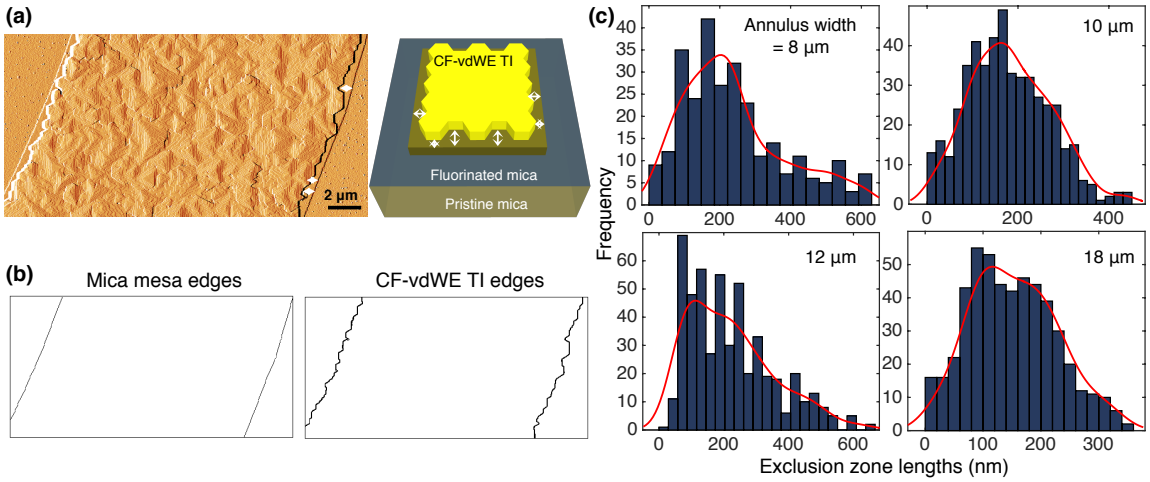

Figure 4.12: (a) AFM amplitude error plot of an 18 μm wide annulus, showing two distinct pairs of edges: the CF-vdWE grown TI crystalline edges and lithographically patterned pristine mica mesa edges (left). Schematic representation of the exclusion zone (right). (b) Both pairs of edges extracted with image detection. (c) Distributions of exclusion zone lengths extracted from image detection for annuli of different widths, from the same growth. Solid lines are kernel-smoothed fits as a visual guide.[117]

Fig-4.11 shows a dependence of CF-vdWE grown TI thickness on the planar feature dimensions, *i.e.*, annulus width. Due to the highly layered growth, the thickness of the CF-vdWE grown TI is distributed. Fig-4.11(a) shows the evolution of

the thickness distributions as a function of the annulus width from a representative growth, for a fixed outer diameter (OD) of 200 μm. As the annulus width increases, the average thickness decreases nonlinearly and shows saturating behavior, while the distributions evolve to become unimodal, exhibiting positive skewness akin to lognormal or log-logistic distributions. Fig-4.11(b) shows median thickness as a function of annulus width for four different OD sets from the same growth. The directly-grown annulus shapes conveniently provide a singular parameter (annulus width) for comparative analysis without having to find an appropriate normalization of planar dimensions of the features to their nearest-neighbor distances or pitches.[108,111] As an unusual characteristic, denuded or exclusion zones (EZ) near the feature boundaries are also observed, more evident in AFM amplitude error images. Fig-4.12(a) shows one such example, where two distinct pairs of boundaries are visible: the crystalline edges of the CF-vdWE grown TI annulus, and another smoother boundary on the outside. The external boundary is the pristine mica mesa formed during the selective-area CF_4 plasma process, typically 2-3 nm in height. Intriguingly, the TI domains in the central region of the patterned annulus grow and merge to form contiguous films, whereas the EZ near the feature boundary remains almost entirely denuded as shown in the schematic in Fig-4.12(a). In order to extract the lengths of the EZs, the two pairs of edges are extracted from the AFM image as shown in Fig-4.12(b) with image detection in MATLAB, and a length distribution of the difference between the two is obtained. Such distributions are shown in Fig-4.12(c) for annuli of different widths, with values centered around 150-200 nm.

The CF-vdWE process is successful in defining large, selective-area growth of custom-patterned TI features on prepatterned muscovite mica substrates. Interesting growth features are observed for the first time for TI SAG, including nonlinear thickness dependence on lateral feature dimensions and observation of exclusion zone boundaries. The next chapter describes a semi-empirical surface migration growth model in order to explain the growth results, and establish a platform to extend the analysis to a larger set of engineered substrate and growth compound combinations.

Chapter 5

Custom-Feature van der Waals Epitaxy: Growth Model and Transport

This chapter presents a semi-empirical two-species surface migration model to explain the CF-vdWE growth results described in the previous chapter. Transport measurements on as-grown TI shapes are also presented.

5.1 Introduction

As discussed in the previous chapter in Section-4.4, the CF-vdWE growth of BTS TI on prepatterned mica substrates leads to unusual observations, chief amongst them being a nonlinear thickness dependence on lateral feature dimensions and observation of exclusion zone (EZ) boundaries. For a qualitative understanding of the underlying growth mechanism leading to the observations, a semi-empirical two-species model is proposed.[117] Two-species epitaxial growth modes are well studied, especially in compound systems such as Bi_2Te_3, GaN/As, HgTe *etc.*, where both species exhibit significantly different kinetic behavior on the surface during deposition and growth.[108,127,128] The custom-feature vdWE growth is largely a physical process; hence the surface migration of adatoms is expected to play a crucial role in the growth kinetics. The solid precursors Bi_2Te_3 and Bi_2S_3 incongruently sublimate to form atomic vapor fluxes, as has been observed in previous experiments.[45,49] Experimental evidence suggests that the heavier atom Bi and the lighter chalcogen Te have very different surface mobilities on mica surfaces.[129,130] Epitaxial growth studies of Bi_2Te_3 and related tetradymites have typically utilized Te-overpressure recipes in order to obtain high crystalline quality thin films,[50] Bi being the rate-limiter, analogous to the case of Ga in GaAs growth. However, there are important differences between the growth mechanism of MBE deposition and the custom-feature vdWE. With an initial assumption of a two-species surface migration dominated growth mechanism,

Results discussed in this chapter were published in ACS Nano. Contributions: Primary author. Developed the CF-vdWE growth model, fabricated devices, carried out the transport measurements, and performed the data analysis. Citation: T. Trivedi, A. Roy, H. C. P. Movva, E. S. Walker, S. R. Bank, D. P. Neikirk, and S. K. Banerjee, "Versatile Large-Area Custom-Feature van der Waals Epitaxy of Topological Insulators," *ACS Nano*, vol. 11, no. 7, pp. 7457–7467, Jul. 2017, Available: `http://dx.doi.org/10.1021/acsnano.7b03894`.

we derive a simple, yet robust semi-empirical model to explain the crucial observations that render the CF-vdWE method markedly different from the case of MBE or MOCVD.

5.2 Motivation for a two-species model

The tetradymite crystal grows in a nonstoichiometric composition in reality,[57] with the S and Te atoms intermixing in the chalcogen layer of the unit cell, as discussed in Section-2.3. The diffusivities Te, S and Se chalcogens in silicon and II–VI compounds is comparable to one another,[131–135] while for heavy elements like Bi it is much lower.[136,137] Thus, the difference in surface mobility between Te–Bi and S–Bi should also be of the same order. Hence, a two-species model would be appropriate considering Bi as species A, and Te/S as species B. In the nominal growth condition without an artificial boundary condition as in the CF-vdWE growth, as long as the incident areal vapor flux remains constant, any two arbitrary regions of different areas should receive the same amount of flux, and hence exhibit the same thickness at the end of the growth. In order to rationalize a thickness increase for narrower annuli, an additional flux j_{in} must be considered, which is dependent on the feature dimensions and can only originate from the surface diffusion of adatoms from the vast fluorinated regions surrounding the pristine mica features. The observation of an EZ near the patterned feature boundaries is also markedly different from conventional SAG experiments, where an increased thickness at abrupt boundaries is typically observed,[111] as is also observed in conventional epitaxy.[122] An imbalance in the rate of change of available adatoms near the boundary region is required for formation of an EZ, such that an impinging adatom near a feature boundary has a finite probability or rate $-J_{\text{out}}$ of escaping into the fluorinated regions without contributing to compound formation. Thus, the rationalizations that build the basis of the two-species model are: species A has a significantly lower surface migration length (SML) than species B on pristine and/or fluorinated mica surfaces, and that a critical imbalance exists between the additional surface diffusion flux j_{in} and the rate of escape $-J_{\text{out}}$ for the formation of the EZ and increased thickness.

5.3 Two-species surface migration model

This section describes the model in detail, with a discussion of the possible growth scenarios and the growth conditions that can reconcile the crucial experimental observations. The derivation based on the growth scenario is also presented, to provide a semi-empirical equation for the average AFM thickness dependence on lateral feature dimensions of the CF-vdWE grown TI annuli. The model also provides a convenient method to estimate certain important growth parameters *ex-situ*, in addition the insights into the growth kinetics.

Cond.→	$N_A \ll N_B$			$N_A \gg N_B$			$N_A \sim N_B$		
Obs.↓	$s_{A,B} \approx 0$	$s_A \approx 0, s_B > s_A$	$s_B \approx 0, s_A > s_B$	$s_{A,B} \approx 0$	$s_A \approx 0, s_B > s_A$	$s_B \approx 0, s_A > s_B$	$s_{A,B} \approx 0$	$s_A \approx 0, s_B > s_A$	$s_B \approx 0, s_A > s_B$
Thickness increase	×	×	✓	×	✓	×	×	✓	×
EZ formation	✓	✓	×	✓	×	?	?	✓	?

Table 5.1: Logical table outlining growth scenario possibilities for the two-species surface migration model.[117]

5.3.1 Two-species growth scenarios

There are a total of nine possible cases for the growth conditions: three possible scenarios of the amount of constituent adatoms available for compound formation on the patterned mica surface, and three different scenarios of the sticking probabilities for species A and B on the fluorinated mica regions. These scenarios are outlined in the logical Table-5.1, along with the projected outcome of each scenario as pertaining to the two crucial experimental observations. A satisfactory scenario that reconciles both crucial experimental observations can be arrived at by method of elimination.

As outlined in the Table-5.1, there are three possible scenarios of the amount of constituent adatoms available for compound formation on the patterned mica surface, and three different scenarios of the sticking probabilities for species A and B on fluorinated mica. As an example, consider the scenario where the effective available flux or number of adatoms on the patterned mica mesa has a large imbalance such that $N_A \ll N_B$, which is the typical situation in the case of MBE growth of Bi_2Te_3. There are three further possibilities: (1) either both species have zero stick-

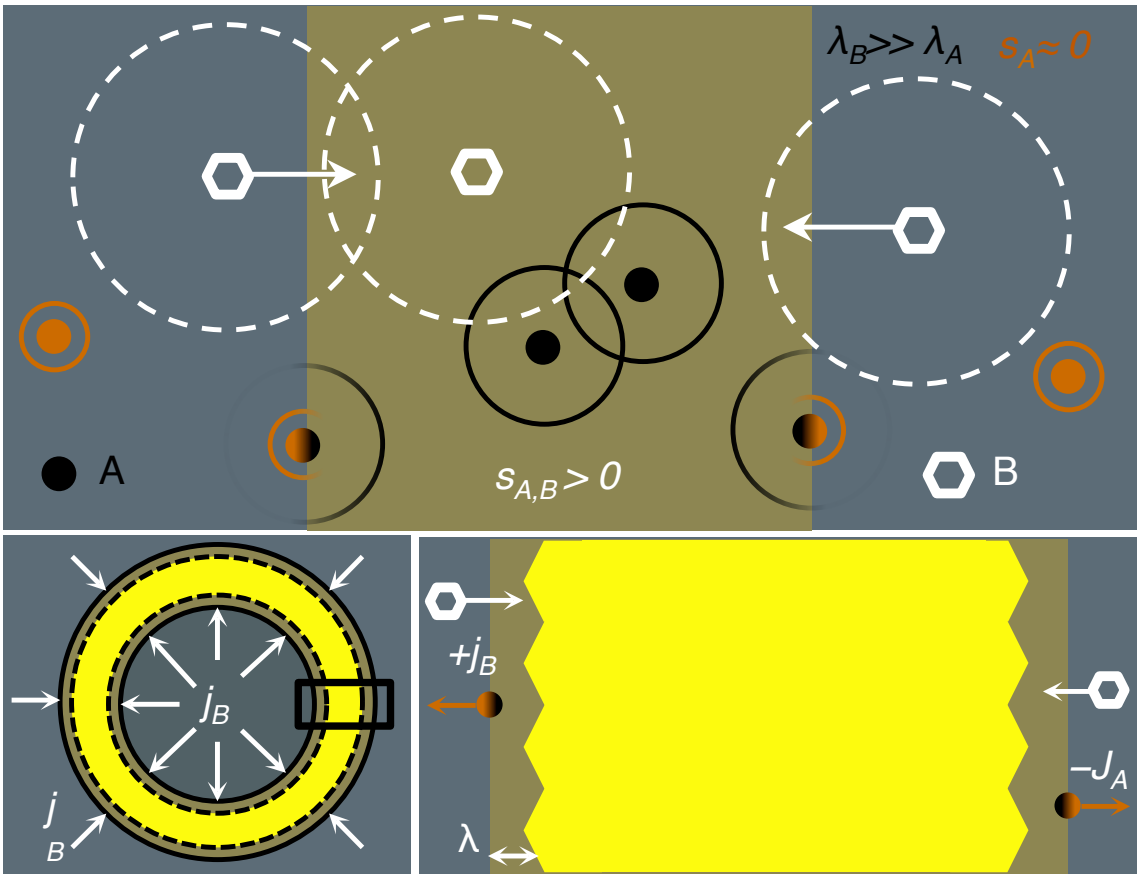

Figure 5.1: Top schematic represents the two-species mechanism for CF-vdWE growth (not to scale). Species A and B have different sticking probabilities, and SMLs as illustrated by different circles. Bottom-left schematic shows an annulus during growth: dashed yellow annulus is the TI with a finite exclusion zone (EZ) near the feature boundary. Bottom-right schematic shows a magnified view of the black box, denoting additional perimeter flux $+j_B$ and escape area flux $-J_A$.[117]

ing ($s_A, s_B \approx 0$), or (2) A has zero sticking probability on fluorinated mica, while for B it is finite ($s_A \approx 0, s_B > s_A$), or (3) vice versa ($s_B \approx 0, s_A > s_B$). For the first condition, an EZ can form near the feature boundaries, if the escape rate of A is faster compared to the rate of additional influx of B over an average distance of the order of λ_A (SML of species A) from the boundary, leading to a critical imbalance of N_A in N_{AB} to significantly reduce compound formation near the boundary. However, a nonlinear thickness increase is not possible, as there cannot be an extra influx of atoms diffusing in from the fluorinated surfaces. For the second (third) condition,

the additional flux Δj_{in} consists of extra B (A) adatoms diffusing inwards from the fluorinated regions, and $-\Delta j_{\text{out}}$ consists of A (B) adatoms near the feature boundary escaping into the fluorinated regions to almost instantly desorb. In the second condition ($s_A \approx 0, s_B > s_A$), an EZ is possible at the boundary, similar to the first condition. An EZ cannot form for the third condition ($s_B \approx 0, s_A > s_B$) however, where species A diffuses inwards from the fluorinated regions. The additional incoming A adatoms can form a compound near the boundary irrespective of a rate imbalance, as the overall concentration of species B is significantly higher than A. On the other hand, a thickness increase is not possible in the second condition, as a reduction in effective N_A leads to a direct reduction in total moles of compound molecules N_{AB}, notwithstanding additional B adatoms. Nevertheless, both the thickness increase and EZ formation cannot occur such that neither of the scenarios represented by the three conditions can completely describe the underlying growth mechanism behind the experimental observations. Similar arguments can be extended for the other cases enumerated in the table, until a satisfactory condition is found through the method of elimination. Such a condition requires the concentration of species A and B to be of the same order, and $s_A \approx 0, s_B > s_A$ on fluorinated mica. The two-species surface migration model is schematically represented in Fig-5.1.

5.3.2 Derivation of the model

Consider the area of incident areal vapor flux, directly contributing to the growth (explicitly omitting the exclusion zone (EZ) boundaries):

$$\begin{aligned} A^{\text{in}} &= \pi\left(R^2 - r^2\right) - \pi\left(R^2 - (R-\lambda)^2\right) - \pi\left((r+\lambda)^2 - r^2\right) \\ &= \pi\left(R^2 - r^2\right) - 2\pi\lambda\left(R + r\right) \\ &= \pi\left(R + r\right)\left(\omega - 2\lambda\right) \end{aligned} \tag{5.1}$$

R and r in Eq-5.1 are the outer and inner diameter of the annulus, respectively, and $\omega = R - r$, which is the annulus width. λ represents an average value of the EZ size. The evolution of the two species A and B can be expressed as follows, where

the superscripts i and f denote initial and final quantities, respectively:

$$\begin{aligned} &2\ A + 3\ B \rightarrow 1\ A_2B_3 \\ &N_A^f = N_A^i - \Delta N_A,\ N_B^f = N_B^i + \Delta N_B \\ &N_{AB}^f = N_{AB}^i + \Delta N_{AB},\ \text{iff}\ \Delta N_A < {}^3\!/_2 \Delta N_B \end{aligned} \tag{5.2}$$

Eq-5.2 describes the condition in which a thickness increase may be possible as long as the inequality is satisfied. This condition is also conducive to formation of an EZ, as long as there is a steady outflux of A in an average radius of the order λ_A near the feature boundary, leading to a local reduction in ΔN_{AB}. The additional change in the moles or number of atoms (ΔN_{AB}) of the compound can only be positive if the final inequality in Eq-5.2 can be satisfied. The individual species changes can be expressed in terms of a rate of change of the species normalized to spatial dimensions, *i.e.*, a flux-like quantity. As illustrated in the schematic of Fig-5.1, the additional surface influx of species B, $+j_B$, can be considered as a "perimeter flux" that enters from the both the inner and outer perimeters of the annulus under consideration, and hence depends on the geometry of the annulus. The escape flux of species A localized near the EZ can be represented as a fraction $f \cdot \eta_A$ of the total incident areal vapor flux of species A, or $-f \cdot \eta_A J_A$. η_A is the ratio of the area of the EZ[†] to the total patterned annulus area. The area ratio η_A provides the number of species A adatoms that fall just in the EZ near the boundary, and a further fraction f of that number may escape to the fluorinated regions. Then the change in the species concetration in Eq-5.2 can be written in terms of the additional fluxes as:

$$\begin{aligned} \Delta N_{AB} &= 2\Delta N_A + 3\Delta N_B \\ &= (3 j_B \tau) \cdot 2\pi\,(R + r) - (2 f \eta_A J_A \tau) \cdot 2\pi\lambda\,(R + r) \end{aligned} \tag{5.3}$$

In Eq-5.3, τ is the growth duration, j_B and J_A are the species B additional perimeter flux and species A escape area flux, respectively, and η_A represents the fraction of the species A in the EZ area that escape to the fluorinated regions. The

[†]The area of the EZ is the vanishingly narrow annuli formed between the CF-vdWE TI crystalline edges and the patterned annulus boundary represented in Fig-5.1 as the area between the yellow TI and brown mica annuli, which is the second term in the second line of Eq-5.1

total number of available adatoms for growth can be expressed as:

$$\begin{aligned} N_{AB}^{f} &= N_{AB}^{i} + \Delta N_{AB} \\ \frac{N_{AB}^{f}}{\rho_N} &= \frac{N_{AB}^{i}}{\rho_N} + \frac{\Delta N_{AB}}{\rho_N} \Leftrightarrow V_{AB}^{f} = V_{AB}^{i} + \frac{\Delta N_{AB}}{\rho_N} \\ d_{\text{tot}} \cdot A^{\text{in}} &= d_0 \cdot A^{\text{in}} + \frac{\Delta N_{AB}}{\rho_N} \end{aligned} \tag{5.4}$$

In Eq-5.4, ρ_N is the number density of the BTS compound and $V_{f,i}$ are the volume of the feature in the final and initial conditions, respectively. The total thickness of the feature is d_{tot}, the nominal thickness considering only an incident areal vapor flux is d_0 and A^{in} is the active area directly contributing to the growth, from Eq-5.1. Eq-5.4 can be rewritten, substituting from Eqs.-5.1 and 5.3:

$$\begin{aligned} d_{\text{tot}} &= d_0 + \frac{1}{A^{\text{in}}} \cdot \frac{\Delta N_{AB}}{\rho_N} \\ &= d_0 + \frac{2\pi\,(R+r)}{\pi\,(R+r)\,(\omega - 2\lambda)} \cdot \left[3\frac{j_B \tau}{\rho_N} - 2\lambda\eta_A \frac{f J_A \tau}{\rho_N} \right] \\ d_{\text{tot}} &= d_0 + \frac{\tau}{\rho_N} \cdot \frac{6 j_B \omega - 8 f \cdot J_A \lambda^2}{\omega^2 - 2\lambda\omega} \end{aligned} \tag{5.5}$$

5.4 Fits to the two-species surface migration model

From the discussion and the derivation in the last section, Eq-5.5 provides a convenient semi-empirical model for determining the thickness dependence of the CF-vdWE grown TI annuli on their lateral dimensions, *i.e.*, annulus width ω. To recap, the other parameters in Eq-5.5 are: the total thickness d_{tot}, a mean exclusion zone length λ, additional incoming perimeter flux and fractional escape areal flux for species B and A, j_B and $f \cdot J_A$, respectively, growth time τ and tetradymite number density ρ_N. The model provides an excellent fit to the thickness dependence data as shown in Fig-5.2, and the extracted growth parameters from the model fits are shown in Fig-5.3.

The fit yields all four unknowns: a nominal thickness d_0, species B influx j_B, species A escape flux $f \cdot J_A$, and an empirical EZ length λ. Note that there is

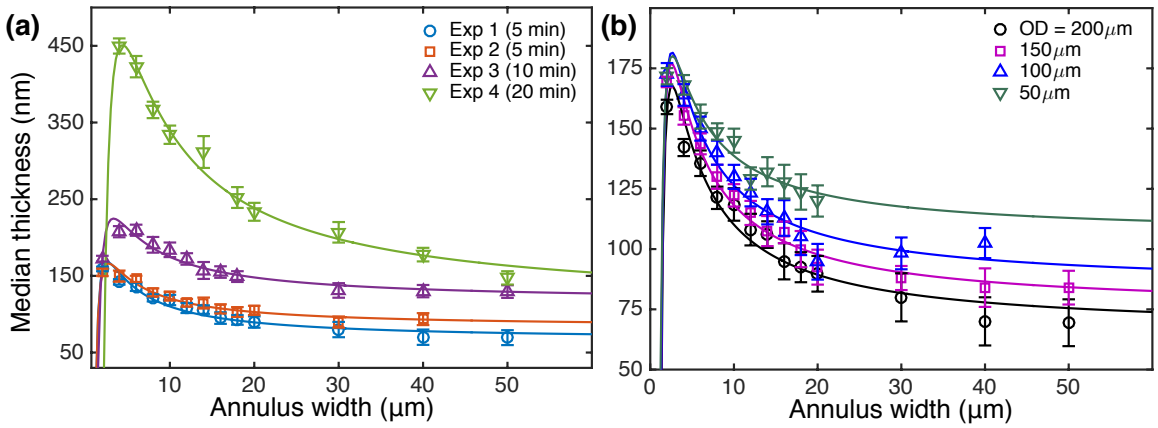

Figure 5.2: AFM measured median thickness of CF-vdWE grown TI annuli as a function of the width from (a) different growth runs (Exp 1 Ð 4) and (b) different ODs from Exp 1. Solid lines are fits to the two-species model of Eq-5.5.[117]

no empirical mechanism to estimate the fraction f itself from the areal escape flux; hence the value of the actual incident species A areal flux is unknown. Nonetheless, the crucial quantity in the model is the fractional escape flux itself and its critical imbalance condition with j_B according to Eq-5.3. The extracted values of the fluxes remain virtually unchanged with growth durations or annulus OD for a given growth duration as shown in Fig-5.3, indicating that the same critical rate imbalance plays a role across different growth experiments and regardless of feature dimensions. The extracted λ from the fits also exhibit little variation as shown in Fig-5.3(b), and are of the same order as experimentally observed EZ lengths from AFM images from Fig-4.12(c), further corroborating the validity of the two-species model. Incidentally, both the observed and extracted EZ lengths are of the same order as the size of the topmost trigonal domains, marked as black equilateral triangles in Fig-4.10(c). The average size of these domains is indicative of the average diffusion length or SML of the least mobile of the two adatoms, *i.e.* species A, on an epitaxial BTS surface. During lateral growth of a trigonal domain, adatoms diffuse to find the lowest energy location along its edges. For higher deposition rates, as the domain size increases, the least mobile adatoms cannot reach a domain edge quickly enough; thus formation of a new domain on the surface of the parent becomes energetically favorable.[138] While the SML of species A on pristine mica and the BTS surface itself should nominally be different, there seems to be a fair agreement between the values, thus providing a

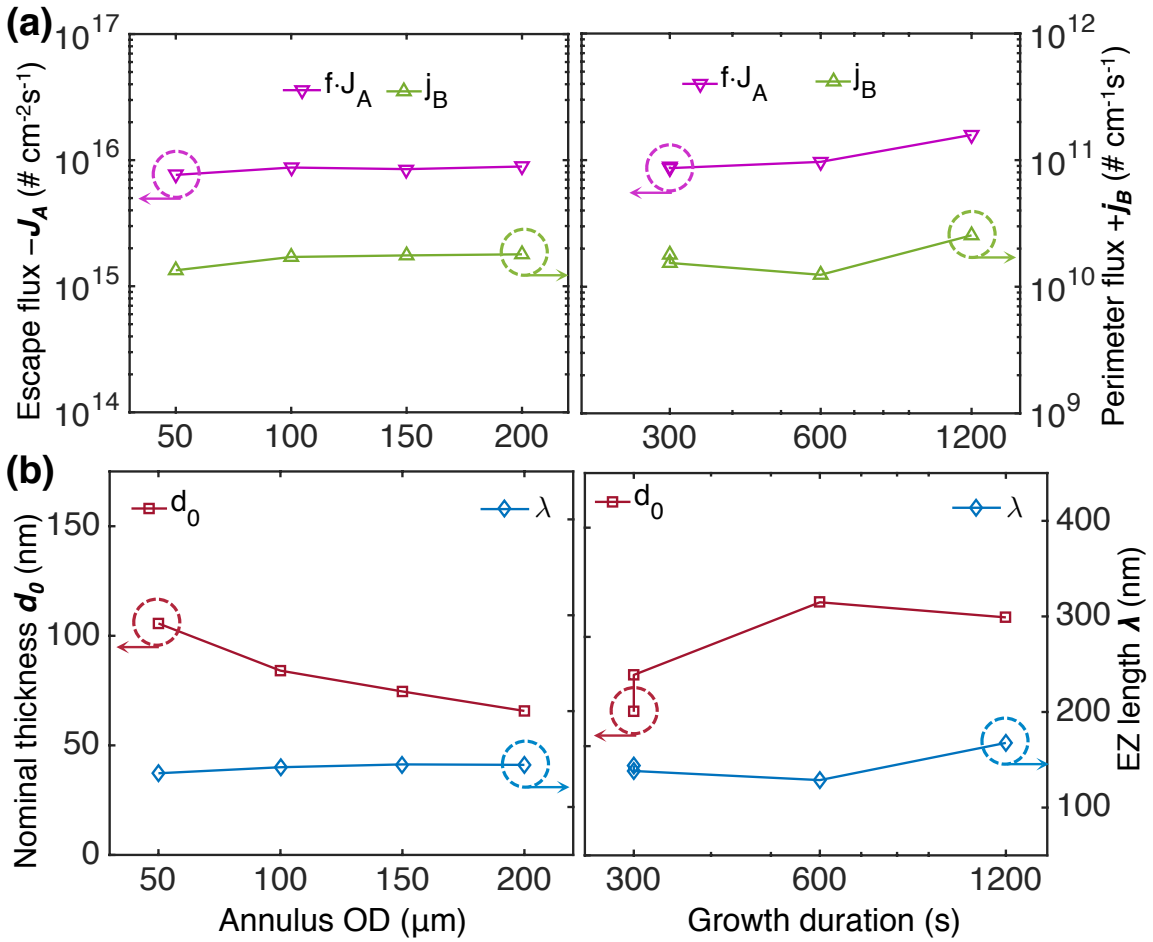

Figure 5.3: (a) Extracted fractional escape flux $-f \cdot J_A$ and additional perimeter flux $+j_B$, (b) Extracted nominal thickness d_0 and EZ length λ, as a function of annulus OD for Exp 1, and growth durations for Exp 1 Ð 4.[117]

convenient empirical mechanism to estimate a mean SML for species A.

Thus, the two-species model yields a simple and logical picture of the underlying growth kinetics due to the selective-area fluorination, without the need to numerically solve the diffusion equation, while still providing excellent empirical estimates of important growth parameters. The matrix of directly-grown annuli allows for a convenient *ex situ* mechanism for exploring growth kinetics and topographic dependence of 2D materials SAG processes in general. Different species have different surface sticking and migration behavior on fluorinated and pristine mica, which leads to selective-area growth well-confined within the feature boundaries. There is a

critical flux imbalance condition that is pivotal for observing nonlinear thickness dependence and EZ formation. Further control on the thickness of the CF-vdWE grown TI can be achieved through controllably regulating the multispecies adatom flux on the fluorinated surface by changing the amount of solid precursor or the volumetric precursor flux.[120] Such a growth condition may be optimized to vary thickness across a single substrate for specialized applications, such as variable thickness grating for on-chip plasmonics and optoelectronics. Conversely, pre-patterning features of the same lateral dimensions may yield a more uniform thickness across the substrate, such that scalable TI devices can be directly grown and fabricated for applications such as spin-transfer torque memory arrays. With careful consideration of the interplay between the compound species and modified surfaces through such multi-species modeling, the CF-vdWE method can be extended to grow several different van der Waals (vdW) compounds on specifically selective-area engineered substrates.

5.5 DC transport measurements on CF-vdWE grown BTS

In order to determine the quality of the TI material for electronic applications, DC transport measurements on devices of CF-vdWE grown TI Hall bars were performed, as shown in Fig-5.4. Due to the ease of incorporation of photolithography masks with different features into the CF-vdWE method, an array of Hall bars of variable dimensions (hence variable thicknesses) can be grown directly, and a subsequent mask can be aligned to define metallic contact leads as shown in Fig-5.4(a) and inset of Fig-5.4(b). Fig-5.4(b) shows the sheet resistance of two different devices as a function of the substrate temperature, measured down to 77K in a liquid-N_2 probe station. Both show monotonic decrease in resistance with temperature, which is expected of the metallic nature of TSS-dominated transport in planar devices. A reduction in the rate of decrease of resistance is observed as the temperature is decreased, which can lead to an insulating ground state at even lower temperatures, after a resistance minimum is encountered as discussed in Section-3.4. Fig-5.4(c) shows the room-temperature device sheet conductance in units of e^2/h as a function of the Hall bar thickness across three difference growths, exhibiting remarkably flat behavior expected from a metallic TSS-dominated transport mechanism. A two parallel channel conduction model for TI devices can be considered, as described by

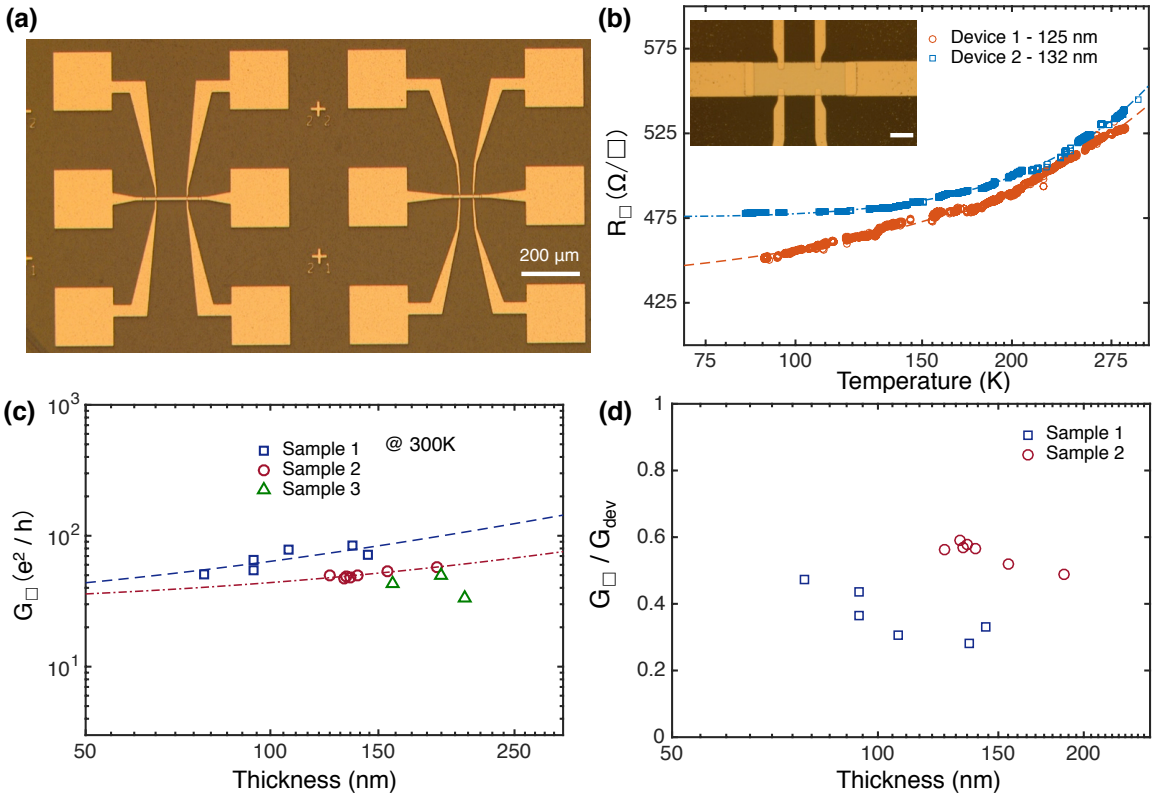

Figure 5.4: (a) Optical image of fully fabricated representative devices on CF-vdWE grown TI Hall bars. (b) Sheet resistance of two candidate TI Hall bars as a function of sample temperature, showing a monotonic decrease in resistance, and early indications of insulating ground state. Inset shows a typical Hall bar (scale bar is 20μm) (c) Sheet conductance of several different Hall bars from three different growths at room temperature, exhibiting very low bulk conductivities. Dashed lines are fits to Eq-5.6. (d) Ratio of the TSS conductance to the total device sheet conductance at room-temperature as a function of device thickness, calculated from Eq-5.6.[117]

Eq-3.3 in Section-3.4, in terms of the measured 4-point device conductance:

$$G_{\text{dev}} = \sigma_b \cdot d + G_{\square}^{\text{ss}} \tag{5.6}$$

In Eq-5.6, G_{dev}, σ_b and $G_{\square}^{\text{ss}}$ are the total device sheet conductance, bulk conductivity and surface state conductance, respectively and d is the TI thickness. This model considers an effective TSS conduction channel $G_{\square}^{\text{ss}}$, while other parasitic contributions such as bulk conduction due to native defects and chalcogen deficiency

doping, and elastic scattering between the bulk and TSS channels, can be lumped into an effective contribution σ_b (different parallel channel contributions are discussed in detail in Sections 3.6 and 3.7.

The linear fit of Equation 2 is applied to the experimentally measured Gdev for Sample 1 and 2, to extract the σ_b values of 150 S/cm and 61 S/cm, respectively, signifying very low bulk conduction that is comparable to bulk-insulating exfoliated BSTS devices,[40] likely due to lower bulk defects and chalcogen deficiencies. The fits also yield the y-axis intercept for Sample 1 and 2, *i.e.* $G_{\square}^{ss}$, as 23.7 and 28 in units of e^2/h, respectively, indicating similar 2D TSS metallic conductivity and uniformity across devices from separate growths. For the devices of Sample 1 and 2, the contribution of the 2D Dirac TSS to total conduction at room-temperature is scattered around 50% (Fig-5.4(d)) with the largest one being at 60%, which is amongst one of the highest reported room-temperature conduction ratios in synthesized TI thin films, rivaling that of bulk crystal exfoliated devices of BSTS.[105,139] Excellent transport and optical properties of TSS for devices of comparable thicknesses have been previously reported for epitaxial thin films and bulk crystal exfoliated flakes for high quality crystalline TIs.[21,24,35,36,140] At lower operating device temperatures, imperative for several TI applications involving proximity-effect heterostructures with superconductors and ferromagnets, the TSS contribution is expected to increase as the bulk carriers are frozen out, further improving the device characteristics. Moreover, due to the highly crystalline and insulating mica bottom interface, substrate related scattering limiting TSS mobility is expected to be negligible.[103] The DC transport measurements establish a TSS-dominated conduction mechanism in the directly-grown TI devices, with a promisingly low bulk contribution and an intrinsic chemical potential at room-temperature. The high quality CF-vdWE grown TI shows great potential for implementing practical devices on large-area crystalline arrays, for applications such as in spin-transfer torque memory,[20] spin based logic[21] and on-chip plasmonic devices.[24]

Chapter 6

Conclusions and outlook

6.1 Conclusions

The research work summarized in this dissertation has endeavored to provide realistic solutions to the challenges of practical implementations of topological insulator (TI) based devices. The approach was to divide the problem and address it from two fronts: to obtain high-quality, reliable TI material and to fabricate devices for in-depth magnetotransport analysis of the underlying device physics. The ternary TI compound $Bi_2Te_{2-x}S_{1+x}$ (BTS) was chosen as the candidate material for the research, in part due to its theoretical potential as one of the best 3DTI compounds.

First-time van der Waals epitaxial (vdWE) growth of BTS nanosheets on SiO_2, hexagonal Boron Nitride (hBN) and muscovite mica was demonstrated. As grown BTS material is obtained in highly layered, good-quality crystalline nanosheets. Detailed transport experiments in devices of BTS indicate the presence of surface states, albeit with bulk states still present in the transport. Weak anti-localization (WAL) and universal conductance fluctuation (UCF) signatures are seen in the magnetoresistance of the BTS devices. Evidence of a combination of both weak antilocalization and electron-electron interaction (EEI) effects is seen from analyzing the insulating ground state in the temperature and field-dependent conductivity data. An extended-HLN model is considered, which provides excellent fitting to longitudinal magnetoconductance data in high-field range, and indicates the presence of 2D surface states, partially coupled to the bulk conducting states. Two-channel Hall conductivity model in conjunction with the extended-HLN model provides a good fit for the magnetoconductance data. The HLN effective prefactor α_{eff} provides a good qualitative tool to understand the regimes of transport in the device, and its value is indicative of the contribution of different channels acting in parallel. The temperature dependent phase coherence lengths from UCF data are in good agreement with those from WAL data, showing 2D behavior arising from topological surface states. The magnetoconductivity data and its empirical modeling show that the bulk conduction channels are still present in the BTS material, likely due to high level of n-type doping by chalcogen deficiency. Electrostatic gating on dual-gated BTS devices indicate separation of

channels when the density in the device is tuned, leading to sharper WAL signatures and larger UCF fluctuations, in agreement with the extended-HLN correction analysis. A three-channel Hall conductivity model is proposed and is shown to provide a more satisfactory fit to gated Hall conductance data, further bolstering the separation of channels argument. Our studies confirm BTS as a candidate 3D TI material in conjunction with the previous APRES measurements, and takes a step closer to understanding transport mechanism in TI materials. Future growth experiments of the BTS material on highly crystalline substrates and substitutional doping with more p-type elements such as Sb, are expected to improve the electronic properties of the BTS material system by reducing the chalcogen deficiency doping and pushing the Fermi level further into the bandgap, leading to the predicted promising nature of the Sulfur based ternary tetradymite. Additionally, more experiments with top and bottom gating on high-quality BTS material are also expected to reveal further the nature and contribution of the multiple transport channels acting in parallel in 3D TIs.

A scalable and high-yield custom-feature vdWE (CF-vdWE) process using selective-area surface modification through microlithographically masked fluorination is also demonstrated for the first-time for realizing large-area crystalline growth of TI compounds on mica. Large terraced single-crystal trigonal domains several microns in size are observed, which merge to form contiguous thin films. The features exhibit a highly oriented growth with the underlying hexagonal mica lattice exhibiting location-dependent zigzag or armchair edges, uncovering the prospect of growing TI and 2D materials in preferential orientations on specifically engineered vdW substrates. The thickness of the CF-vdWE grown TI has a nonlinear dependence on the planar feature dimensions, which can be described well by a semi-empirical model considering two-species surface migration on the mica surface. Depending on the application, the TI thickness can be tuned across a sample by varying feature dimensions or be kept constant for an array of similarly sized devices. Transport measurements on CF-vdWE grown TI Hall bars reveal TSS-dominant conduction with low bulk conductivity, indicating excellent electronic material quality for on-chip applications of TI. The CF-vdWE method can be readily extended to wafer-scale large area crystalline TI growths. The vdWE method additionally provides a facile way to exchange source precursors with minimal alteration to introduce dopants or different compound

combinations, to grow a plethora of layered 3DTI compounds from the tetradymite family, i.e., $(Bi_{1-y}Sb_y)_2(Te_{1-x}[Se/S]_x)_3$. In principle, this method also presents a promising candidate for exploring custom-feature large-area growth of other technologically relevant 2D van der Waals materials such as transition metal and column III/IV chalcogenides for next-generation electronics and photonics applications. The CF-vdWE process achieves a versatile growth method harnessing planar microfabrication processes to obtain large-area crystalline TI structures for electronic, spintronic and on-chip optical device applications, while simultaneously being highly adaptable to prototype research as well as optimized scalable implementation.

6.2 Outlook

Utilizing the research presented in this dissertation as a platform, there are several directions worth pursuing for future projects in the field of TIs and 2D materials. Some of them are outlined below:

1. Optimize the vdWE growth of BTS on hBN substrates (exfoliated and CVD-grown) and fabrication of hBN-encapsulated BTS devices for further exploring underlying transport physics in TIs.

2. Extend the vdWE growth method to incorporate antimony (Sb) into the mix to synthesize $(Bi_{1-y}Sb_y)_2(Te_{1-x}S_x)_3$ compound on different substrates, and to tune the intrinsic doping to control the parasitic conductivity.

3. Extend the CF-vdWE growth method to explore growth on selectively engineered highly crystalline substrates such as quartz, sapphire and hBN. The two-species surface migration model is a helpful guide in understanding the role of selective-area fluorination. This analysis may be extended to other substrates with specific schemes of selectively engineered surface free energies, and overlayer compounds with inherently different surface migration behavior on the engineered substrate. The location-dependent edge orientation observed in CF-vdWE of TI on mica also prompts investigation into growing preferentially oriented thin film heterostructures of vdW compounds.

4. Explore CF-vdWE grown TI on insulating substrates (such as mica) for on-chip coplanar device applications at RF and microwave frequencies. The process pro-

vides excellent control on feature sizes and shapes, which are crucial for coplanar waveguide and device designs. TIs have been recently shown to have potential for microwave applications due to some inherently nonlinear and nonreciprocal properties of the material system.

5. Extend the CF-vdWE method to synthesize other layered vdW compounds such as In_2Se_3, GaSe, transition metal dichalcogenides MX_2, where M = [Mo, W] and X = [S, Se, Te].

6. Extend the CF-vdWE process to wafer-scale and optimize its scalable manufacturing for immediate applications in flexible electronics.

It is hoped that the CF-vdWE growth, characterization and in-depth transport analysis presented in this work will provide a solid foundation for researchers in the field of TI and vdW materials at large, with easy incorporation of growth compounds and substrate combinations for rapid prototyping, and exploration of the DC and AC transport in TI materials for future device applications.

Appendices

Appendix A

vdWE Operating Procedure and Maintenance

This appendix describes the standard operating procedure (SOP) for the in-house van der Waals epitaxy (vdWE) growth system in detail. The vdWE schematic and photograph are shown in Fig-2.1 in Chapter 5. The system is currently setup inside the MRC clean rooms, in the thermal service aisle behind the MRL furnaces. The vdWE system is owned and operated by Prof. Banerjee and Prof. Tutuc's research groups. Any modifications to the system or additions to its growth capabilities (*e.g.*,including new materials) must be first confirmed with both the professors, then the MRC safety coordinator and the facilities manager. Banerjee and Tutuc students will always have the first priority on the system, and only regular growers may manage the equipment usage calendar.

A.1 vdWE system components

The vdWE growth system is composed of the following components:

1. Furnace (ThermoFisher):
   (a) Lindberg/Blue M 1200°C split-hinge tube furnace with three controllable zones (part#: HTF55347C)
   (b) 3-zone programmable controller with programmable center zone. Outside zones can be set at a $\pm\Delta T$ from the central zone temperature. (part#: CC58434PC-1)
   (c) Furnace tube adaptor: 3" to 60mm (2.36"). Other sizes of adaptors should be bought directly from ThermoFisher.
2. Quartzware (MTI Corp): 400mm long quartz tube with 60 mm outer diameter (OD) and 55 mm inner diameter (ID) (part#: EQ-QZTube-60GE-1400). Quartz boats (part#: EQ-QB-1017) are used for holding precursor powders and slotted 1" wafer diffusion boats (part#: EQ-QB-1025) are used for holding samples during growth. Source and sample quartz boats are held in larger quartz carriers with extended legs, for easy access via quartz furnace rods. The carriers are custom made by the UT Chemistry glass shop.
3. Vacuum and gas manifold (custom-designed with KF-25 or 1/4" lines, standard O-ring seals and Swagelok joints):
   (a) Vacuum flanges (MTI Corp part#: EQ-FL-60KF25-FT) with KF-25 fitting on the pump side and Swagelok fitting on the input side. High-

temperature Silicone O-rings must be used to seal the flange (MTI Corp part#: EQ-SOR-60).

(b) Gas input manifold is custom designed currently with three 1/4" input lines. An N_2 purge line with a direct valve, and two mass flow controllers (MFC): one N_2 and the other is Ar gas. Note: the MFC on the Ar gas line is NOT calibrated for Ar, but for H_2. Future additions to the gas input manifold should include two on-off Swagelok valves (e.g., part#: SS-4P4T-BK) for every line, including retrofitting current lines, installed upstream and downstream of the MFC.

(c) A 4 channel MFC controller, used manually. Contact MRC facilities staff for servicing or replacing the controller.

(d) Pump-side manifold is also custom designed with KF-25 bellows and has the following components:

- Main line is a KF-25 line with the main valve assembly: an in-line manual bellows valve (Ideal Vacuum part#: P103845) and a manual butterfly valve (generic).
- A bypass line is a 1/4" line comprising of a metering valve (Swagelok part#: SS-SS4-VH) with two quarter-turn on/off valves (Swagelok part#: SS-4P4T-BK) up and downstream of the metering valve.
- A KF-25 Pirani vacuum gauge tube (KJL part#: KJL275196) with a benchtop gauge monitor (KJL part#: KJLC 375).

4. Roughing pump. Current pump, as of August 2017, is an Edwards hydrocarbon oil pump that was installed in summer 2016. Any standard mechanical pump can be used. Installation of a turbo pump requires major modifications to the vacuum manifold, and conflat flanges. Changing the tube often will no longer be possible.

5. Negative pressure acrylic hood over the tube mouth on the pump-side. The baffle on the exhaust must **always** be open unless advised otherwise by the MRC facilities staff.

A.2 Pre-growth preparation

This section describes the standard pre-preparation steps for the vdWE growth system that should be followed before a spell of growths, including preparing the quartzware and calibrating the furnace.

A.2.1 Preparing quartzware

When a new quartz tube is installed or new quartz ware is used for the first time, a controlled bakeout step is recommended to remove contaminants and prepare the quartz ware for subsequent growths.

- New tubes should be removed from all external packaging except the internal tube holder, and taken to the thermal isle. There it should be unwrapped completely while wearing standard clean room garb.

- Tube should be loaded in the tube cleaning acid hood for a rinse in extremely dilute HF for several hours. Training on this hood is mandatory, and notifying MRC staff prior to using this hood is recommended. This hood is used to clean the high-yield MRL furnaces, so must be kept free of contamination at all times. Note: DO NOT LOAD any tubes in there contaminated with heavy metals (such as Bi, Sb, Mo, W). Once a tube has been used for growth it should NOT be cleaned in this station.

- Put on standard acid hood aprons, gloves and face shield. Then load the tube gently in the tube holder bath in the hood. Fill the bath with DI water and drain it at least five times. Fill the bath until the tube is well submerged for the overnight rinse.[†]

- Get a bottle of standard 49% HF (not BHF) and pour roughly a quarter of it in the filled bath slowly and steadily.[‡] Remember to have your acid hood garb and especially the face shield on at this time. Lower the acid hood sash and leave a note with your name and phone number on it.

- Let the tube clean for a good 3 – 6 hours. Then repeat a drain/refill cycle for at least 10 times.

- Put on acid garb and gently remove the tube. Dry it on the outside with several cloth wipes. It is crucial to clean it with soft cloth wipes ONLY, to prevent scratching. Dry the inside of the tube with the custom-rigged "lollipop" shaped rod covered with several cloth wipes. Only basic drying is required at this stage, there is no need to be thorough. Leave the tube overnight in the quartz holder cabinets in front of the vdWE furnace.

Quartzware such as source and sample boats, their carriers *etc.* should also be cleaned if they are used for the first time. They should also periodically be cleaned as there will be plenty of deposition on them during each growth. A good rule of thumb

[†]The bath has a very slow drain, so be sure to fill it up with plenty of water.

[‡]DO NOT pour a lot of HF in there, as it can lead to fast etching and crack propagation in the tube.

is to clean them every 10 growths and/or every time a tube is changed. Quartzware cleaning steps are as follows:

- Log in to acid hood H-14 and prepare a standard 30%H_2O_2 and H_2SO_4 (1:2) piranha solution in the quartz container. It is assumed that the user is trained on acid hoods.
- After 5 minutes when the piranha solution is bubbling, gently lower the quartzware in the bath such that it is vertical and some part of it is safely accessible above the bath. It is recommended to use teflon baskets to easily lower and raise the quartzware. One or two boats at a time should be cleaned for safety and handling purposes.
- After a minute of cleaning, the boats can be flipped to clean their other half using teflon tweezers. DO NOT use metal tweezers as they may scratch/break and contaminate the boats.
- Once the boats are cleaned on both sides, load the teflon basket containing the boats into the DI water bath and do a 10-cycle rinse.
- Repeat the procedure until all quartzware has been cleaned and rinsed. Wipe the boats with cloth wipes and store them in the furnace storage cupboard overnight.

Once the quartz tubes and boats have been cleaned and dried overnight, they may be installed in the furnace for a bakeout step:

- Load the quartz tube into the furnace. It is advisable to get help from a colleague for safety and handling. Once the tube has been safely loaded, fasten the gas input manifold side vacuum flanges on the tube with the O-rings.
- Load the cleaned quartzware such as boats and carriers into the central zone of the tube, then fasten the pump-side vacuum flanges on the tube and pump the furnace down to base pressure and hold it there for half an hour.
- The tube must be flushed with UHP N_2 several times before starting the bakeout step[§]:
  - Use the N_2 purge valve on the input lines to fill the tube up to atmosphere ($\sim$ 650 – 700 Torr on the vacuum gauge). Turn the valve off, otherwise the tube will overpressurize and the vacuum flanges can blow off causing safety hazards. Note that there is no automatic safety release valve on the furnace for overpressure relief.

[§]At this point, the exhaust vent valve on the pump side of the manifold should be closed.

- Turn the on/off valves on the 1/4" pump bypass line to ON (parallel to the lines). Slowly turn the metering valve to fully open position.
- Once the pressure gauge reads below 200 Torr, slowly start turning the bellows valve on the main KF-25 line. The butterfly valve right downstream of the main valve is typically kept always open. The bellows valve must be slowly opened to prevent extreme load on the pump and backdrafting of pump oil into the chamber. A good rule of thumb is to open it slowly enough such that the reading on the pressure gauge does not go up.
- Once the base pressure is achieved, close the main bellows valve and the top on/off valve on the bypass line.
- Repeat the flushing procedure for at least 5 times.

- Once the tube has been flushed 5 times, the valve upstream of the N_2 MFC should be turned on and the N_2 gas flow should be set at 200 – 300 sccm using the controller. Make sure to keep the main bellows valve open at this point, otherwise the tube will slowly overpressurize.

- Program the following temperature profile on the central zone of the furnace with the controller:

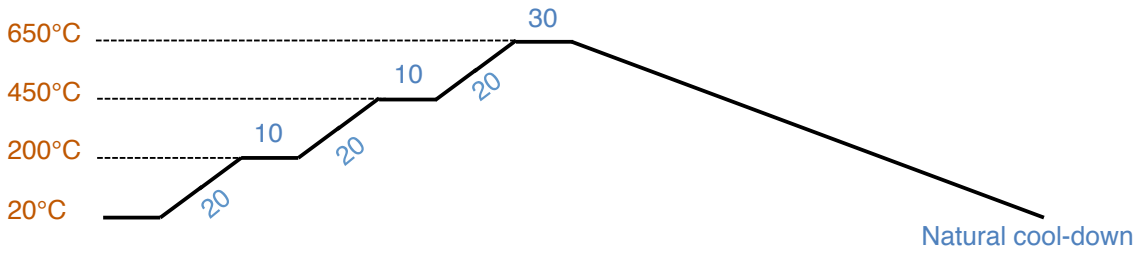

Figure A.1: Temperature ramp profile for bakeout. All time periods are in minutes.

The furnace controller should be turned on by flicking the main switch. Initial reading on all three zones will be room temperature ($\sim$ 20°C). Long-press the SET/ENT on the central zone until the display changes. Then keep single-pressing the button until it reads "PROG". The default value is "0", press the $\uparrow$ button to turn it to "1 and enter the program menu. Read through the controller manual to familiarize yourself with the default values of the different parameters, which will continue to cycle as you keep single-pressing the SET/ENT. Temperature and time setpoint parameters will be accessible in the middle of the menu. Note that even though the furnace naturally cools down to room temperature, a final value with a ramp-down time must be provided. So the

last two entries in the program must read: "(T = 20°C, t = 20 min) and (T = 20°C, t = off)".

- Once the program has been set, long-press SET/ENT to go back to temperature display. When you're ready, long-press the ↓ button to start the ramp-up process. You will hear a loud click, which signals the power breaker turning on.

- Let the furnace naturally cool down to room temperature. Then close the all the open pump valves, set the MFC dial to zero, and turn off its valve. Fill the furnace up to atmosphere using the N_2 purge line valve. If the furnace has overpressurized, quickly turn off all input gas valves and open the exhaust vent valve on the pump manifold side to relieve the pressure. The exhaust lines are maintained just below atmosphere so the tube pressure will be recovered back. NEVER open the exhaust vent valves while the furnace is under vacuum, as there will be an explosive back flow into the furnace through the vent lines and it can decompress violently.

A.2.2 Calibrating temperature profile

It is recommended to perform a temperature calibration on the vdWE furnace every time a major component is replaced or once a year. The thermocouples of the furnace zones are located outside the tube, embedded within the ceramic. The actual temperature inside the tube is generally always higher than the value on the controller. A good statistical value for the offset is ~ 70°C. The following procedure should be used:

- Remove the pipe thread nut on the 1/4" thermocouple input on the gas input manifold vacuum flange, and remove the silicone stopper and replace it with a 1/4" silicone O-ring.

- A 1/4" OD feedthrough quartz tube will hold the thermocouple line, and hence must be closed on one end. Very carefully insert the thermocouple feedthrough tube with its closed end towards the furnace tube, through the thermocouple input. The 1/4" tube should be long enough that its closed end reaches the ceramic neck zone of the furnace all the way at the other end, where the samples will be stored. This neck zone is where the tube adaptor sits, and where the furnace temperature profile will rapidly be falling. Utmost care must be taken in handling a long 1/4" tube as it is fragile, and will sag or crack easily.

- Carefully insert a long K-type thermocouple line (suitable for $T < 1250°$) through the 1/4" feedthrough tube. The end of the thermocouple that is open to air is the point at which the temperature will be measured.

- Once the furnace is closed, there is no way to tell where the thermocouple sensor is located exactly. It is advisable to mark the location of the thermocouple sensor manually. First, move the thermocouple sensor point to the location where temperature needs to be measured, then make a mark on the thermocouple line where it meets the open end of the 1/4" feedthrough tube with a sharpie. Make as many marks as points at which the temperature needs to be measured. A good rule of thumb is to measure the temperature in the central zone (Zone 2), the outer zone on the pump side (Zone 3) and several points in the neck region of the furnace.

- Slide the thermocouple point to the central zone location, and plug it into a monitor. Close the furnace lid. At this stage, all vacuum flanges must be secured and the tube must have been flushed according to the procedure mentioned in Section-A.2.1.

- Set the temperature profile that is desired on the furnace controller. Once the central zone temperature has stabilized, the thermocouple line can be moved to the points of interest by lining up the sharpie marks on its outer jacket to the edge of the open end of the 1/4" feedthrough tube. The thermocouple must be allowed to stay at the point for a minute before its temperature should be noted. Note that if the thermocouple line is moved frequently during the ramp up or ramp down, the temperature readings may not be accurate due to finite settling time of the thermocouple.

- Once the furnace cools down, bring it back up to atmosphere using the technique described in Section-A.2.1. Remove the thermocouple and the 1/4" feedthrough tube, and put the silicone stopper back in to seal the end properly. There is no need to monitor the temperature during live growths once the profile has been measured.

A.3 Standard operating procedure

This section describes the SOP for the vdWE growth system in detail. For the sake of example, the following SOP describes a step-by-step guide for BTS growth on SiO_2, exfoliated hBN and pristine muscovite mica. It is assumed that any new quartz tubes and wares have been prepared and the furnace temperature profile calibrated as described in Sections A.2.1 and A.2.2. A grower must gown up to go through the clean room and use the fume hoods for cleaning. The following procedure will typically take 5 – 6 hours of presence for an experienced grower. The furnace cools down naturally to room temperature after the growth is complete, which takes ~ 8 hours. It is therefore recommended to finish the growth during the day time and let the furnace cool down overnight.

1. **Prepare growth substrates**:

   (a) For the 60 mm OD furnace tube and its associated quartzware, the typical sample sizes should be of linear dimensions of no more than 20×20 mm^2. If any samples are being loaded vertically in the slotted quartz boat, they can be larger (measure the dimensions of the sample boat to see prior to growth).

   (b) For growths on exfoliated hBN (or any other vdW material), the samples should ideally be prepared a day in advance. After exfoliation onto a clean SiO_2/Si substrate (with our without the etched alignment marker grid), the sample should ideally be vacuum annealed to remove tape residue and relax the stresses in the exfoliated flakes.

   (c) Any SiO_2 substrates with alignment marker grids (prepared using the process described in Section-B.1) should be cleaned in hot acetone/IPA baths prior to loading.

   (d) Any muscovite mica disk (Ted Pella catalog series 50) should be freshly cleaved immediately prior to loading when all other tasks are finished. Muscovite mica is a layered compound that cleaves readily out of plane. Use an uncontaminated scalpel to introduce a small cut along the edge of the mica disk, and then pull the two disks apart swiftly with two clean tweezers. At this point, it is advisable to use a tweezer to pull and lift a small tab at an edge location of the mica disk to indicate the top-side of the substrate.[†]

   (e) Any other substrates (such as sapphire or quartz) must be prepared according to their standard procedures prior to loading. At minimum, always perform solvent cleans for substrates that have been exposed to air to prevent contamination in the growth system.

2. **Load source precursors**: Load the source precursor materials (can be done while a solvent clean on substrates is ongoing):

   (a) Remove the clean room hood, wear a standard particulate respirator[‡] and safety glasses before beginning. Wear double set of nitrile gloves.

   (b) Bring the furnace back up to atmosphere if it is under vacuum. Then make sure that all input gas valves are completely shut off. Unload the powder source and the sample quartz boats.

[†]Cleaving mica substrates cleanly is a bit of an art. It is advisable to practice on several dummy mica disks for firs timers.

[‡]Consult MRC safety coordinator or the MBE lab folks for help on ordering respirators.

(c) Load the quartz boat only without its carrier on the balance scale located in the aluminum fume hood opposite the vdWE system. Tare the scale to zero.

(d) Take the bottle of the powders (Bi_2Te_3) or chunks (Bi_2S_3) to the fume hood and keep them next to the scale on a cloth wipe.

(e) Using clean spoons designated for their corresponding powder sources, drop some Bi_2Te_3 powder into the quartz boat. 12 mg of powder is plenty for a standard vdWE growth.[§] Excess powder SHOULD NOT be added back into the container, but disposed of into another waste container while inside the fume hood.

(f) Once the Bi_2Te_3 powder is loaded, tare the scale back to zero if loading the other source material in the same boat. If using a new boat, load it and tare the balance.

(g) Bi_2S_3 chunks are usually too large to load by themselves. Use a secondary container like an open alumina crucible (inside the fume hood) to break up a Bi_2S_3 chunk using a sharp implement, such as a fine-tipped diamond scribe specifically used for that purpose. For ideal stoichiometry of Bi_2Te_2S, the weight ratios of Bi_2Te_3:Bi_2S_3 should be 3:1. Load 4 mg of Bi_2S_3 chunks into the boat. If it is the same boat as Bi_2Te_3 powder, then be sure to have a large separation between the two sources.

(h) Carefully bring the quartz boat(s) with the source powders back to the vdWE furnace and slide it into the central zone with the furnace rod. Be very careful to not drop or release the powder outside the fume hoods.

(i) Close all bottles caps and load them back into their sealed plastic bags. Pick up any waste carefully with cloth wipes and dispose into the designated trash bin. Dispose of your outer pair of nitrile gloves into the contaminated trash as well.

(j) Once the powder boat(s) is safely loaded into the tube, cover the open end of the tube with a vinyl glove and shut the acrylic hood door.

(k) Remove your contaminated vinyl gloves and dispose of them in the contaminated trash can before removing your respirator and putting your hood back on.

3. **Load substrates**: load the substrates onto the quartz sample boat as shown in the schematic Fig-A.2, while the boat is outside the tube. If there is a lot of deposition on the sample boat from previous growths, it is advisable to keep the boat in the acrylic negative pressure hood at all times. In that case, be

[§]You must practice first to see how much 12 mg powder "looks like" in the spoon before doing a live growth.

careful loading the mica samples as they can "fly off" if they're very thin. At this point, you should be wearing vinyl gloves on top of your nitrile gloves.

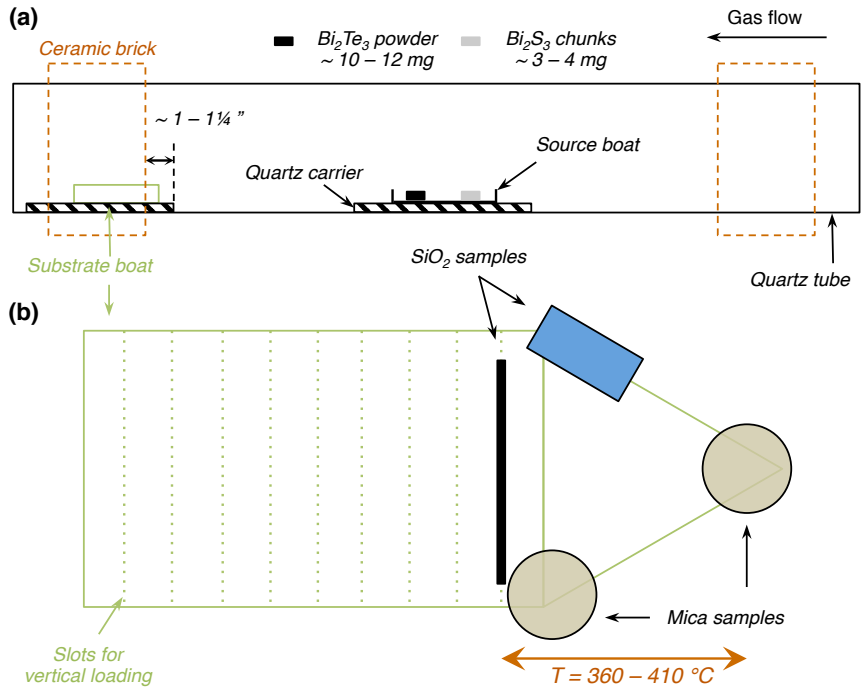

Figure A.2: (a) Cross sectional schematic showing vdWE furnace setup for growth. (b) Enlarged top view of the sample boat.

(a) All SiO_2/Si substrates should have been cleaned in hot acetone/IPA and baked on a > 100°C hotplate for a minute before loading. All exfoliated vdW materials, *e.g.*, hBN on SiO_2/Si substrates should have been already vacuum annealed and stored in a desiccator, or should have been cleaned in hot solvent and baked before loading. All muscovite mica substrates should be freshly cleaved before loading (no more than 10 minutes).

(b) In the current setup of the vdWE furnace with the precalibrated central zone temperature setpoint of 450°C (actual $T \approx 520$°C), substrates that are loaded horizontally on the "bow" of the sample boat will be in a zone of 380 – 410 °C and the substrates loaded vertically in the first slot will be in the range of 360 – 380 °C temperature range, as shown in Fig-A.2(b).

(c) Gently grab the quartz carrier that is supporting the sample boat from the back end and load the boat in the tube's mouth. Use a quartz furnace rod to push the boat to the neck of the furnace.

(d) As shown in Fig-A.2(a), the sample boat should be loaded at the neck such

that the distance between the frontmost end of the quartz carrier and the inner-edge of the ceramic brick at the neck will be $\sim 1 - 1^1/_4$" apart. This will ensure the temperature range mentioned above.[†]

(e) Once the sample boat is loaded at the correct location, fasten the flange on the tube and connect it to the KF-25 pump line. It is advisable to carry out the fastening process gently, as rough handling may disturb the substrates and smaller/lighter substrates like mica can even fall off the boat.

4. **Pump down to base pressure**: Make sure all gas input valves, and the exhaust vent valves are turned off. Use the 1/4" bypass line to start pumping the tube. Once the pressure gauge crosses below 200 Torr, slowly open the main bellows valve such that the pressure in the tube doesn't spike up. If the main valve is opened rapidly, the sudden turbulence inside the tube can move substrates, quartz carriers or even suck the powder out. Leave the tube under base pressure for half an hour. The base pressure should be $\sim 6 - 7$ mTorr with a standard roughing pump.

5. **Flush the tube**: Flush the tube with UHP N_2 for atleast five times as described in the bakeout procedure in Section-A.2.1. Be vigilant during the entire flushing process, as overpressure in the tube can move substrates, quartz carriers or blow the powder out. This process should take 15 minutes. After the cycles, pump down to base pressure again and hold for 10 minutes. The flushing step rapidly dries the tube of any moisture and pushes out most of the atmospheric gases, *e.g.* O_2.

6. **Purge the tube**: Turn off the main bellows valve but keep the bypass line fully open. Turn on the valve on the N_2 MFC line and set the gas flow to 50% (300 sccm) on the controller for a continuous purge. This will ensure a slow drying and cleaning of the tube with a steady flow of pure N_2. The pressure in the tube will rise to below 50 Torr. The tube should be purged for at least 2 hours. Then turn off the MFC and pump back down to base pressure.

7. **Fill the tube up**: Close all pump valves. Turn on the N_2 MFC and set it to 90% (450 sccm). The tube pressure will start to rise. Typical pressure for BTS growths are in the 20 – 50 Torr range. Let the tube pressure cross 100 Torr. Now turn the gas flow down to the setpoint: 100 – 200 sccm (20 – 40%).

8. **Pump down to growth pressure**: The current pump bypass line setup with the 1/4" metering valve will hold $\sim 20 - 25$ Torr tube pressure at ~ 150 sccm N_2

[†]The calibration in the furnace can drift over time and with new components, so it is recommended to double check this sample temperature range before a live growth.

flow when completely open. After opening the bypass line, the tube pressure will slowly start falling down to the desired value. Never reverse these two steps, they should always be in the order of: filling the tube up to a higher pressure first then pumping it down to growth pressure. The pressure should be stabilized for another 2 hours.

9. **Growth steps**:

   (a) Close the furnace lid and fasten the latch.

   (b) Once the tube pressure has been stabilized, the furnace controller on the floor should be turned on. Using the method described in the bakeout process of Section-A.2.1, set the temperature ramp shown in Fig-A.3.

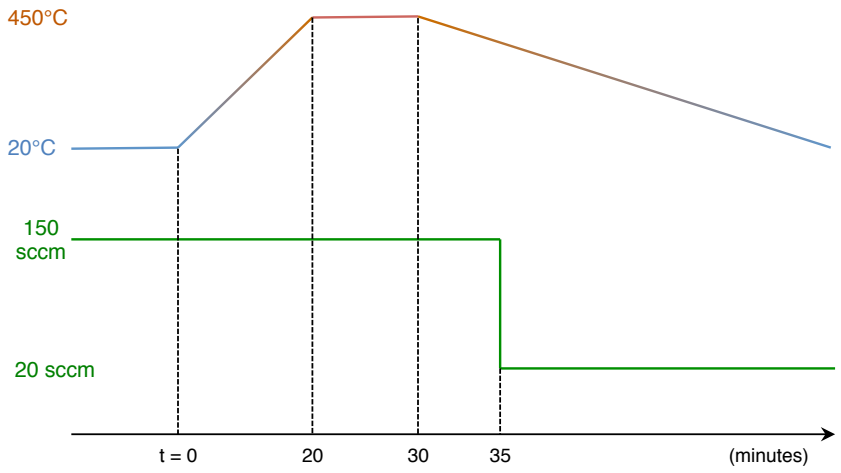

Figure A.3: Temperature and gas flow rate profiles for the BTS vdWE growth. All time stamps are in minutes.

   (c) When you start the program, start a count-up timer to keep track of time. Note down all the details of the growth setup in your journal while you wait for the ramp up such as: materials, substrates (their preparation), N_2 cycle details, pressure/flow numbers, temperature profiles and any other special comments. The journal entries should be detailed enough to provide all the information even if being checked after 2 years.

   (d) The default growth-time is 10 minutes. Note that the source precursor material will start sublimating well before the temperature in the central zone reaches the setpoint and will continue to sublimate well after the time-stamp when the rampdown begins (*i.e.*, when the furnace controller turns

the current off). This is largely due to incongruent non-stoichiometric elemental sublimation of the bismuth and chalcogens. Similarly, the substrate temperature will be in the range of growth for slightly longer than 10 minutes. If a different growth time is desired, make sure to maintain the Δt's in the timestamps for the ramp-up and the reduction of the gas flow rate.

(e) The gas flow rate should be reduced soon after the furnace starts cooling, in order to significantly decrease the adatom flux that is still being sublimated from the precursors. Note that if you open the main valve at this point, you may introduce too rapid a change in the partial vapor pressure locally on top of the substrates, which can affect the growth. Test growths must be carried out in order to determine the effects of such minute details on the growth.

(f) As the furnace starts cooling down after the hold-time is over, the controller should have turned off the current to the zones. However, it is still advisable to manually power off the controller with the main switch when the gas flow is reduced to prevent any accidental ramping up.

10. **Unload furnace**:

(a) After the furnace has cooled down to room temperature overnight, go in through the main clean room and turn off the MFC valve. Open the main bellows valve and pump to base pressure. Then repeat 2 N_2 flushing cycles to remove any trace contamination before exposing the furnace to atmosphere. After the final N_2 cycle, bring the tube pressure to slightly above atmosphere ($\sim$ 800 Torr), and then open the exhaust vent valve.

(b) At this point, bring the sample holder boxes out nearby and keep them open for easily unloading the samples without changing gloves.

(c) Put on a pair of vinyl gloves on top of your nitrile gloves. Put on your respirator mask and safety glasses, and gently unfasten the pump-side flange on the tube. Again be careful not to move the tube much. Use the furnace rod to remove the sample boat, and then gently unload each sample into its holder box with a pair of clean tweezers while inside the acrylic hood. You can close the box lids later with a fresh pair of gloves.

(d) Pull the source boat with the leftover powders and chunks out very carefully with the furnace rod. Be very careful as to not accidentally release the powder outside the acrylic hood. While inside the hood, gently open the waste powder bottle that is stored there, and empty the contents of the source boat in there. Be careful to not violently agitate the waste bottle or tap it too hard while it is open, otherwise powder may be released.

(e) Put both the source and sample boats back into the furnace, fasten the vacuum flange back on and turn off the exhaust vent valve. Take your contaminated gloves off first and dispose of them in the contaminated trash can before taking your respirator off.

(f) Pump the furnace down to base pressure. If you will not be performing another growth in that week, close all the pump valves and gas input source valves. Turn the pump off and let the tube sit under vacuum until the next growth.

(g) Store the samples in a N_2 or vacuum desiccator for preventing material degradation.

A.4 The Dos & Don'ts and special comments

Some special comments regarding the vdWE system:

- If the tube doesn't pump down to base pressure, then there is likely a leak in the manifold. Speak with MRC staff to get help on locating and fixing the leak.
- If the tube pressure pumps down to base pressure, but starts rising once the pump valves are closed then there is likely a "virtual leak". This is a due to a higher pressure (but below atmosphere) gas being trapped somewhere in the manifold between a valve and the tube, which starts leaking into the tube once it reaches base pressure.
  - The usual culprits are the lengths of piping between the MFC on/off valves and MFC inputs. Open the main pump valve then with the MFC on/off valve turned off, set the MFC gas flow to 50%. The trapped gas will slowly be pumped out, and the pressure gauge will go back down after rising up momentarily.
  - A less likely culprit is the defunct exhaust valve on the pump-side vacuum flange on the tube. If so, carefully turn the valve open while pumping on the tube. Once it is fully open, the pressure should rise up and then back down.
  - Finally, it is possible that the N_2 purge line valve is not shut off completely. Make sure it is turned off tightly.
  - If a future modification to the vacuum manifold is scheduled, be sure to include quarter-turn on/off valves upstream of the N_2 purge valve, and downstream of all MFCs to prevent virtual leaks in the future.
- It is very likely that the tube pressure starts rising during growth, typically after the central zone has crossed 400° (actual temperature) and there is a

larger quantity of source precursor. It is only of concern if the pressure is rising very quickly (more than 1 Torr/min). In that case if the bypass metering valve is not fully open, then slowly turn the valve to reduce the pressure. Be sure to not open it too quickly, otherwise the chamber pressure and flux conditions will not be favorable to growth. If the valve is fully open and the pressure is still rising too fast, then there are two possible solutions: reduce the MFC gas flow rate very slowly but steadily until the pressure is stabilized or very gently open the main bellows valve just a tad to stabilize the pressure. The latter technique requires a lot of practice and finesse and is not recommended for beginners.

- The Ar-gas line has been connected to the other MFC, but the MFC is calibrated for H_2 not Ar. A gas correction factor (GCF) value must be used to convert the H_2 calibrated gas flow rate to Ar gas flow for the MFC. The vacuum gauge will also require a calibration to Ar. Speak with MRC staff to get help.

- DO NOT operate the furnace with no gas flow, as the precursor flux can back-flow into the gas input manifold and contaminate it.

- For low-pressure growths where the main bellows valve is opened, a finer pressure control may be achieved by adjusting the butterfly valve directly downstream. This hasn't been tested before, so must be calibrated in a dry test run.

- The tube should be changed out once every six months of regular growth, or any time a new precursor is to be introduced. You can maintain two tubes simultaneously for two different materials by securely storing one in the quartz cabinet. Do not use the same tube for multiple compounds as there will be cross-contamination on the substrates.

For safety, efficiency and equipment longevity purposes, here are a list of dos and don'ts.

Dos:

- Wear complete clean-room gear while operating the vdWE system for safety.

- Always wear a respirator and safety glasses while loading and unloading the furnace.

- Always keep an eye on the vacuum gauge while venting or pumping the tube.

- Always turn the exhaust vent valve off after venting the tube.

- Change the pump oil periodically (every six months of regular usage, or if it has turned dark).

- Always check the thermal aisle to see if anyone else is working there before handling powders and putting on your respirator. Wait until they are done.

Don'ts:

- DO NOT turn off the baffle on the negative pressure acrylic hood unless advised by MRC staff.
- DO NOT get distracted during the N_2 flushing cycles and filling the tube.
- DO NOT handle source powders and contaminated furnace parts without wearing a respirator.
- DO NOT vent the tube directly to exhaust vent. Always bring it up to slightly higher than atmosphere ($\sim$ 800 Torr) with N_2 purge before venting.
- DO NOT pump on a line open to atmosphere. This will harm the pump.
- DO NOT dispose of contaminated wipes and gloves in general clean room trash. Only dispose of in the specialized trash near the vdWE furnace.
- DO NOT hesitate to report any accidents (broken quartz ware, leaked powders *etc.*) to MRC staff. Their foremost concern is your and other users' safety.

Appendix B

Fabrication Processes

This appendix describes the different fabrication processes utilized in this research work.

B.1 SiO_2 substrates with alignment marker grid

For most growths it is advisable to have thermal SiO_2/Si substrates with alignment marker grids ready in advance, as they provide a convenient testbed for quick materials characterization and even device fabrication using e-beam lithography (EBL). Note that for vdWE growths, it is preferable to have the alignment marker grid etched into the SiO_2 film, rather than having the typical metallic markers. Metallic markers act as nucleation centers for undesirably dense growth and can lead to unintentional metal doping and contamination. The fabrication steps for the SiO_2 substrates are as follows:

1. Obtain 3 – 4 low resistivity n^+-Si 4" wafers. High resistivity substrates are required for RF and microwave applications. Clean the wafers with standard piranha, 10 cycle DI water, a quick 1:40 HF dip (to remove native oxide), and another 5 cycle DI water clean in the C16 acid hood, and spin dry them before loading in the gate-oxide furnace.

2. Load wafers in MRL Gate-ox furnace (use the Field-ox furnace only if Gate-ox is unavailable). Run the "gate1050" recipe on the furnace controller to obtain 285 – 300 nm of dry thermal SiO_2 (check logbooks for time calibration). Only use dry oxidation recipes, wet oxides are generally much leakier and not good for device applications. Confirm the thickness using the ellipsometer, after the oxide has been grown.

3. Spin-coat AZ 5209E photoresist (PR) at 4000 rpm on the wafers and prebake them at 90°C on a calibrated hotplate for 90 seconds or in a 90°C process oven for 10 minutes. No need to use PR adhesion primers.

4. Load the wafers into one of the two wafer-scale mask aligners (Karl Süss MA6 or EVG) with the standard brightfield alignment marker grid mask and expose using the i-line UV lamp (365 nm) at 7.5 mW/cm^2 constant intensity for 9 seconds in vacuum contact mode. Develop the wafers in standard 2.3%-TMAH developer (AZ 726 MIF or Dow MF-26A) for $\sim$ 30 seconds (or a precalibrated development time) with mild agitation. Rinse the wafers with DI water and quickly inspect grid patterns under microscope at low illumination (to prevent pattern degradation).

5. Load the wafer in the Plasmatherm-#2 RIE in the right-side chamber with a quartz ring. Use the standard SiO_2 etching recipe (CHF_3 + O_2 at 400 V_{DC}) for an amount of time that is predetermined to etch the oxide from the marker grid pattern regions completely. It is recommended to etch it down to the Si substrate, which helps in obtaining a decent contrast required during EBL alignment. A marker grid that is only partially etched SiO_2 may not provide enough contrast especially at lower SEM apertures ($< 30\mu$m).

6. The PR etch mask will now have polymerized and would be difficult to remove in solvent cleans. Use a standard piranha clean to remove the PR from the wafers.

7. Old wafers with alignment marker grids become hydrophobic or have organic contamination on the surfaces, and should be cleaned with standard piranha cleans before using as growth substrates.

B.2 Device fabrication for vdWE grown TI

This section describes the standard fabrication process for TI devices vdWE grown on SiO_2/Si substrates, exfoliated vdW materials such as hBN on SiO_2/Si susbtrates, or muscovite mica substrates using standard EBL liftoff techniques with minor modifications.

B.2.1 EBL for vdWE grown TI

1. Remember that the alignment marker grid on the SiO_2 is etched in. Utmost care must be taken to design the contact leads and pads layout in the EBL to avoid any overlap with the alignment markers or numbers, otherwise the metallic leads and pads will short to the exposed Si substrate at the alignment markers.

2. Spin-coat PMMA A4 at 3000 rpm for 1 minute (or PMMA A2 if contact metal thicker than 200 nm needs to be deposited). If the TI is grown on exfoliated hBN, the spinner should be ramped up to 3000 rpm instead of directly spun to prevent hBN flakes from flying off.

3. Prebake the PMMA on a precalibrated hotplate at 135°C for 90 seconds. TI compounds containing chalcogenides can unintentionally get substitutionally doped if exposed to higher temperatures due to evaporation of high vapor pressure chalcogens.

4. For TI grown on unpatterned insulating substrates such as mica, another layer of e-spacer ink must be spin-coated at 2500 rpm for 1 minute to prevent charging during EBL. It is assumed that the EBL alignment marker grid has been patterned on the substrate using standard photolithography and metal liftoff. Refer to Section-B.3.2 for photolithography process on mica substrates.

5. Load the samples in the SEM chamber and perform the standard EBL lithography with a dose of 380 μC/cm^2. At lower aperture sizes, the etched-in alignment markers on SiO_2 may not be visible very clearly. Contrast must be adjusted, and alignment must be performed at least 3 times to improve accuracy. Care must be taken to not accidentally expose any PMMA that can connect the leads/pads layout with any exposed alignment marker regions.

6. Develop the PMMA using a standard 1:4 MIBK:IPA solution. If feature sizes or pitches smaller than 500 nm are desired with high shape accuracy, a cold development ($\sim 5^{\circ}$C) in DI water is much more preferable.

7. Immediately prior to metallization using CHA, run an Ar RIE on the sample in Plasmatherm-#2 right chamber to remove surface contaminations, oxides and improve contact adhesion. The power should be 75W, Ar gas flow 20 sccm, chamber pressure 30 mT and duration less than 15 seconds. Program the final step to NOT vent to atmosphere when done to keep sample in vacuum and prevent contact area oxidation.

8. Load the CHA with Ti and Pd (or Au) sources. Vent the RIE, load the samples then pump down CHA as soon as possible. Deposit 5 nm of wetting layer of Ti and $\sim$ 120 – 140 nm of Pd (or Au) for normal contacts. Follow the standard CHA deposition rules. Contact pad thickness must be more than 100 nm to successfully wirebond to or survive repeated probing.

9. Even after taking care, if some part of the metallic patterns has accidentally overlapped with exposed alignment markers, then load an old and used probe tip on the Cascade Microtech probe station and manually break the metallic connection by scratching it off with the tip.

10. For devices that require top gating, it is advisable to dry transfer a thin flake ($\sim$ 10 – 20 nm) of hBN as the dielectric on top of the TI with patterned contacts. For dual gated devices, all contact leads near the active device area must be kept thin ($<$ 20nm) to facilitate easy transfers and clean interfaces. Top-gate lithography should be carried out in EBL in a following step using the same process as described above.

B.2.2 Wirebonding for vdWE grown TI devices

For metal pads on SiO_2/Si substrates, the K&S Au Ball Bonder is utilized for wirebonding to a standard 16-pin dual in-line package (DIP) or the PPMS sample pucks (*e.g.*, horizontal rotator puck).

1. The 16-pin DIP must have been grinded down at the crescent-shaped notch to remove the electroplated gold from the location, otherwise the DIP will short to the PPMS insert's housing. Use the grinder wheel in the machine shop, after getting trained by MRC staff. Remember, ALWAYS go in to the shop with a buddy and NEVER alone for safety.

2. Cleave the SiO_2/Si substrate down to size such that it can fit on the sample holder (3×5 mm^2 for DIP and 5×5 mm^2 for the PPMS pucks). Be careful not to damage the patterned devices.

3. If the Si substrate is highly doped then it must be grounded even when a backgate is not to be applied to prevent any floating potential buildup. The sample backplate on the DIP is electroplated. You must use a diamond scriber to gently scratch off the oxide at the back of the Si substrate BEFORE breaking it into small pieces. Apply a small dab of conductive silver paste to the backside of the substrate and gently attach it on the DIP by very gently pushing down it. Let it dry for 5 minutes before bonding.

4. Double-sided Kapton tape can be used to attach the substrate onto a PPMS puck. However, if a backgate is desired, then first attach a Si sample that has thick gold ($\sim$ 100 nm) evaporated on it to the puck. Then scratch the oxide on the back of the device substrate and use the silver paste method to attach it to the gold sample.

5. Load the DIP onto the lab-jack that is modified to hold it or the PPMS puck onto the puck holder. You must use one of these two platforms for your package, as the default ball bonder platform cannot be used.

6. Take a printout of an optical image of your device layout with any relevant details.

7. Bond the pads on the substrate using the standard two-stitch wirebonding method:

   (a) Bond the ball onto the pad on the substrate. Settings: ball size 5.2, sonication power 2.3, sonication time 4.5, tip force 1.1. Keep the loop size large so that you can comfortably stretch the wire onto the package pads.

(b) Bond the wedge stitch (crescent) onto the package pads. Settings: sonication power 4, sonication time 5, force 4. Remember that you cannot use pads# 1, 8 , 9 and 16 on the 16-pin DIP as they correspond to the pins on the DIP corners, which aren't connected to any port in the PPMS insert. You may have to use a higher sonication power and/or time to bond to the PPMS puck pads if they're dirty. Remember you CANNOT bond to any "THERM" pads if they're present on the PPMS puck, for electrical transport measurements.

(c) If you want to change the settings, make sure to practice on dummy samples with pads first. DO NOT change the ball size too much without consulting MRC staff. Tips have specific bore sizes and too large or too small a ball size can clog the tip for good.

8. Note down the device contact to package pad connections on the printed image of the device for measurement reference.

B.3 CF-vdWE fabrication process

This section describes the fabrication steps required for the CF-vdWE process on mica substrates.

B.3.1 Prepatterning mica

It is imperative to be very careful with mica substrates as they are transparent and to keep track of the front side (freshly cleaved side) of the sample.

1. Cleave a mica disk using a clean scalpel and prepare several substrates. Do not clean them with solvents.

2. Quickly spincoat PMMA A4 at 4000 rpm for 1 minute and prebake the samples on a precalibrated hotplate at 180°C for 2 minutes.

3. After the samples have cooled down, spincoat AZ 5209E photoresist at 4000 rpm for 45 seconds. After spincoating PR on all samples, bake them in a 90°C process oven in a clean aluminum foil basket for 15 minutes. It is found that oven-baked PR is more uniform and has better resolution than hotplate baked PR for mica lithography.

4. Load the mica samples in Karl Süss MA 6 aligner with the growth prepattern mask (either Layer 0 for growth test annuli structures or L1 for growing Hall bar and active device regions), and expose them with the 365 nm i-line UV lamp at 7.5 mW/cm^2 intensity for 8 seconds in vacuum contact mode. Vacuum contact mode significantly improves resolution on the transparent mica substrates.

5. Develop the PR using standard 2.3%-TMAH developers for 35 seconds, rinse carefully with DI water and dry with N_2 gun. Inspect patterns under the microscope and develop further if necessary. This process describes conventional positive lithography, *i.e.*, the mask is brightfield (mostly transparent) and resist is positive (UV exposed regions develop). The features visible in the microscope would be the PMMA/PR bilayer stack, and the mica regions under the bilayer stack will be protected from the fluorination plasma process.

6. Meanwhile, a 45 – 60 minute O_2-only 300 W clean process should have been run on the right chamber of Plasmatherm-#2.

7. Once all samples have been developed, load them into Plasmatherm-#2 for the two-step RIE process:

   (a) 100 W, 18 sccm O_2, 50 mT chamber pressure, 1 minute 30 seconds to transfer PR patterns down onto the PMMA film.

   (b) (Pump with turbo + Purge with N_2)×2

   (c) 100 W, 20 sccm CF_4 + 3 sccm Ar, 50mT chamber pressure, 1 minute 30 seconds to fluorinate the exposed mica surface for selective-area surface free energy modification.

8. Inspect the samples under the microscope to check if the PMMA/PR features is still visible. If it isn't, the O_2 process was too violent and etched all the resist. These samples may not show good selective-area growth.

9. Put the samples into hot NMP (Remover PG Microchem) beaker at 80°C overnight with a covered lid to remove the organic resists.

10. Clean the samples in a fresh bath of Remover PG, then IPA and dry with N_2 gun immediately before loading them into the vdWE furnace for growth.

B.3.2 Device fabrication on CF-vdWE grown TI

After the vdWE growth step (as described in Section-A.3), the prepatterned mica samples should show growth of TI film in the regions that were protected by the bilayer resist in the lithography process, and negligible to no deposition on the fluorinated regions. For mica substrates with CF-vdWE grown TI Hall bars and devices (Layer 1 on the mask), a metal contact layer can be directly aligned on top.

1. Using steps 2 and 3 from the process from Section-B.3.1, spincoat the bilayer resist on the CF-vdWE TI/mica substrate. While lithography process is ongoing, you can start a 45 – 60 minute 300W O_2 clean on the right chamber of Plasmatherm-#2.

2. As the alignment on MA6 or MJB4 aligners is done manually, it is advisable to use the brightfield version of the contact pad patterns (Layer 2) on the mask such that the TI features are visible during alignment. This requires an image reversal lithography process. If the darkfield version of the contact pad layer is being used, then follow the process in steps 4 and 5 from Section-B.3.1. The image reversal litho process steps are as follows:

   (a) Align the brightfield contact pad layer in MA6 manually. Check each device that is going to be measured, and confirm that the contact leads fully line up on the TI regions. Utilize the large alignment markers at the north/south and east/west edges of the die to start alignment. Expose with the same parameters as step 4 in Section-B.3.1 in vacuum contact mode. Align and expose all other substrates.

   (b) After exposure, bake the substrates in the 110°C process oven for 150 seconds to invert the resist. If a hotplate is being used, make sure to calibrate it at 115°C and bake for 1 minute.

   (c) Remove the mask from the aligner and flood expose all substrates *individually* on the aligner, at the same intensity for 40 – 45 seconds to reverse the patterns. Now follow step 5 from Section-B.3.1 for development of the PR. Inspect the patterns under the microscope and double check that the image reversal process worked. If not, you must strip the resist bilayer and start over.

3. Load the developed samples into the right chamber for the two step process:

   (a) 100 W, 18 sccm O_2, 50 mT chamber pressure, 1 minute 30 seconds to transfer PR patterns down onto the PMMA film.

   (b) (Pump with turbo + Purge with N_2)×2

   (c) 75W, 20 sccm Ar, 30 mT chamber pressure, less than 15 seconds. Program the final step to NOT vent to atmosphere when done to keep sample in vacuum and prevent contact area oxidation.

4. Prepare the CHA for metal deposition similar to Section-B.2.1, and load the mica samples in for metallization. Care must be taken to load the mica samples. Remove the sample holder on CHA-2 and first load the mica substrates under the springs. Use narrow strips of Kapton (polyimide) tape on the side of the substrate to secure it further. Springs alone will not hold the thin disks. Mica substrates can also be secured to a glass slide with Kapton tape strips and the glass slide can be loaded with the springs. Avoid double-sided copper tape, as it may cleave the mica unevenly while pulling the substrate off.

Appendix C

Magnetotransport Measurements in PPMS

This appendix describes the PPMS transport measurement setups and processes utilized in this research work. All users must familiarize themselves with the Quantum Design PPMS EverCool II system and should be trained by senior lab members before attempting independent experiments. Only Banerjee group students can be officially trained to use the PPMS unsupervised. Users from other groups must get permission from Prof. Banerjee to measure their samples in PPMS. It is imperative to understand the fundamentals of cryogenic magnetotransport measurements before attempting to even get trained on PPMS. There are many tools and personnel safety implications when working with PPMS, such as explosive depressurization of compressed He gas, rapid loss of liquid–He, quenching of the superconducting magnet and many more. Understand the basics of each component of the entire system such as gas canisters, compressors, vacuum pumps and lines, electrical connections, various instruments that are used, in order to be best prepared for unusual or emergency situations. Contact senior lab members and MRC staff for more details and training on some of these components.

C.1 Electrical connections

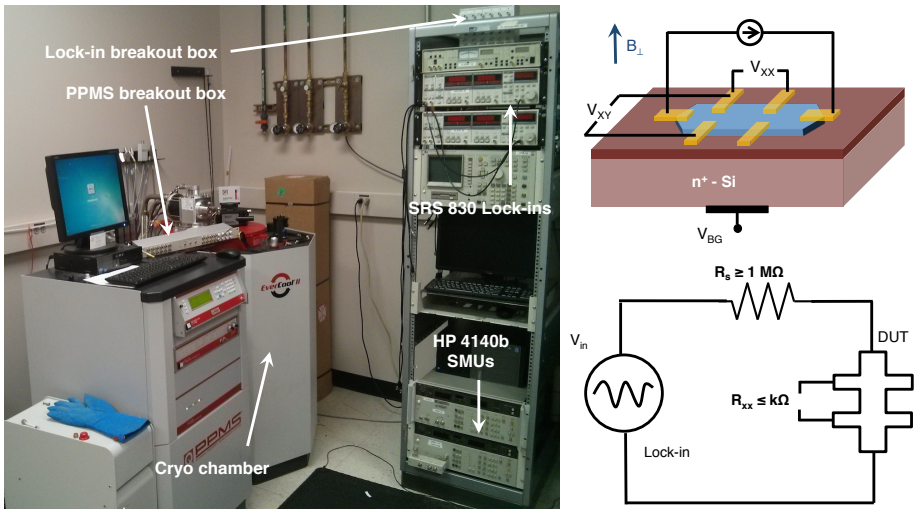

Figure C.1: PPMS transport measurement setup. The schematics on the right show the typical DC magnetotransport measurement topology.

The PPMS measurement setup is shown in Fig-C.1. For all measurements reported in this work, the external SRS 830 lock-in amplifier setup was utilized. Lock-in amplifiers are used to make low-noise high-sensitivity measurements in a heterodyne receiver mode, especially to record small changes or fluctuations on a large signal offset (such as UCF in the MR). The internal PPMS measurement setup was also found to have suboptimal grounding, which can lead to unwanted electrostatic discharge (ESD) and damage to the devices. An in-house breakout box (labeled lock-in breakout box in Fig-C.1) is used externally to provide better grounding. There are 12 channels in the external breakout box, with through BNC connections from front to back panel. Each channel has a switch that can either through-connect the front BNC to the back (switch up) or ground the front BNC to the common ground of the breakout box (switch down). There are also six series resistors that are connected between the front and back panels, to provide input currents to the device under test (DUT) in different ranges. Gate voltage to the device is provided by the HP 4140b SMU, using an HP breakout-box with a triax port that can measure the gate leakage current I_G along with providing the gate voltage V_G.

The SRS 830s are digital lock-in amplifiers with an input isolation of 10MΩ and a large range of sensitivity of 2 nV to 1 V. The master lock-in amp's (top) internal reference channel is used to provide a sinusoidal voltage at a low-frequency (typically $11 - 17$ Hz at 1V amplitude), which is fed through a series resistor on the breakout box to provide a sinusoidal current to the DUT. The DUT is measured in a 4-wire configuration as shown in Fig-C.1 to measure true sheet resistance of the devices. The voltage drop in the DUT is measured at the signal input terminals of the lock-ins in differential mode ($A - B$) with AC input coupling and float shield. This voltage drop can then be converted to a 4-point resistance by dividing by the input DC current value (which in turn is the lock-in output voltage divided by the series resistance). The connections to the DUT are available on the PPMS breakout box (dot-dashed line in Fig-C.2). Connections from the DUT to the lock-in amp are typically made *via* the through ports on the external lock-in amplifier, as shown in Fig-C.2. The outer shields of all BNCs of the breakout box are shorted with the body. The actual ground on the breakout box is enforced by the active ground of the lock-in amplifier *via* the lock-in V_{out} cable. This is done in order to prevent formation of any ground loops by having different active grounds. As long as the internal PPMS SMUs are not used (the bridge 1, 2, 3 switches on the PPMS breakout box are off), the active ground of the lock-in will in turn be enforced on the DUT. When in standby mode, the switches of the ports on the external lock-in breakout box connected to the DUT should be turned off, which will ground all I and V connections of the device and prevent stray ESD.

For measurements made with the Agilent B1500 semiconductor parameter analyzer, triax to coax adaptors must be used for each channel. The B1500 has a standby mode where all ports are by default grounded to the active ground of the

instrument. Make sure to turn this mode on before loading your sample in the PPMS.

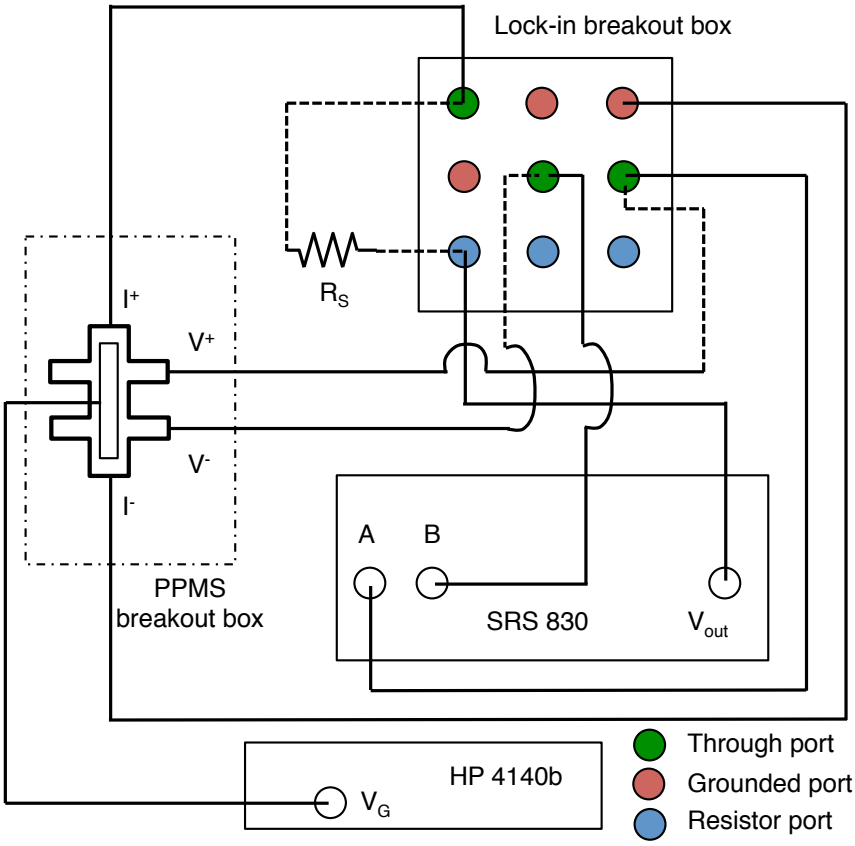

Figure C.2: Connection topology for PPMS measurement using an external SRS 830 lock-in and an external breakout box. Dashed lines represent connections made from the backside of the breakout box to the corresponding ports. All lines represent BNC cables. The ground on the breakout box and hence on the DUT is enforced by the active ground of the SRS 830.

C.2 Loading the DUT in the PPMS

You MUST make sure that the PPMS sample chamber temperature is at 300 K and the applied magnetic field is zero before loading or unloading samples. It is preferable to not make any temperature or field dependent measurements when the PPMS liquid–He level is below 75%. Let the system recover the He gas and compress it back into liquid if the levels fall below that threshold. This rule applies even after the measurement has started. If you have to wait a few hours for the level to recover between two measurements, then go get coffee/dinner. Make all the

necessary connections from the PPMS breakout box to the external lock-in setup as shown in Fig-C.2 BEFORE loading the sample. Turn all the switches on the external lock-in to OFF. This is to prevent accidental ESD from damaging the DUT during the loading process. If using the B1500, make all the connections from the PPMS breakout box to the B1500 prior to loading the insert and turn the standby mode on the B1500 on. The PPMS system has three inserts that are utilized for cryogenic transport measurements: standard PPMS puck, PPMS horizontal rotator and the 16-pin DIP insert. Most of the transport experiments in this work were performed by wirebonding the DUT onto the 16-pin socket or the horizontal rotator.

Care must be taken to not accidentally introduce ESD on the device while loading the sample. It is advisable to wear the ESD wrist-strap while loading the package onto the insert. Do not wear gloves if you are wearing the wrist-strap. Avoid directly touching any parts of the insert with bare fingers, as this can lead to contamination in the sample chamber once the insert is loaded. Load the package onto the insert with the proper tools: tweezers for the 16-pin DIP and the specialized tool for the horizontal rotator. When loading the horizontal rotator, it is a good idea to rotate the sample to 0 degrees on the dial, and then check visually if it is almost perpendicular to the floor (degree dial on the rotator refers to the angle of the sample plane). There might be a few degrees offset, which you should note down in your journal. Once the package is loaded, carefully place the insert back onto the workbench, remove the workbench wrist-wrap and wear the wrist-wrap connected to the PPMS breakout box. Then grab the insert off the workbench and slowly lower it in the chamber. There is a notch at the bottom of all inserts, which will fit within a corresponding notch in the sample chamber below. Rotate the insert until the notch matches and the insert is secure (it will go down a bit further when it sits in the notch). Fasten the appropriate vacuum seal flanges for the insert. Purge and seal the PPMS sample chamber and wait for the pressure to stabilize.

C.3 Measurement notes

Turn on both lock-in amps and both the HP 4140b SMUs. When using the external lock-in setup, you must control the PPMS and the external instrumentation with the LabVIEW VI on the computer in the instrument rack. The computer is connected to the PPMS and the instruments *via* ethernet and GPIB, respectively. Before running any LabVIEW VI, you must confirm that the QD PPMS Instrument Server program on the PPMS computer is active. This program is used to communicate between the instrument computer and PPMS. Make a note of the PPMS computer IP address. This is the IP address that should reflect in any LabVIEW VI that is run from the instrument computer.

Turn on the switches for drain and voltage measurement ports on the external lock-in breakout box. For a good device, you will see a stable voltage drop on the

lock-in with a negligible out-of-phase component. A large value of the out-of-phase component signifies a large reactive component in the device impedance, usually due to bad contacts (either between the contact metal and your active device region or between the DUT metal pads and package pads). Adjust the sensitivity range such that the voltage drop is less than half of the range. Good starting values for the other lock-in settings such as the integration time and filter slopes are provided as user inputs or hardcoded as defaults in the LabVIEW VIs. Do not use too large a temperature or magnetic field ramp up/down rate in the PPMS. For T-sweeps, use a 5 K/min or lower rate and for B-field sweeps use 100 Oe/sec. Faster temperature rates can lead to higher load on the sample heater and increased wear and tear. Similarly, very large B-field rates can result in rapid liquid–He boil off and in worst cases can lead to quenching of the magnet. All LabVIEW programs operate the magnet in the driven mode by default (where the input current circuit is connected to the superconducting magnet). Driven mode always leads to some noise, but for good devices these noise amplitudes translate to negligible variation in the measured resistances. If noise is an issue, the magnet can be operated in the persistent mode instead, where the input current circuit is cut off from the magnet once the supercurrent inside the magnetic coil is established. Persistent mode is very slow, and sweeping the B-field in this mode requires days. It is advisable to use persistent mode only when the externally applied B-field is to be kept at a fixed value, while other parameters are being swept. Persistent mode fields slowly decay with the supercurrent.

Do not change the LabVIEW VIs without express permission of the senior students in the lab. Study the VIs in detail before making any changes and PLEASE make backups of older copies BEFORE changing any code. Remember, an experimental measurement is only as believable as your own understanding of the measurement setup. A 4-wire measurement setup DOES NOT guarantee a measurement totally independent of contact-impedance related effects. If current injecting contacts (drain/source) are very high impedance (large Schottky barriers or bad metal adhesion) or suffer from large Fermi-level pinning, a voltage drop measured *via* different contact probes may not be independent of deleterious effects of the injecting contacts. Not all oscillations observed in the magnetoresistance measurements are Shubnikov–de Haas oscillations nor is all noise universal conductance fluctuations. Rule out the simplest answer (bad contacts, bad connections, ground loops *etc.*) by repeating measurements under different conditions or by varying another degree of freedom (temperature, B-field, E-field *etc.*).

Bibliography

[1] M. Z. Hasan and C. L. Kane, "*Colloquium*: Topological insulators," *Reviews of Modern Physics*, vol. 82, no. 4, pp. 3045–3067, Nov. 2010.

[2] X.-L. Qi and S.-C. Zhang, "Topological insulators and superconductors," *Reviews of Modern Physics*, vol. 83, no. 4, pp. 1057–1110, Oct. 2011.

[3] Y. Ando, "Topological insulator materials," *Journal of the Physical Society of Japan*, vol. 82, no. 10, p. 102001, Sep. 2013.

[4] C. L. Kane and E. J. Mele, "Z_2 topological order and the quantum spin hall effect," *Physical Review Letters*, vol. 95, no. 14, p. 146802, Sep. 2005.

[5] L. Fu and C. L. Kane, "Topological insulators with inversion symmetry," *Physical Review B*, vol. 76, no. 4, p. 045302, Jul. 2007.

[6] L. Fu, C. L. Kane, and E. J. Mele, "Topological insulators in three dimensions," *Physical Review Letters*, vol. 98, no. 10, p. 106803, Mar. 2007.

[7] B. A. Bernevig, T. L. Hughes, and S.-C. Zhang, "Quantum spin hall effect and topological phase transition in HgTe quantum wells," *Science*, vol. 314, no. 5806, pp. 1757–1761, Dec. 2006.

[8] H. Zhang, C.-X. Liu, X.-L. Qi, X. Dai, Z. Fang, and S.-C. Zhang, "Topological insulators in Bi_2Se_3, Bi_2Te_3 and Sb_2Te_3 with a single dirac cone on the surface," *Nature Physics*, vol. 5, no. 6, pp. 438–442, Jun. 2009.

[9] M. König, S. Wiedmann, C. Brüne, A. Roth, H. Buhmann, L. W. Molenkamp, X.-L. Qi, and S.-C. Zhang, "Quantum spin hall insulator state in HgTe quantum wells," *Science*, vol. 318, no. 5851, pp. 766–770, Nov. 2007.

[10] D. Hsieh, D. Qian, L. Wray, Y. Xia, Y. S. Hor, R. J. Cava, and M. Z. Hasan, "A topological Dirac insulator in a quantum spin Hall phase," *Nature*, vol. 452, no. 7190, pp. 970–974, Apr. 2008.

[11] Y. Xia, D. Qian, D. Hsieh, L. Wray, A. Pal, H. Lin, A. Bansil, D. Grauer, Y. S. Hor, R. J. Cava, and M. Z. Hasan, "Observation of a large-gap topological-insulator class with a single Dirac cone on the surface," *Nature Physics*, vol. 5, no. 6, pp. 398–402, Jun. 2009.

[12] J.-i. Wakabayashi and S. Kawaji, "Hall effect in silicon MOS inversion layers under strong magnetic fields," *Journal of the Physical Society of Japan*, vol. 44, no. 6, pp. 1839–1849, Jun. 1978.

[13] K. v. Klitzing, G. Dorda, and M. Pepper, "New method for high-accuracy determination of the fine-structure constant based on quantized Hall resistance," *Physical Review Letters*, vol. 45, no. 6, pp. 494–497, Aug. 1980.

[14] S. Pancharatnam, "Generalized theory of interference, and its applications," *Proceedings of the Indian Academy of Sciences - Section A*, vol. 44, no. 5, pp. 247–262, Nov. 1956.

[15] M. V. Berry, "Quantal phase factors accompanying adiabatic changes," *Proceedings of the Royal Society of London A: Mathematical, Physical and Engineering Sciences*, vol. 392, no. 1802, pp. 45–57, Mar. 1984.

[16] A. R. Akhmerov, J. Nilsson, and C. W. J. Beenakker, "Electrically detected interferometry of Majorana fermions in a topological insulator," *Physical Review Letters*, vol. 102, no. 21, p. 216404, May 2009.

[17] D. Pesin and A. H. MacDonald, "Spintronics and pseudospintronics in graphene and topological insulators," *Nature Materials*, vol. 11, no. 5, pp. 409–416, May 2012.

[18] R. Li, J. Wang, X.-L. Qi, and S.-C. Zhang, "Dynamical axion field in topological magnetic insulators," *Nature Physics*, vol. 6, no. 4, pp. 284–288, Apr. 2010.

[19] Y. Fan, P. Upadhyaya, X. Kou, M. Lang, S. Takei, Z. Wang, J. Tang, L. He, L.-T. Chang, M. Montazeri, G. Yu, W. Jiang, T. Nie, R. N. Schwartz, Y. Tserkovnyak, and K. L. Wang, "Magnetization switching through giant spin-orbit torque in a magnetically doped topological insulator heterostructure," *Nature Materials*, vol. 13, no. 7, pp. 699–704, Jul. 2014.

[20] A. R. Mellnik, J. S. Lee, A. Richardella, J. L. Grab, P. J. Mintun, M. H. Fischer, A. Vaezi, A. Manchon, E.-A. Kim, N. Samarth, and D. C. Ralph, "Spin-transfer torque generated by a topological insulator," *Nature*, vol. 511, no. 7510, pp. 449–451, Jul. 2014.

[21] F. Yang, S. Ghatak, A. A. Taskin, K. Segawa, Y. Ando, M. Shiraishi, Y. Kanai, K. Matsumoto, A. Rosch, and Y. Ando, "Switching of charge-current-induced spin polarization in the topological insulator $BiSbTeSe_2$," *Physical Review B*, vol. 94, no. 7, p. 75304, Aug. 2016.

[22] S. Cho, D. Kim, P. Syers, N. P. Butch, J. Paglione, and M. S. Fuhrer, "Topological insulator quantum dot with tunable barriers," *Nano Letters*, vol. 12, no. 1, pp. 469–472, Jan. 2012.

[23] N. H. Tu, Y. Tanabe, Y. Satake, K. K. Huynh, and K. Tanigaki, "In-plane topological p-n junction in the three-dimensional topological insulator $Bi_{2-x}Sb_xTe_{3-y}Se_y$," *Nature Communications*, vol. 7, p. 13763, Dec. 2016.

[24] P. D. Pietro, M. Ortolani, O. Limaj, A. D. Gaspare, V. Giliberti, F. Giorgianni, M. Brahlek, N. Bansal, N. Koirala, S. Oh, P. Calvani, and S. Lupi, "Observation of Dirac plasmons in a topological insulator," *Nature Nanotechnology*, vol. 8, no. 8, pp. 556–560, Aug. 2013.

[25] S. D. Sarma, M. Freedman, and C. Nayak, "Majorana zero modes and topological quantum computation," *npj Quantum Information*, vol. 1, p. 15001, Dec. 2015.

[26] M. Mogi, M. Kawamura, R. Yoshimi, A. Tsukazaki, Y. Kozuka, N. Shirakawa, K. S. Takahashi, M. Kawasaki, and Y. Tokura, "A magnetic heterostructure of topological insulators as a candidate for an axion insulator," *Nature Materials*, vol. 16, no. 5, pp. 516–521, May 2017.

[27] L. Wu, M. Salehi, N. Koirala, J. Moon, S. Oh, and N. P. Armitage, "Quantized Faraday and Kerr rotation and axion electrodynamics of a 3D topological insulator," *Science*, vol. 354, no. 6316, pp. 1124–1127, Dec. 2016.

[28] J. Chen, H. J. Qin, F. Yang, J. Liu, T. Guan, F. M. Qu, G. H. Zhang, J. R. Shi, X. C. Xie, C. L. Yang, K. H. Wu, Y. Q. Li, and L. Lu, "Gate-voltage control of chemical potential and weak antilocalization in Bi_2Se_3," *Physical Review Letters*, vol. 105, no. 17, p. 176602, Oct. 2010.

[29] H. Steinberg, D. R. Gardner, Y. S. Lee, and P. Jarillo-Herrero, "Surface state transport and ambipolar electric field effect in Bi_2Se_3 nanodevices," *Nano Letters*, vol. 10, no. 12, pp. 5032–5036, Dec. 2010.

[30] L. He, F. Xiu, Y. Wang, A. V. Fedorov, G. Huang, X. Kou, M. Lang, W. P. Beyermann, J. Zou, and K. L. Wang, "Epitaxial growth of Bi_2Se_3 topological insulator thin films on Si (111)," *Journal of Applied Physics*, vol. 109, no. 10, p. 103702, May 2011.

[31] J. Wang, A. M. DaSilva, C.-Z. Chang, K. He, J. K. Jain, N. Samarth, X.-C. Ma, Q.-K. Xue, and M. H. W. Chan, "Evidence for electron-electron interaction in topological insulator thin films," *Physical Review B*, vol. 83, no. 24, p. 245438, Jun. 2011.

[32] M. Liu, C.-Z. Chang, Z. Zhang, Y. Zhang, W. Ruan, K. He, L.-l. Wang, X. Chen, J.-F. Jia, S.-C. Zhang, Q.-K. Xue, X. Ma, and Y. Wang, "Electron interaction-driven insulating ground state in Bi_2Se_3 topological insulators in

the two-dimensional limit," *Physical Review B*, vol. 83, no. 16, p. 165440, Apr. 2011.

[33] J. Chen, X. Y. He, K. H. Wu, Z. Q. Ji, L. Lu, J. R. Shi, J. H. Smet, and Y. Q. Li, "Tunable surface conductivity in Bi_2Se_3 revealed in diffusive electron transport," *Physical Review B*, vol. 83, no. 24, p. 241304, Jun. 2011.

[34] H. Steinberg, J.-B. Laloë, V. Fatemi, J. S. Moodera, and P. Jarillo-Herrero, "Electrically tunable surface-to-bulk coherent coupling in topological insulator thin films," *Physical Review B*, vol. 84, no. 23, p. 233101, Dec. 2011.

[35] N. Bansal, Y. S. Kim, M. Brahlek, E. Edrey, and S. Oh, "Thickness-independent transport channels in topological insulator Bi_2Se_3 thin films," *Physical Review Letters*, vol. 109, no. 11, p. 116804, Sep. 2012.

[36] A. A. Taskin, S. Sasaki, K. Segawa, and Y. Ando, "Manifestation of topological protection in transport properties of epitaxial Bi_2Se_3 thin films," *Physical Review Letters*, vol. 109, no. 6, p. 066803, Aug. 2012.

[37] Y. Takagaki, A. Giussani, K. Perumal, R. Calarco, and K.-J. Friedland, "Robust topological surface states in Sb_2Te_3 layers as seen from the weak antilocalization effect," *Physical Review B*, vol. 86, no. 12, p. 125137, Sep. 2012.

[38] A. Roy, S. Guchhait, S. Sonde, R. Dey, T. Pramanik, A. Rai, H. C. P. Movva, L. Colombo, and S. K. Banerjee, "Two-dimensional weak anti-localization in Bi_2Te_3 thin film grown on Si (111)-(7×7) surface by molecular beam epitaxy," *Applied Physics Letters*, vol. 102, no. 16, p. 163118, Apr. 2013.

[39] D. Culcer, "Transport in three-dimensional topological insulators: Theory and experiment," *Physica E: Low-dimensional Systems and Nanostructures*, vol. 44, no. 5, pp. 860–884, Feb. 2012.

[40] J. Lee, J. Park, J.-H. Lee, J. S. Kim, and H.-J. Lee, "Gate-tuned differentiation of surface-conducting states in $Bi_{1.5}Sb_{0.5}Te_{1.7}Se_{1.3}$ topological-insulator thin crystals," *Physical Review B*, vol. 86, no. 24, p. 245321, Dec. 2012.

[41] D. Kim, P. Syers, N. P. Butch, J. Paglione, and M. S. Fuhrer, "Coherent topological transport on the surface of Bi_2Se_3," *Nature Communications*, vol. 4, p. 2040, Jun. 2013.

[42] F. Yang, A. A. Taskin, S. Sasaki, K. Segawa, Y. Ohno, K. Matsumoto, and Y. Ando, "Top gating of epitaxial $(Bi_{1-x}Sb_x)_2Te_3$ topological insulator thin films," *Applied Physics Letters*, vol. 104, no. 16, p. 161614, Apr. 2014.

[43] Y.-Y. Li, G. Wang, X.-G. Zhu, M.-H. Liu, C. Ye, X. Chen, Y.-Y. Wang, K. He, L.-L. Wang, X.-C. Ma, H.-J. Zhang, X. Dai, Z. Fang, X.-C. Xie, Y. Liu, X.-L. Qi, J.-F. Jia, S.-C. Zhang, and Q.-K. Xue, "Intrinsic topological insulator Bi_2Te_3 thin films on Si and their thickness limit," *Advanced Materials*, vol. 22, no. 36, pp. 4002–4007, Sep. 2010.

[44] Z. Ren, A. A. Taskin, S. Sasaki, K. Segawa, and Y. Ando, "Large bulk resistivity and surface quantum oscillations in the topological insulator Bi_2Te_2Se," *Physical Review B*, vol. 82, no. 24, p. 241306, Dec. 2010.

[45] Y. Takagaki, B. Jenichen, U. Jahn, M. Ramsteiner, K. Friedland, and J. Lähnemann, "Hot wall epitaxy of topological insulator films," *Semiconductor Science and Technology*, vol. 26, no. 12, p. 125009, 2011.

[46] P. Gehring, B. F. Gao, M. Burghard, and K. Kern, "Growth of high-mobility Bi_2Te_2Se nanoplatelets on hBN sheets by van der Waals epitaxy," *Nano Letters*, vol. 12, no. 10, pp. 5137–5142, Oct. 2012.

[47] H. Peng, W. Dang, J. Cao, Y. Chen, D. Wu, W. Zheng, H. Li, Z.-X. Shen, and Z. Liu, "Topological insulator nanostructures for near-infrared transparent flexible electrodes," *Nature Chemistry*, vol. 4, no. 4, pp. 281–286, 2012.

[48] N. H. Tu, Y. Tanabe, K. K. Huynh, Y. Sato, H. Oguro, S. Heguri, K. Tsuda, M. Terauchi, K. Watanabe, and K. Tanigaki, "Van der Waals epitaxial growth of topological insulator $Bi_{2-x}Sb_xTe_{3-y}Se_y$ ultrathin nanoplate on electrically insulating fluorophlogopite mica," *Applied Physics Letters*, vol. 105, no. 6, p. 63104, Aug. 2014.

[49] T. Trivedi, S. Sonde, H. C. P. Movva, and S. K. Banerjee, "Weak antilocalization and universal conductance fluctuations in bismuth telluro-sulfide topological insulators," *Journal of Applied Physics*, vol. 119, no. 5, p. 055706, Feb. 2016.

[50] T. P. Ginley, Y. Wang, and S. Law, "Topological insulator film growth by molecular beam epitaxy: A review," *Crystals*, vol. 6, no. 11, p. 154, Nov. 2016.

[51] Y. Guo, Z. Liu, and H. Peng, "A roadmap for controlled production of topological insulator nanostructures and thin films," *Small*, vol. 11, no. 27, pp. 3290–3305, Jul. 2015.

[52] M. I. B. Utama, Q. Zhang, J. Zhang, Y. Yuan, F. J. Belarre, J. Arbiol, and Q. Xiong, "Recent developments and future directions in the growth of nanostructures by van der Waals epitaxy," *Nanoscale*, vol. 5, no. 9, pp. 3570–3588, Apr. 2013.

[53] K. Momma and F. Izumi, "VESTA 3 for three-dimensional visualization of crystal, volumetric and morphology data," *Journal of Applied Crystallography*, vol. 44, no. 6, pp. 1272–1276, Dec. 2011.

[54] L.-L. Wang and D. D. Johnson, "Ternary tetradymite compounds as topological insulators," *Physical Review B*, vol. 83, no. 24, p. 241309, Jun. 2011.

[55] H. H. Soonpaa, "Anisotropy of the electrical conductivity and the seebeck coefficient of $Bi_8Te_7S_5$," *Journal of Applied Physics*, vol. 33, no. 8, pp. 2542–2546, Aug. 1962.

[56] A. C. Glatz, "The Bi_2Te_3-Bi_2S_3 system and the synthesis of the mineral tetradymite," *The American Mineralogist*, vol. 52, pp. 161–170, Jan. 1967.

[57] L. Pauling, "The formula, structure, and chemical bonding of tetradymite, $Bi_{14}Te_{13}S_8$, and the phase $Bi_{14}Te_{15}S_6$," *The American Mineralogist*, vol. 60, no. 11-12, pp. 994–997, Dec. 1975.

[58] H. Ji, J. M. Allred, M. K. Fuccillo, M. E. Charles, M. Neupane, L. A. Wray, M. Z. Hasan, and R. J. Cava, "$Bi_2Te_{1.6}S_{1.4}$: A topological insulator in the tetradymite family," *Physical Review B*, vol. 85, no. 20, p. 201103, May 2012.

[59] K. Ueno, "About VDWE: What is "van der Waals epitaxy"?" http://van-der-waals-epitaxy.info/?page_id=11, 2012, [Online; accessed 04-August-2017].

[60] A. D. Novaco and J. P. McTague, "Orientational epitaxy - the orientational ordering of incommensurate structures," *Physical Review Letters*, vol. 38, no. 22, pp. 1286–1289, May 1977.

[61] A. Koma, K. Sunouchi, and T. Miyajima, "Fabrication and characterization of heterostructures with subnanometer thickness," *Microelectronic Engineering*, vol. 2, no. 1–3, pp. 129–136, Oct. 1984.

[62] A. Koma, "van der Waals epitaxy for highly lattice-mismatched systems," *Journal of Crystal Growth*, vol. 201-202, no. 0, pp. 236 – 241, 1999.

[63] M. Ferhat, B. Liautard, G. Brun, J. Tedenac, M. Nouaoura, and L. Lassabatere, "Comparative studies between the growth characteristics of Bi_2Te_3 thin films deposited on SiO_2, Si (100) and Si (111)," *Journal of Crystal Growth*, vol. 167, no. 1, pp. 122–128, 1996.

[64] D. Kong, Y. Chen, J. J. Cha, Q. Zhang, J. G. Analytis, K. Lai, Z. Liu, S. S. Hong, K. J. Koski, S.-K. Mo, Z. Hussain, I. R. Fisher, Z.-X. Shen, and Y. Cui, "Ambipolar field effect in the ternary topological insulator $(Bi_xSb_{1-x})_2Te_3$ by composition tuning," *Nature Nanotechnology*, vol. 6, no. 11, pp. 705–709, 2011.

[65] G. Hao, X. Qi, Y. Liu, Z. Huang, H. Li, K. Huang, J. Li, L. Yang, and J. Zhong, "Ambipolar charge injection and transport of few-layer topological insulator Bi_2Te_3 and Bi_2Se_3 nanoplates," *Journal of Applied Physics*, vol. 111, no. 11, p. 114312, Jun. 2012.

[66] W. Dang, H. Peng, H. Li, P. Wang, and Z. Liu, "Epitaxial heterostructures of ultrathin topological insulator nanoplate and graphene," *Nano Letters*, vol. 10, no. 8, pp. 2870–2876, 2010.

[67] T. Trivedi, S. Sonde, and S. K. Banerjee, "Van der Waals epitaxy of bismuth telluro-sulfide nanosheets and magnetotransport in devices," in *Bulletin of the American Physical Society*, vol. Volume 60, Number 1. San Antonio, TX: American Physical Society, Mar. 2015.

[68] T. Michely, M. Hohage, M. Bott, and G. Comsa, "Inversion of growth speed anisotropy in two dimensions," *Physical Review Letters*, vol. 70, no. 25, pp. 3943–3946, Jun. 1993.

[69] A. Roy, S. Guchhait, R. Dey, T. Pramanik, C.-C. Hsieh, A. Rai, and S. K. Banerjee, "Perpendicular magnetic anisotropy and spin glass-like behavior in molecular beam epitaxy grown chromium telluride thin films," *ACS Nano*, vol. 9, no. 4, pp. 3772–3779, Apr. 2015.

[70] S. Liu, Z. Zhang, G. Comsa, and H. Metiu, "Kinetic mechanism for island shape variations caused by changes in the growth temperature," *Physical Review Letters*, vol. 71, no. 18, pp. 2967–2970, Nov. 1993.

[71] R. T. Downs and M. Hall-Wallace, "The american mineralogist crystal structure database," *The American Mineralogist*, vol. 88, no. 1, pp. 247–250, Jan. 2003.

[72] V. Chis, I. Y. Sklyadneva, K. A. Kokh, V. A. Volodin, O. E. Tereshchenko, and E. V. Chulkov, "Vibrations in binary and ternary topological insulators: First-principles calculations and raman spectroscopy measurements," *Physical Review B*, vol. 86, no. 17, p. 174304, Nov. 2012.

[73] A. Purkayastha, Q. Yan, M. S. Raghuveer, D. D. Gandhi, H. Li, Z. W. Liu, R. V. Ramanujan, T. Borca-Tasciuc, and G. Ramanath, "Surfactant-directed synthesis of branched bismuth telluride/sulfide core/shell nanorods," *Advanced Materials*, vol. 20, no. 14, pp. 2679–2683, Jul. 2008.

[74] S. Aminorroaya-Yamini, C. Zhang, X. Wang, and I. Nevirkovets, "Crystal structure, electronic structure and thermoelectric properties of n-type $BiSbSTe_2$," *Journal of Physics D: Applied Physics*, vol. 45, no. 12, p. 125301, 2012.

[75] L.-L. Wang, M. Huang, S. Thimmaiah, A. Alam, S. L. Bud'ko, A. Kaminski, T. A. Lograsso, P. Canfield, and D. D. Johnson, "Native defects in tetradymite $Bi_2(Te_xSe_{3-x})$ topological insulators," *Physical Review B*, vol. 87, no. 12, p. 125303, Mar. 2013.

[76] P. A. Lee and T. V. Ramakrishnan, "Disordered electronic systems," *Reviews of Modern Physics*, vol. 57, no. 2, pp. 287–337, Apr. 1985.

[77] B. L. Altshuler and A. G. Aronov, *Electron-Electron Interactions in Disordered Systems*, ser. Modern Problems in Condensed Matter Sciences, A. L. Efros and M. Pollak, Eds. Amsterdam: Elsevier, 1985, vol. 10.

[78] H.-Z. Lu and S.-Q. Shen, "Finite-temperature conductivity and magnetoconductivity of topological insulators," *Physical Review Letters*, vol. 112, no. 14, p. 146601, Apr. 2014.

[79] D. E. Beutler and N. Giordano, "Localization and electron-electron interaction effects in thin Bi wires and films," *Physical Review B*, vol. 38, no. 1, pp. 8–19, Jul. 1988.

[80] J. J. Lin, S. Y. Hsu, J. C. Lue, and P. J. Sheng, "Spin-orbit scattering effect on electron-electron interactions in disordered metals," *Journal of Physics and Chemistry of Solids*, vol. 62, no. 9âĂŞ10, pp. 1813–1818, Sep. 2001.

[81] Y. Takagaki, B. Jenichen, U. Jahn, M. Ramsteiner, and K.-J. Friedland, "Weak antilocalization and electron-electron interaction effects in Cu-doped Bi_2Se_3 films," *Physical Review B*, vol. 85, no. 11, p. 115314, Mar. 2012.

[82] D. S. McLachlan, "Weak-localization, spin-orbit, and electron-electron interaction effects in two- and three-dimensional bismuth films," *Physical Review B*, vol. 28, no. 12, pp. 6821–6832, Dec. 1983.

[83] P. H. Woerlee, G. C. Verkade, and A. G. M. Jansen, "An experimental investigation on weak localisation, spin-orbit and interaction effects in thin bismuth films," *Journal of Physics C: Solid State Physics*, vol. 16, no. 15, p. 3011, 1983.

[84] S. Hikami, A. I. Larkin, and Y. Nagaoka, "Spin-orbit interaction and magnetoresistance in the two dimensional random system," *Progress of Theoretical Physics*, vol. 63, no. 2, pp. 707–710, Feb. 1980.

[85] B. Xia, P. Ren, A. Sulaev, P. Liu, S.-Q. Shen, and L. Wang, "Indications of surface-dominated transport in single crystalline nanoflake devices of topological insulator $Bi_{1.5}Sb_{0.5}Te_{1.8}Se_{1.2}$," *Phys. Rev. B*, vol. 87, p. 085442, Feb 2013.

[86] Z. Li, T. Chen, H. Pan, F. Song, B. Wang, J. Han, Y. Qin, X. Wang, R. Zhang, J. Wan, D. Xing, and G. Wang, "Two-dimensional universal conductance fluctuations and the electron-phonon interaction of surface states in Bi_2Te_2Se microflakes," *Scientific Reports*, vol. 2, p. 595, Aug. 2012.

[87] M. Bianchi, D. Guan, S. Bao, J. Mi, B. B. Iversen, P. D. C. King, and P. Hofmann, "Coexistence of the topological state and a two-dimensional electron gas on the surface of Bi_2Se_3," *Nature Communications*, vol. 1, p. 128, Nov. 2010.

[88] S. X. Zhang, R. D. McDonald, A. Shekhter, Z. X. Bi, Y. Li, Q. X. Jia, and S. T. Picraux, "Magneto-resistance up to 60 Tesla in topological insulator Bi_2Te_3 thin films," *Applied Physics Letters*, vol. 101, no. 20, p. 202403, Nov. 2012.

[89] R. Dey, T. Pramanik, A. Roy, A. Rai, S. Guchhait, S. Sonde, H. C. P. Movva, L. Colombo, L. F. Register, and S. K. Banerjee, "Strong spin-orbit coupling and Zeeman spin splitting in angle dependent magnetoresistance of Bi_2Te_3," *Applied Physics Letters*, vol. 104, no. 22, p. 223111, Jun. 2014.

[90] B. A. Assaf, T. Cardinal, P. Wei, F. Katmis, J. S. Moodera, and D. Heiman, "Linear magnetoresistance in topological insulator thin films: Quantum phase coherence effects at high temperatures," *Applied Physics Letters*, vol. 102, no. 1, p. 012102, Jan. 2013.

[91] C. Shekhar, C. E. ViolBarbosa, B. Yan, S. Ouardi, W. Schnelle, G. H. Fecher, and C. Felser, "Evidence of surface transport and weak antilocalization in a single crystal of the Bi_2Te_2Se topological insulator," *Phys. Rev. B*, vol. 90, p. 165140, Oct 2014.

[92] B. L. Altshuler, A. G. Aronov, and D. E. Khmelnitsky, "Effects of electron-electron collisions with small energy transfers on quantum localisation," *Journal of Physics C: Solid State Physics*, vol. 15, no. 36, p. 7367, Dec. 1982.

[93] D. K. Schroder, *Semiconductor Material and Device Characterization*, 3rd ed. Wiley-IEEE Press, 2006.

[94] B. Al'tshuler and D. Khmel'nitskii, "Fluctuation properties of small conductors," *JETP Letters*, vol. 42, no. 7, pp. 291–293, Oct. 1985.

[95] P. A. Lee, A. D. Stone, and H. Fukuyama, "Universal conductance fluctuations in metals: Effects of finite temperature, interactions, and magnetic field," *Physical Review B*, vol. 35, no. 3, pp. 1039–1070, Jan. 1987.

[96] P. Gehring, H. M. Benia, Y. Weng, R. Dinnebier, C. R. Ast, M. Burghard, and K. Kern, "A natural topological insulator," *Nano Letters*, vol. 13, no. 3, pp. 1179–1184, Mar. 2013.

[97] A. N. Pal, V. Kochat, and A. Ghosh, "Direct observation of valley hybridization and universal symmetry of graphene with mesoscopic conductance fluctuations," *Physical Review Letters*, vol. 109, no. 19, p. 196601, Nov. 2012.

[98] E. Rossi, J. H. Bardarson, M. S. Fuhrer, and S. Das Sarma, "Universal conductance fluctuations in dirac materials in the presence of long-range disorder," *Physical Review Letters*, vol. 109, no. 9, p. 096801, Aug. 2012.

[99] B. Al'tshuler, "Fluctuations in the extrinsic conductivity of disordered conductors," *JETP Letters*, vol. 41, p. 648, Jun. 1985.

[100] Z. Li, Y. Meng, J. Pan, T. Chen, X. Hong, S. Li, X. Wang, F. Song, and B. Wang, "Indications of topological transport by universal conductance fluctuations in Bi_2Te_2Se microflakes," *Applied Physics Express*, vol. 7, no. 6, p. 065202, Jun. 2014.

[101] P. Gehring, K. Vaklinova, A. Hoyer, H. M. Benia, V. Skakalova, G. Argentero, F. Eder, J. C. Meyer, M. Burghard, and K. Kern, "Dimensional crossover in the quantum transport behaviour of the natural topological insulator aleksite," *Scientific Reports*, vol. 5, p. 11691, Jun. 2015.

[102] H. C. P. Movva, A. Rai, S. Kang, K. Kim, B. Fallahazad, T. Taniguchi, K. Watanabe, E. Tutuc, and S. K. Banerjee, "High-mobility holes in dual-gated WSe_2 field-effect transistors," *ACS Nano*, vol. 9, no. 10, pp. 10 402–10 410, Oct. 2015.

[103] S. Das and J. Appenzeller, "Where does the current flow in two-dimensional layered systems?" *Nano Letters*, vol. 13, no. 7, pp. 3396–3402, Jul. 2013.

[104] F. Ortmann, S. Roche, S. O. Valenzuela, and L. W. Molenkamp, Eds., *Topological Insulators: Fundamentals and Perspectives*. Weinheim, Germany: Wiley-VCH, Verlag GmbH & Co. KGaA, 2015.

[105] Y. Xu, I. Miotkowski, C. Liu, J. Tian, H. Nam, N. Alidoust, J. Hu, C.-K. Shih, M. Z. Hasan, and Y. P. Chen, "Observation of topological surface state quantum Hall effect in an intrinsic three-dimensional topological insulator," *Nature Physics*, vol. 10, no. 12, pp. 956–963, Dec. 2014.

[106] E. S. Walker, S. R. Na, D. Jung, S. D. March, J.-S. Kim, T. Trivedi, W. Li, L. Tao, M. L. Lee, K. M. Liechti, D. Akinwande, and S. R. Bank, "Large-area dry transfer of single-crystalline epitaxial bismuth thin films," *Nano Letters*, vol. 16, no. 11, pp. 6931–6938, Nov. 2016.

[107] C. Ghosh and R. L. Layman, "Selective area growth of gallium arsenide by metalorganic vapor phase epitaxy," *Applied Physics Letters*, vol. 45, no. 11, pp. 1229–1231, Dec. 1984.

[108] M. Nagahara, S. Miyoshi, H. Yaguchi, K. Onabe, Y. Shiraki, and R. Ito, "Selective growth of cubic GaN in small areas on patterned GaAs(100) substrates by metalorganic vapor phase epitaxy," *Japanese Journal of Applied Physics*, vol. 33, no. 1S, p. 694, Jan. 1994.

[109] W. T. Tsang and M. Ilegems, "Selective area growth of GaAs/$Al_xGa_{1-x}As$ multilayer structures with molecular beam epitaxy using Si shadow masks," *Applied Physics Letters*, vol. 31, no. 4, pp. 301–304, Aug. 1977.

[110] J. Noborisaka, J. Motohisa, and T. Fukui, "Catalyst-free growth of GaAs nanowires by selective-area metalorganic vapor-phase epitaxy," *Applied Physics Letters*, vol. 86, no. 21, p. 213102, May 2005.

[111] A. Tanaka, R. Chen, K. L. Jungjohann, and S. A. Dayeh, "Strong geometrical effects in submillimeter selective area growth and light extraction of GaN light emitting diodes on sapphire," *Scientific Reports*, vol. 5, p. 17314, Nov. 2015.

[112] Y. Guo, M. Aisijiang, K. Zhang, W. Jiang, Y. Chen, W. Zheng, Z. Song, J. Cao, Z. Liu, and H. Peng, "Selective-area van der Waals epitaxy of topological insulator grid nanostructures for broadband transparent flexible electrodes," *Advanced Materials*, vol. 25, no. 41, pp. 5959–5964, Nov. 2013.

[113] J. Kampmeier, C. Weyrich, M. Lanius, M. Schall, E. Neumann, G. Mussler, T. Schäpers, and D. Grützmacher, "Selective area growth of Bi_2Te_3 and Sb_2Te_3 topological insulator thin films," *Journal of Crystal Growth*, vol. 443, pp. 38–42, Jun. 2016.

[114] H. Li, J. Cao, W. Zheng, Y. Chen, D. Wu, W. Dang, K. Wang, H. Peng, and Z. Liu, "Controlled synthesis of topological insulator nanoplate arrays on mica," *Journal of the American Chemical Society*, vol. 134, no. 14, pp. 6132–6135, Apr. 2012.

[115] M. Wang, J. Wu, L. Lin, Y. Liu, B. Deng, Y. Guo, Y. Lin, T. Xie, W. Dang, Y. Zhou, and H. Peng, "Chemically engineered substrates for patternable growth of two-dimensional chalcogenide crystals," *ACS Nano*, vol. 10, no. 11, pp. 10 317–10 323, Nov. 2016.

[116] W. Zheng, T. Xie, Y. Zhou, Y. L. Chen, W. Jiang, S. Zhao, J. Wu, Y. Jing, Y. Wu, G. Chen, Y. Guo, J. Yin, S. Huang, H. Q. Xu, Z. Liu, and H. Peng, "Patterning two-dimensional chalcogenide crystals of Bi_2Se_3 and In_2Se_3 and efficient photodetectors," *Nature Communications*, vol. 6, p. 6972, Apr. 2015.

[117] T. Trivedi, A. Roy, H. C. P. Movva, E. S. Walker, S. R. Bank, D. P. Neikirk, and S. K. Banerjee, "Versatile large-area custom-feature van der Waals epitaxy of topological insulators," *ACS Nano*, vol. 11, no. 7, pp. 7457–7467, Jul. 2017.

[118] J. L. Parker, D. L. Cho, and P. M. Claesson, "Plasma modification of mica: Forces between fluorocarbon surfaces in water and a nonpolar liquid," *The Journal of Physical Chemistry*, vol. 93, no. 16, pp. 6121–6125, Aug. 1989.

[119] D. Nečas and P. Klapetek, "Gwyddion: An open-source software for SPM data analysis," *Open Physics*, vol. 10, no. 1, pp. 181–188, 2011.

[120] N. H. Tu, Y. Tanabe, Y. Satake, K. K. Huynh, P. H. Le, S. Y. Matsushita, and K. Tanigaki, "Large-area and transferred high-quality three-dimensional topological insulator $Bi_{2-x}Sb_xTe_{3-y}Se_y$ ultrathin film by catalyst-free physical vapor deposition," *Nano Letters*, vol. 17, no. 4, pp. 2354–2360, Mar. 2017.

[121] Wikipedia, "Contact angle," Jun 2017. [Online]. Available: https://en.wikipedia.org/w/index.php?title=Contact_angle&oldid=783553447

[122] A. Roy, T. Bagarti, K. Bhattacharjee, K. Kundu, and B. N. Dev, "Patterns in Ge cluster growth on clean and oxidized Si(111)-(7 × 7) surfaces," *Surface Science*, vol. 606, no. 9–10, pp. 777–783, May 2012.

[123] T. E. F. M. Standaert, C. Hedlund, E. A. Joseph, G. S. Oehrlein, and T. J. Dalton, "Role of fluorocarbon film formation in the etching of silicon, silicon dioxide, silicon nitride, and amorphous hydrogenated silicon carbide," *Journal of Vacuum Science Technology A: Vacuum, Surfaces, and Films*, vol. 22, no. 1, pp. 53–60, Nov. 2003.

[124] D. Y. Kwok and A. W. Neumann, "Contact angle measurement and contact angle interpretation," *Advances in Colloid and Interface Science*, vol. 81, no. 3, pp. 167–249, Sep. 1999.

[125] G. S. Oehrlein and H. L. Williams, "Silicon etching mechanisms in a CF_4/H_2 glow discharge," *Journal of Applied Physics*, vol. 62, no. 2, pp. 662–672, Jul. 1987.

[126] Y. Zhou, Y. Nie, Y. Liu, K. Yan, J. Hong, C. Jin, Y. Zhou, J. Yin, Z. Liu, and H. Peng, "Epitaxy and photoresponse of two-dimensional GaSe crystals on flexible transparent mica sheets," *ACS Nano*, vol. 8, no. 2, pp. 1485–1490, Feb. 2014.

[127] I. Bhat and S. K. Ghandhi, "The growth and characterization of HgTe epitaxial layers made by organometallic epitaxy," *Journal of The Electrochemical Society*, vol. 131, no. 8, pp. 1923–1926, Aug. 1984.

[128] J. Krumrain, G. Mussler, S. Borisova, T. Stoica, L. Plucinski, C. M. Schneider, and D. Grützmacher, "MBE growth optimization of topological insulator Bi_2Te_3 films," *Journal of Crystal Growth*, vol. 324, no. 1, pp. 115–118, Jun. 2011.

[129] H. Terajima and S. Fujiwara, "Temperature dependence of the surface diffusion distance of bismuth atoms adsorbed on mica, carbon and silicon monoxide surfaces," *Thin Solid Films*, vol. 30, no. 1, pp. 55–64, Nov. 1975.

[130] E. J. Weidmann and J. C. Anderson, "Structure and growth of oriented tellurium thin films," *Thin Solid Films*, vol. 7, no. 3-4, pp. 265–276, Mar. 1971.

[131] R. O. Carlson, R. N. Hall, and E. M. Pell, "Sulfur in silicon," *Journal of Physics and Chemistry of Solids*, vol. 8, pp. 81–83, Jan. 1959.

[132] H. H. Woodbury and R. B. Hall, "Diffusion of the chalcogens in the II-VI compounds," *Physical Review*, vol. 157, no. 3, pp. 641–655, May 1967.

[133] P. M. Borsenberger and D. A. Stevenson, "Self-diffusion of cadmium and tellurium in cadmium telluride," *Journal of Physics and Chemistry of Solids*, vol. 29, no. 8, pp. 1277–1286, Aug. 1968.

[134] M. Hage-ali, I. V. Mitchell, J. J. Grob, and P. Siffert, "Heavy element diffusion in cadmium telluride," *Thin Solid Films*, vol. 19, no. 2, pp. 409–418, Dec. 1973.

[135] H. Stümpel, M. Vorderwülbecke, and J. Mimkes, "Diffusion of selenium and tellurium in silicon," *Applied Physics A*, vol. 46, no. 3, pp. 159–163, Jul. 1988.

[136] M. P. Gomez, D. A. Stevenson, and R. A. Huggins, "Self-diffusion of Pb and Te in lead telluride," *Journal of Physics and Chemistry of Solids*, vol. 32, no. 2, pp. 335–344, Jan. 1971.

[137] Y. Ishikawa, K. Yazaki, and I. Nakamichi, "The diffusion of bismuth in silicon," *Japanese Journal of Applied Physics*, vol. 28, no. 7R, p. 1272, Jul. 1989.

[138] L. E. Rumaner, J. L. Gray, and F. S. Ohuchi, "Nucleation and growth of GaSe on GaAs by van der Waal epitaxy," *Journal of Crystal Growth*, vol. 177, no. 1, pp. 17–27, May 1997.

[139] A. A. Taskin, Z. Ren, S. Sasaki, K. Segawa, and Y. Ando, "Observation of Dirac holes and electrons in a topological insulator," *Physical Review Letters*, vol. 107, no. 1, p. 16801, Jun. 2011.

[140] J. W. McIver, D. Hsieh, H. Steinberg, P. Jarillo-Herrero, and N. Gedik, "Control over topological insulator photocurrents with light polarization," *Nature Nanotechnology*, vol. 7, no. 2, pp. 96–100, Feb. 2012.